SLAC-R-778

Study of Rare Radiative B Decay to K^*_2(1430) Meson Using the BABAR Detector

by Qinghua Guo

Ph.D. Thesis

Stanford Linear Accelerator Center, Stanford University, Stanford, CA 94309

Work supported by Department of Energy contract DE–AC02–76SF00515.

Study of Rare Radiative B Decay to $K_2^*(1430)$ Meson Using the *BABAR* Detector

Qinghua Guo

A DISSERTATION

in

Physics and Astronomy

Presented to the Faculties of the University of Pennsylvania

in Partial Fulfillment of the Requirements for the Degree of Doctor of Philosophy

2004

Supervisor of Dissertation

Graduate Group Chairperson

Abstract

Study of Rare Radiative B Decay to $K_2^*(1430)$ Meson Using the *BABAR* Detector

Qinghua Guo

Thesis directed by Professor Larry D. Gladney

Radiative B Meson decay through the $b \to s\gamma$ process has been one of the most sensitive probe of new physics beyond the Standard Model, because of its importance in understanding the phenomenon of *CP* violation, which is believed to be necessary to explain the excess of matter over anti-matter in our universe. The inclusive picture of the $b \to s\gamma$ process is well established; however, our knowledge of the exclusive final states in radiative B meson decays is rather limited. We have investigated one of them, the exclusive, radiative B decay to the charmless $K_2^*(1430)$ meson, in a sample of 88.5×10^6 $B\overline{B}$ events with the *BABAR* detector at the PEP-II storage ring. We present a measurement of the branching fractions $\mathcal{B}(B^0 \to K_2^*(1430)^0\gamma) = (1.22 \pm 0.25 \pm 0.10) \times 10^{-5}$ and $\mathcal{B}(B^+ \to K_2^*(1430)^+\gamma) = (1.45 \pm 0.40 \pm 0.15) \times 10^{-5}$, where the first error is statistical and the second systematic. In addition, we have performed the first search for direct *CP* violation in this decay with the measured asymmetry in $B^0 \to K_2^*(1430)^0\gamma$ of $\mathcal{A}_{CP} = -0.08 \pm 0.15 \pm 0.01$.

Contents

List of Tables

1 Theory

1.1 Introduction

Since the beginning of the 20th century there have been considerable breakthroughs in understanding the world around us from the micro-view. What we learned from the smallest structures we can find will help us to understand the macro scale universe. Even though we have a fundamental physics theory, there are still many unusual, even bizarre, aspects of this picture.

Particle physics is considered to be intimately helpful for study of the early evolution of the universe. We believe the universe originated in a "Big-Bang", from which all particles were created. Today we are left with the cooled remnants, on which the current evolution is dominated by gravity. So our search toward higher energies is also a look backward in time to determine the characteristics of the universe in its earliest stages.

In order to study elementary particles people first turned to radioactive sources and cosmic rays. In addition to these, they nowadays construct bigger and bigger accelerators where these particles are produced at high energies and detectors where they are recorded and examined. Modern experiments require work with many pieces of sophisticated equipment and involve collaborations of many scientists. In Section 2 we will describe the modern elementary particle experiment where our work has been carried out.

Since the 1980s, interest in the study of B mesons has been heating up. Fundamental properties of many elementary particles can be obtained through analysis of B meson decays. The most important of these, CP violation, could help explain the excess of matter over anti-matter in our universe.

1.2 Elementary Particles

In this paper we describe the "Standard Model" (SM) of elementary particles and their interactions. While there were many models constructed during the development of particle physics theories, the Standard Model is the most commonly accepted and consistent theory which successfully explains most of the experimental observations.

Quantum mechanics is the basis for understanding microscopic phenomena. Starting from postulating quantization of spin angular momentum with

	Leptons	Quarks
Family 1	$e\ \bar{\nu}_e$	$d\ u$
Family 2	$\mu\ \bar{\nu}_\mu$	$s\ c$
Family 3	$\tau\ \bar{\nu}_\tau$	$b\ t$
Spin	$\hbar/2\ \hbar/2$	$\hbar/2\ \hbar/2$
Charge	$-e\ 0$	$-e/3\ 2e/3$

Table 1: Fundamental fermions. Three families of lepton and quark doublets presented along with their spin and charge quantum numbers.

the fundamental quantum $\hbar$, one of the most important concepts underlying our analysis of the interactions of particles and fields is the spin-statistics theorem (Pauli 1940). We classify particles into two groups: fermions with half-integer spin ($\hbar/2, 3\hbar/2$,...), and bosons with integer spin (0,$\hbar, 2\hbar$,...).

The statistics obeyed by a particle determines the symmetry of the total wave-function describing a pair of identical particles under interchange. This leads directly to a conclusion that two identical fermions can not exist in the same quantum state–the Pauli principle. On the other hand there is no restriction on the number of bosons which may exist in the same quantum state.

There are two known types of fundamental fermions: leptons and quarks (see Table 1). There are three families with two types of leptons and quarks in each family (doublets), so there are a total of six leptons and six quarks. In addition each lepton or quark has its anti-particle, which has the same mass as the particle, but opposite charge and magnetic moment.

1.3 Interactions

Classical physics describes interaction at a distance in terms of a potential or field due to one particle's interaction with another, while in quantum field theory, the interactions are viewed in terms of the exchange of quanta (gauge bosons) associated with the specific type of interaction. Since the quantum carries energy and momentum, the conservation laws determine that the

Interaction	Gravity	EM	Weak	Strong
Gauge boson	graviton	γ	W^+,W^-,Z^0	g_1,...g_8
Spin-parity	2^+	1^-	$1^-, 1^+$	1^-
Charge	0	0	$\pm e$,0	0
Mass (GeV)	0	0	80-91	0
Range (m)	∞	∞	10^{-18}	$\leqslant 10^{-15}$
Source	Mass	Electric charge	"Weak charge"	"Color charge"
Typical cross-section (m^2 GeV)	-	10^{-33}	10^{-44}	10^{-30}
Typical lifetime (s)	-	10^{-20}	10^{-8}	10^{-23}

Table 2: Fundamental interactions

process only takes place over a time limited by the Uncertainty Principle, $\Delta E * \Delta t \leqslant \hbar$. Such transient quanta are called virtual bosons.

There are four basic types of interactions: gravitational, electromagnetic (EM), weak and strong interactions. (see Table 2).

Only the first two interactions are known in classical physics because of their long-range interaction with potential $\propto 1/r$. Gravitation has negligible effect in the present description of elementary particle physics. It is described in macroscopic physics in terms of the Newtonian constant G, with the magnitude of the force between two equal point masses M given by GM^2/r^2, where r is the separation distance. By comparing with the electrostatic force between singly charged particle, e^2/r^2, the quantity $GM^2/\hbar c$ is seen to be dimensionless. If we take M as the proton mass, then

$$\frac{GM^2}{4\pi\hbar c} = 4.6 \times 10^{-40}, \tag{1}$$

compared with

$$\frac{e^2}{4\pi\hbar c} = \frac{1}{137}. \tag{2}$$

Thus, for the common mass scales in particle physics, the gravitational coupling is negligibly small.

The strong interactions take place between the constituent quarks which exist as bound states, called hadrons. These types of interactions are described by the theory of Quantum Chromodynamics (QCD) with the SU(3) symmetry group of the "color charge". There are three basic "colors" of the SU(3) triplet representation: red (r), blue (b), and green (g), for example. Each quark carries a color and each anti-quark carries an anti-color. Gluons mediate the strong interactions. They belong to a color octet SU(3) representation: $r\bar{b}$, $r\bar{g}$, $b\bar{r}$, $b\bar{g}$, $g\bar{r}$, $g\bar{b}$, $(r\bar{r} - b\bar{b})$, $(r\bar{r} + b\bar{b} - 2g\bar{g})$, for example. Thus there are 8 gluons and they carry "color charge" between quarks as well as between other gluons. All leptons are colorless, so they do not participate in the strong interaction. At high energies (or small distances) the QCD coupling constant α_s is small ($\alpha_s \approx 0.1$ at $E = M_Z$) and perturbative calculations are possible. However at low energies, interaction forces increase indefinitely leading to color charge confinement. Thus free particles can only be colorless and free quarks or gluons have never been observed.

Quantum Electrodynamics (QED) describes electromagnetic interactions in terms of a photon (γ) coupling to charged particles. The small value of the coupling constant $\alpha = e^2/\hbar c = 1/137$ allows calculations in a perturbative series (with the single quantum exchange in the first order) to a very high precision.

The weak interactions take place between all the quarks and lepton constituents; each of them has, so to speak, a "weak charge". Since weak interactions are mediated by massive W or Z bosons, they are short-ranged. This interaction is so feeble however that it is usually swamped by the much stronger electromagnetic and strong interactions, unless these are forbidden by conservation rules. The observable weak interactions therefore either involve neutrinos or quarks with a flavor change ($\Delta S = 1$,$\Delta C = 1$, etc.). While electromagnetic and strong interactions conserve parity, that is, symmetry under spatial inversions, weak interactions do not. Both weak and electromagnetic interactions come naturally from the unified Electroweak theory (EW) with four gauge bosons in the SU(2)×U(1) symmetry group.

Quark	Anti-quark	Flavor	Estimated mass (MeV/c^2)
d	$\bar{d}$	down	3-9
u	$\bar{u}$	up	1.5-5
s	$\bar{s}$	strange	60-170
c	$\bar{c}$	charm	1100-1400
b	$\bar{b}$	bottom	4100-4400
t	$\bar{t}$	top	174300±5100

Table 3: Six quark flavors and masses

1.4 Non-relativistic Quark Model

In the non-relativistic quark model, hadrons are viewed as bound states of constituent quarks. Only two types of bound color-singlet states are known: three-quark baryons with color state (rbg) and quark-antiquark mesons with color state ($r\bar{r} + b\bar{b} + g\bar{g}$). Hadron flavor quantum numbers are defined by constituent quark flavors with six basic types, as listed in Table 3.

The six different flavors may be considered as different states of the same quark. With n flavors under consideration one has SU(n) flavor symmetry. Flavor symmetry is broken because of the quark mass difference and it is a relatively good approximation for the light quarks only (for example SU(2) isospin invariance for u and d quark flavors and SU(3) invariance for u, d, s quarks).

Hadrons are usually presented as SU(n) flavor multiplet members. The two lowest baryon states are well known as proton (p) made of uud and neutron (n) made of udd (they form an SU(2) doublet). There are many other baryon resonance states known as $\Delta, \Lambda, K^*(892), K_2^*(1430)$, etc. We will discuss some of them in more detail because they are the subject of this work.

All mesons are bound states of a quark and an anti-quark and can be classified by the quark flavors, angular momentum quantum numbers: L, S, J, and radial quantum numbers n. The lowest states would have $L = 0$ (no orbital angular momentum), $n = 1$ (no radial excitation), and $J = S = 0$

Quark content	Pseudo-scalar	Vector
$u\bar{d}$, $(u\bar{u}-d\bar{d})$, $d\bar{u}$	$\pi^{\pm}$, π^0	$\rho^{\pm}$, ρ^0
$(u\bar{u}+d\bar{d})$& $s\bar{s}$	η', η	ω, ϕ
$\bar{s}u$, $s\bar{u}$, $\bar{s}d$, $s\bar{d}$	$K^{\pm}$,K^0,$\bar{K}^0$	$K^{*\pm}$,K^{*0},$\bar{K}^{*0}$
$c\bar{d}$, $\bar{c}d$, $c\bar{u}$, $\bar{c}u$	$D^{\pm}$, D^0, $\bar{D}^0$	$D^{*\pm}$,D^{*0},$\bar{D}^{*0}$
$c\bar{s}$, $\bar{c}s$	D_s^+, D_s^-	D_s^{*+}, D_s^{*-}
$c\bar{c}$	η_c	J/ψ
$\bar{b}u$, $b\bar{u}$, $\bar{b}d$, $b\bar{d}$	$B^{\pm}$,B^0,$\bar{B}^0$	$B^{*\pm}$,B^{*0},$\bar{B}^{*0}$
$\bar{b}s$, $b\bar{s}$	B_s^0, B_s^0	B_s^{*0}, $\bar{B}_s^{*0}$
$b\bar{b}$	η_b	$\Upsilon(1S)$

Table 4: Pseudo-scalar and Vector meson states

(pseudo-scalar mesons) or $J = S = 1$ (vector mesons), or even higher state $J = S = 2$ (tensor mesons). Examples of such known states are presented in Table 4. The first line in the table presents SU(2) triplets (isospin $I = 1$) with u and q quarks. The next two lines present SU(3) octet and singlet states with u, d and s quarks.

1.5 Units in Particle Physics

Although the fundamental units in classical physics are of length, mass, and time, in meters, kilograms and seconds (MKS system), they are not good units to be used in particle physics, where lengths are typically 10^{-15} m and masses $10^{-27}kg$.

Lengths in particle physics are usually quoted in terms of the femtometer or fermi ($1fm = 10^{-15}m$), and cross section in terms of the barn ($1b = 10^{-28}m^2$). The unit of energy is based on the electron volt ($1\,\mathrm{eV} = 1.6\times10^{-19}$ joules) with the larger units MeV, GeV. Masses are usually measured by MeV/c^2, meaning that if the mass is M, the rest energy is $Mc^2\,\mathrm{MeV}$.

In calculations, the quantities $\hbar = h/2\pi$ and c occurs frequently, and it

is often advantageous to use a system with units in which $\hbar = c = 1$. To achieve this goal, we choose some standard m_0 (e.g., the proton mass) as the unit: $m_0 = 1$. The natural unit of length is then the Compton wavelength of the standard particle: $\lambda_0 = \hbar/m_0 c = 1$;

that of time is $t_0 = \lambda_0/c = \hbar/m_0 c^2 = 1$, and that of energy is $E_0 = mc^2 = 1$. In these units, it's seen that $\hbar = c = 1$.

Throughout this text we shall be dealing with the coupling of charges–strong, electric and weak–to mediation bosons. In MKS units, electric charge, e, is measured in Coulombs and the fine-structure constant is then given by $\alpha = e^2/(4\pi\epsilon_0\hbar c) \simeq= 1/137$.

1.6 CP Violation in the B Meson System

While CP violation effects have been observed in the neutral K system, they are very small and uncertainties in the theoretical calculations prevent reliable tests of their origin. On the other hand the B meson system offers excellent prospects for CP violation measurements. Large effects are expected and measurement of the unitary triangle parameters is possible. In the late 1980s, studies [1] indicated that the best source of B mesons for such a physics program was an electron-positron collider, operated at $\Upsilon(4S)$ resonance, but in an asymmetric beam energy mode.

Currently there are three B-factories: PEP-II at SLAC [2], KEKB at KEK [3] and CESR Phase III at Cornell University [4]. All of them are electron-positron colliders.

PEP-II and KEKB are two-ring colliders now being run at SLAC and KEK, respectively. This type of collider consists of two rings: one for positrons and the other for electrons. Since the energy of electrons and positrons are different (3.1 GeV positrons and 9 GeV electrons at PEP-II and 3.5 GeV positrons and 8 GeV electrons at KEKB), these colliders are called asymmetric-energy colliders. Electrons have higher energy than positrons in order to avoid ion trapping, which becomes much serious at low energies. The positron ring, therefore, is called the low-energy ring (LER) and the electron ring is the high-energy ring (HER). LER and HER have a common region of a few meter lengths around an interaction point (IP), where electrons and positrons collide. The detectors surround the IP. The *BABAR* B-Factory construction was started in 1994 and commissioning started in 1999.

CESR is a symmetric-energy, single-ring collider with a beam energy

of 5.3 GeV. CESR started its operation in 1981 and has been continuously improved and upgraded. The most recent upgrade, from CESR Phase II to Phase III together with the upgrade of CLEO II to CLEO III, was completed in 1998 [5].

The most salient features of these B-Factories is that all of them aim at achieving luminosities larger than $10^{33}\,\mathrm{cm}^{-2}\mathrm{s}^{-1}$. The luminosity of an electron-positron collider is given by

$$L = 2.17 \times 10^3 4\xi(1+r)(\frac{E \times I}{\beta_y^*})^{\pm} \tag{3}$$

where L stands for luminosity, ξ, the beam-beam tune-shift, r, the ratio of vertical beam size to horizon beam size at the IP, I, beam current in units of A, E, beam energy in GeV, and β_y^*, beta-value at the IP. The signs + and − mean that this formula is applicable both to electron and positron rings.

All B-Factory designs assume that the beam-beam tune-shift ξ is between 0.03 and 0.05 and β_y^* between 1 cm and 2 cm, r in the order of a few %. If we assume $L = 3 \times 10^{33}\,\mathrm{cm}^{-2}\mathrm{s}^{-1}$, $E = 5\,\mathrm{GeV}$,$\xi = 0.03$, and $\beta_y^* = 1\,\mathrm{cm}$, we find that we need to store $1.3A$ in a ring. The main parameters of these B-Factories are summarized in Table 5.

1.7 The Radiative Penguin Decays

Flavor-changing neutral current (FCNC) transitions involving the B-meson provide unique opportunities to study electroweak theory in higher orders. Our physics analysis has been focused on the search for $b \to s$ quark decays, starting with the search for exclusive decay modes through the electromagnetic penguin process $b \to s\gamma$. In the Standard Model (SM), these decays are forbidden at the tree level. For example, there is no direct coupling between the b quark and the s or d quarks. Effective FCNC are induced by loop (or "penguin") diagrams, where a quark emits and re-absorbs a W, thus changing flavor twice as in the $b \to s\gamma$ transition depicted in Figure 1.

With large samples of B mesons and increasingly powerful background-suppression techniques, experimenters have succeeded in measuring Cabibbo-Kobayashi-Maskawa (CKM)-favored penguins. Theory has also made good progress in computing the decay rates; in particular, recent completion of the NLO correction [6] to the inclusive $b \to s\gamma$ decay rate has intensified experimental efforts to further improve the measurement. Comparisons of

	PEP-II	KEKB	CESR Ph.3
Luminosity($10^{33}\,\mathrm{cm}^{-2}\mathrm{s}^{-1}$)	10	10	1.55
Energy, E_+/E_-(GeV)	3.1/9	3.5/8	5.3/5.3
Circumference, C(m)	2199	3016	768
Total current, $I_+/I_-(A)$	2.14/0.99	2.6/1.1	0.5/0.5
Number of bunches	1317	5000	45 (5× 9)
Bunch separation (m)	1.14	0.6	4.2
Bunch current, I_+/I_-(mA)	1.3/0.6	0.52/0.22	11.1/11.1
Crossing angle ($mrad$)	0	2×11	2×2.3
Beam-beam tune shiftξ_x/ξ_y	0.03/0.03	0.039/0.052	0.0364/0.04
IP beta, β_x^*(cm)/β_{y}^*(cm)	37.5/1.5(LER)	33/1	100/1.5
	50/1.0(HER)		100/1.8

Table 5: Main parameters of B-factories

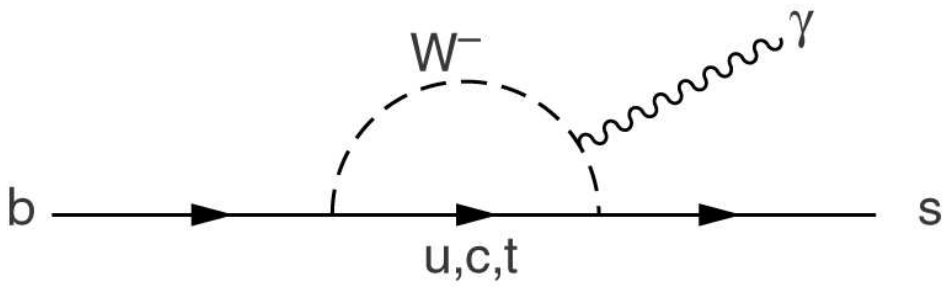

Figure 1: $b \to s\gamma$ "penguin" diagram.

this decay rate between theory and experiment place strong constraints on physics beyond the Standard Model.

The discovery of $B \to K^*(892)\gamma$ by the CLEO collaboration [7] verified the existence of penguins. They also reported evidence for $B \to K_2^*(1430)\gamma$, which was confirmed by the BELLE collaboration [8]. The inclusive decay rate has been studied both experimentally [9] and theoretically [10]; detailed knowledge about the resonant modes with masses higher than $K^*(892)$, for example, the $B \to K_2^*(1430)\gamma$ decay, will help to understand the inclusive $b \to s\gamma$ branching fraction in terms of the sum over exclusive modes. Furthermore, with the inclusive branching fraction studied extensively, there is another unique feature of this process within the SM which drew only moderate theoretical attention and has not yet been tested—the photon helicity. Namely, the emitted photons are left-handed in B^- and $\bar{B}^0$ decays and right-handed in B^+ and B^0 decays. In the SM the photon emitted from $b \to s\gamma$ is predominantly left-handed because the recoil s quark which couples to a W meson is left-chiral. This prediction of *maximum parity violation* holds in the SM with small corrections on the order of m_s/m_b. It applies to

the exclusive radiative decays when including the long-distance effects [11]. Though measurements of the inclusive radiative decay rate agree with SM calculations, no evidence exists for the helicity of the photons in inclusive and exclusive decays.

In several extensions of the SM the photon in $b \to s\gamma$ acquires a significant right-handed component due to a chirality flip along a heavy fermion line in the electroweak loop process. Two well-known examples of such extensions are the $SU(2)_L \times SU(2)_R \times U(1)$ left-right symmetric (LR) model and the unconstrained Minimal Super-symmetric Standard Model (MSSM) [12]. In the LR model, the chirality flip along the t quark line in the loop involves $W_L - W_R$ mixing [13], while in the MSSM a chirality flip along the gluino line in the loop involves left-right squark mixing. In both types of modes it was found that, in certain allowed regions of the parameter space, the photons emitted in $b \to s\gamma$ can be largely right-handed polarized, without affecting the SM prediction for the inclusive radiative decay rate. This situation calls for an independent measurement of the photon helicity.

Several ways [14] were suggested in the past five years to look for signals of physics beyond the SM through photon helicity effects in $B \to X_s\gamma$. One recent method [18], which proposes the direct measurement on a fundamental parameter in the effective radiative weak Hamiltonian describing the photon polarization, based on radiative B decays to an excited kaon resonance, like $B^+ \to (K_1^+(1400) \to K^0\pi^+\pi^0)\gamma$ and $B^0 \to (K_1^0(1400) \to K^+\pi^-\pi^0)\gamma$, makes use of angular correlations among the three-body decay products of the excited kaons. The up-down asymmetry of the photon momentum with respect to the $K\pi\pi$ decay plane measures the photon polarization with a rather high

efficiency. Such an asymmetry can be measured at currently operating B factories assuming the radiative branching ratio into $K_1(1400)$ to be around 10^{-5}.

1.8 Theoretical Predictions

The effective Hamiltonian for the decays $B \to X_s\gamma$ can be found in many places, e.g. [15]. It is derived by integrating out the top quark and W-boson at the same scale $u \approx M_w$. An appropriate operator basis for the effective Hamiltonian consists of four-quark operators and the magnetic moment type operators of dimension six ($O_1 - O_8$). Higher dimensional operators are suppressed by powers of the masses of the heavy quarks.

The Standard Model rate for the inclusive $b \to s\gamma$ process has been calculated to next-to-leading order by Buras et al., the result being:
$\mathcal{B}(b \to s\gamma) = (3.57 \pm 0.30) \times 10^{-4}$.

For the $B \to K^{**}\gamma$ decays only the operator O_7 contributes, so that

$$H_{eff} = -\frac{4G_F}{\sqrt{2}} V_{tb}V_{ts}^* C_7(m_b) O_7(m_b). \tag{4}$$

Here, O_7 is given by

$$O_7 = \frac{e}{32\pi^2} F_{\mu\nu}[m_b \bar{s}\sigma^{\mu\nu}(1+\gamma_5)b + m_s \bar{s}\sigma^{\mu\nu}(1-\gamma_5)b], \tag{5}$$

with $\sigma^{\mu\nu} = \frac{i}{2}[\gamma^\mu, \gamma^\nu]$. The explicit expression for the Wilson coefficient $C_7(m_b)$ as a function of $\frac{{m_t}^2}{M_W}$ can be found in [16]. The value of C_7 can be calculated perturbatively at the mass scale $\mu = M_W$. The evolution from M_W down to a mass scale $\mu = m_b$ introduces large QCD corrections. This

procedure also introduces large theoretical uncertainties, primarily due to the choice of the renormalization scale u (taken above as m_b), which can be as large as 25%.

Calculations of exclusive modes which contribute to the inclusive decay rate have also been done by many theorists [19] [20] [21] [22] [23]. Predictions of the percentage contribution of different K^*∗ into the inclusive branching ratio are listed in Table 6. The calculations in all these papers used Heavy Quark Effective Theory (HQET) to determine the branching fractions. The significant difference in the branching fractions are due solely to [21] [22] [23]'s use of an improved calculation of the form factors, which describes the wave-function overlap between initial and final state mesons presented in [25].

Mode J^P	[19]	[20]	[21]	[22]	[23]
$B \to K\gamma$	forb.	forb.	forb.	forb.	forb.
$B \to K^*(892)\gamma$ 1^-	4.5	3.5-12.2	16.8± 6.4	15 ± 3	10.0 ± 4.0
$B \to K_1(1270)\gamma$ 1^+	forb.	4.5-10.1	4.3± 1.6	1.5 ± 0.5	2.0 ± 0.8
$B \to K_1(1400)\gamma$ 1^+	forb.	6.0-13.0	2.1± 0.9	2.6 ± 0.6	0.9 ± 0.4
$B \to K^*(1410)\gamma$ 1^-	7.3	7.2-10.6	4.1± 0.6		0.8 ± 0.4
$B \to K_2^*(1430)\gamma$ 2^+	6.0	17.3-37.1	6.2± 2.9	5.7 ± 1.2	5.0 ± 2.0
$B \to K_2(1580)\gamma$	4.4	1.8-2.6	0.46±0.11		
$B \to K_1(1650)\gamma$ 1^+			0.47±0.16		0.8 ± 0.3
$B \to K^*(1680)\gamma$ 1^-	0.9	1.1−1.5	0.5± 0.2		0.7 ± 0.3

Table 6: Predicted percentage contributions (%) from exclusive modes

2 Overview of *BABAR* Project

The purpose of the high energy physics experiment is to study properties of the elementary particles. Most of these particles are not found around us. Large accelerators are constructed to produce these particles. To study the collisions produced by these accelerators, physicists must construct massive detectors having hundreds of thousands or even millions of channels of electronics. Within such detectors, when a particle in a primary beam from the accelerator collides with either a stationary target or, in a colliding beam accelerator, with a particle from the other particle beam, many thousands of electronic elements record information about the "secondary elementary particles" produced in the collision. The tracking system records the time and position at which a charged particle passes near one of the detector elements–information that is used to reconstruct the particle's trajectory, or track. Calorimeters measure particle energies. Vertex detectors provide very precise tracking near the collision region to allow determination of the points from which various groups of tracks originated. Still other elements can be used to identify what kind of particle (electron, pion, kaon and so on) made the track. Together, information from these elements allows particle physicists to reconstruct what occurred in a particular event.

We will introduce some specifics about the detector (PEP-II) we used for our research project, *BABAR*.

2.1 PEP-II

The primary physics goal of the *BABAR* experiment is the systematic study of CP asymmetries in decays of the B^0 to CP eigenstates. The secondary goals are to explore the wide range of other B physics, charm physics, τ physics, two-photon physics, and rare processes that becomes accessible with the high luminosity of the PEP-II B Factory. The design of the detector is optimized for CP violation studies, but it is also well suited for these other physics topics.

The PEP-II B Factory is an asymmetric e^+e^- collider designed to operate at a luminosity of $3 \times 10^{33} cm^{-2} s^{-1}$ and above, at a center of mass energy of 10.58 GeV, the mass of the $\Upsilon(4S)$ resonance. This resonance decays exclusively to $B^0\overline{B}^0$ and B^+B^- pairs and thus provides an ideal laboratory for the study of B mesons. In PEP-II, the electron beam of 9.0 GeV collides head-on with the positron beam of 3.1 GeV resulting in a Lorentz boost to the $\Upsilon(4S)$ resonance of $\beta\gamma = 0.56$. The general differential cross section for annihilation of an electron-positron pair to fermion-anti-fermion final state $e^+e^- \rightarrow f\bar{f}$ with energy E_{beam} through a single photon into two relativistic fermions of charge Q_f is

$$\frac{d\sigma}{d\Omega}(e^+e^- \rightarrow f\bar{f}) = \frac{\alpha^2}{16(E_{beam})^2}(1+\cos^2\theta){Q^2}_f, \tag{6}$$

where the angle θ is defined by the fermion direction with respect to the beam angle in the lab frame. The final state may involve all fundamental fermions—leptons and quarks that are allowed by energy conservation. For exact calculations, additional radiative corrections are needed.

The $\Upsilon(4S)$ resonance with a peak cross-section 1.08 nb is particularly

important because it decays into $B\overline{B}$ pairs. We note that the angular distribution of the B direction with respect to the beam axis in the lab frame is:

$$\frac{d\sigma}{d\Omega}(e^+e^- \to \Upsilon(4S) \to B\overline{B}) \propto \sin^2\theta_B. \quad (7)$$

Thus, if the e^+e^- energy is tuned to $\Upsilon(4S)$ resonance energy of 10.58 GeV, $B\overline{B}$ pairs can be produced at a rate of about 1/3 of the continuum hadronic production. This is realized at the PEP-II collider.

2.2 Detector Overview

The *BABAR* detector is the collaboration's achievement of a large international team of scientists and engineers. The detector surrounds the PEP-II interaction region, and is offset relative to the beam-beam interaction point (IP) by 0.37 m in the direction of the lower energy beam in order to maximize the geometric acceptance for the boosted $\Upsilon(4S)$ decays.

A schematic of the *BABAR*detector is shown in Fig 2. Major subsystems of the detector include:

- A Silicon Vertex Tracker (SVT). This provides precise position information on charged tracks, and also is the sole tracking device for very low-energy charged particles.

- A Drift Chamber (DCH). It is filled with a helium-based gas, in order to try to minimize multiple scattering. It provides the main momentum measurement for charged particles and helps in particle identification through energy loss measurements.

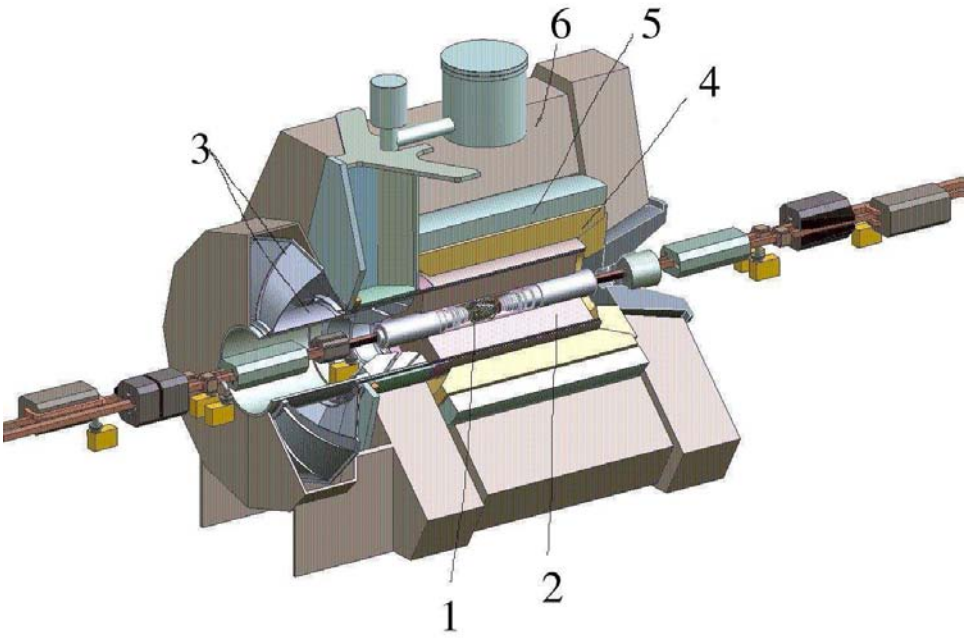

Figure 2: Layout of the *BABAR*detector.

- A Detector of Internally Reflected Cherenkov light (DIRC). This is designed and optimized for a charged hadron particle identification.

- An Electromagnetic Calorimeter (EMC). It is designed to detect electromagnetic showers with excellent energy and angular resolution over the energy range from 20 MeV to 4 GeV. This coverage allows the detection of low energy π^0s and η^0s from B decays and higher energy photons and electrons from electromagnetic, weak and radiative processes. Photons and electrons are measured in the barrel and forward end-cap, consisting of 6580 Thallium-doped CsI crystals.

- A superconducting coil, which provides a 1.5 T solenoid magnetic field.

- An Instrumented Flux Return (IFR) for muon identification down to about 0.6 GeV and neutral hadron identification.

There are 5 layers in the SVT. The inner three layers primarily provide position and angle information for the measurement of the vertex position, the outer two layers provide the coordinate and angle measurements needed for linking SVT and DCH tracks. For charged tracks with momentum $p > 1\,\mathrm{GeV}/c$, the measured transverse momentum with respect to the beam axis (p_T) has the resolution

$$\frac{\sigma_{p_T}}{p_T} = 0.13\% p_T + 0.45\%, \tag{8}$$

where p_T is measured in GeV/c. The electromagnetic calorimeter resolution, σ_E, can be expressed as

$$\frac{\sigma_E}{E} = \frac{2.3\%}{E^{\frac{1}{4}}} \oplus 1.9\%, \tag{9}$$

where the energy E is measured in GeV.

Charged particle identification is provided by the energy loss (dE/dx) in the tracking devices and by an internally reflecting ring-imaging Cherenkov detector. The DIRC transports the Cherenkov light to a water-filled expansion volume equipped with approximately 11,000 photomultiplier tubes. A K/π separation better than 4 standard deviations is achieved for charged tracks with momenta below $3\,\mathrm{GeV}/c$.

An overview [24] of the coverage, the segmentation, and performance of the *BABAR* detector systems is presented in Table 7.

System	θ_1 (θ_2)	#. channels	#. layer	Segmentation	Performance
SVT	20.1° (-29.8°)	150K	5	50-100 μm 100-200 μm z	$\sigma_{d_0} = 55\,\mu$m $\sigma_{z_0} = 65\,\mu$m
DCH	17.2° (-27.4°)	7104	40	6-8 mm drift distance	$\sigma_\phi = 1\ mrad$ $\sigma_{tan\lambda} = 0.001$ $\sigma_{p_t}/p_t = 0.47\%$ $\sigma(dE/dx) = 7.5\%$
DIRC	25.5° (-38.6°)	10752	1	$35 \times 17\,\mathrm{mm}^2$ ($r\delta\phi \times \delta r$) 144 bars	$\sigma_{\theta_c} = 2.5\ mrad$ per track
EMC(C)	27.1° (-39.2°)	2×5760	1	$47 \times 47\,\mathrm{mm}^2$ 5760 crystals	$\sigma_E/E = 3.0\%$ $\sigma_\phi = 3.9\ mrad$
EMC(F)	15.8° (-39.2°)	2×820	1	820 crystals	$\sigma_\theta = 3.9\ mrad$
IFR(C)	47° (-57°)	22K+2K	21	22-38 mm	90%$\mu^\pm$eff. $6-8\%\pi^\pm$mis-id
IFR(F)	20° (47°)	14.5K	18	28-38 mm	(loose selection, 1.5-3.0 GeV/c)
IFR(F)	-57° (-26°)	14.5K	18	28-38 mm	

Table 7: Overview of the coverage, segmentation, and performance of the *BABAR* detector systems

2.3 The Monte Carlo Simulation

Monte Carlo (MC) modeling is frequently used in science to predict the probability with which a random process will occur. It is especially important in elementary particle physics when predictions calculated analytically are impractical because of the very complex detector systems. Computer simulations of all the processes starting from the elementary particle decays and ending with detector subsystem response are used.

We use Monte Carlo simulations of the *BABAR* detector based on GEANT 4 [17] to optimize our selection criteria and to determine signal efficiencies. These simulations take into account the varying detector conditions and beam backgrounds during the data-taking period simulated.

2.4 Blind Analysis

In our study, the physics result is kept hidden until the analysis is essentially complete. This is called "blind analysis".

The major motivation for a blind analysis is to adopt a technique to avoid or minimize the potential for experimenter bias; the unconscious biasing of measurement, perhaps toward prior results or theoretical predictions. For example, the point at which the decision is made to stop working and present one's result can be influenced by the value of the result itself, and how it compares with prior results or predictions. In a blind analysis the decision to stop and publish is made based on external checks, and not on the numerical value of the result. Another example is that choices about the data to include, or the cuts to use, can be subtly biased, if the effect of these choices on the

result is known. A blind analysis ensures that such choices affecting the data sample do not bias the result. In general, the background estimation, the selection cuts, and the acceptance calculation should all be fixed prior to looking into the signal box.

Of course, a blind analysis does not necessarily eliminate the possibility of mistakes, like overlooking a major source of systematic error or a flaw in the analysis. Nor is a non-blind analysis necessarily flawed. However, given that techniques exist to reduce or eliminate the possibility of experimenter bias from affecting our physics results, and that these techniques do not incur significant burden on the progress of analysis, it is strongly recommended to use the blind analysis where possible.

3 Event Reconstruction

3.1 Global Event Requirement

We require an event to be classified as hadronic using track multiplicity to remove low multiplicity events such as Bhabhas and dimuons.

There must be at least *three* tracks that each satisfy the " *GoodTracksLoose*" criteria (described in Appendix A). In addition to the *GoodTracksLoose* requirement, the second Fox-Wolfram moment [27], R_2, for the event must be less than 0.9. This is to remove Bhabha, radiative Bhabha and τ events that remain after satisfying the track multiplicity requirement. The distribution of multiplicity of tracks and R_2 in signal $B^0 \to K_2^*(1430)^0\gamma$ MC can be seen in Fig. 3.

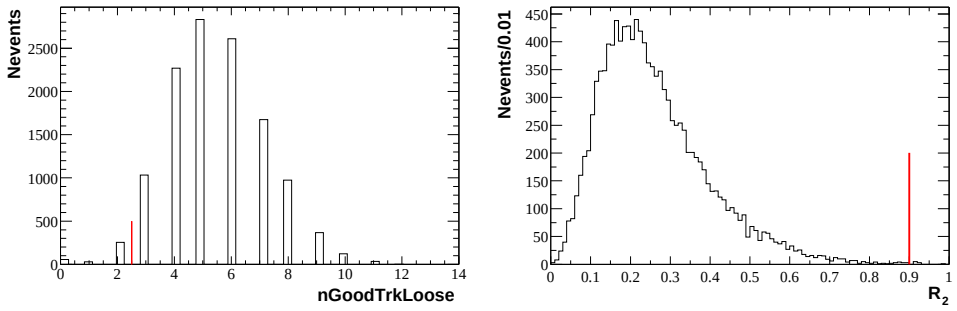

Figure 3: The number of tracks satisfying the global event track criteria and R_2 for $B^0 \to K_2^*(1430)^0\gamma$ ($K_2^{*0}(1430) \to K^+\pi^-$)

We next require the presence of a high energy photon. There should be at least one *GoodPhotonLoose* (defined in Appendix B) candidate with energy between 1.5 and 3.5 GeV in the center-of-mass (CMS) frame.

The detailed efficiencies for each global variable cut are listed in Table 8.

Table 8: Global variables cut efficiencies

Cut	$B^0 \to K_2^{*0}\gamma$ $(K_2^{*0} \to K^+\pi^-)$	$B^+ \to K_2^{*+}\gamma$ $(K_2^{*+} \to K_S\pi^+)$	$B^+ \to K_2^{*+}\gamma$ $(K_2^{*+} \to K^+\pi^0)$
$nTrk > 2$	97.2 %	98.0%	93.1 %
$R_2 < 0.9$	99.97 %	99.98 %	99.84 %
$1.5 < eMax < 3.5\,\mathrm{GeV}$	80.3 %	78.0%	80.3 %
Cumulative efficiency	78.1 %	76.4 %	74.6 %

3.2 Photon Candidate Selection

3.2.1 Photon Quality

A photon candidate is defined as a localized energy maximum well contained within the calorimeter acceptance, $-0.77 < \cos\theta < 0.96$, where θ is the polar angle to the detector axis. It must have a lateral energy profile consistent with a photon shower. The photon shower must be isolated by 25 cm from all other showers, both neutral and charged. To suppress photons from $\pi^0(\eta)$ decays, we veto any photon that combines with another photon of energy greater than 50 (250) MeV to form a $\gamma\gamma$ invariant mass in the range 115 (508) $< M_{\gamma\gamma} <$ 155 (588) MeV/c^2. As a summary, We require:

- $1.8\,\mathrm{GeV} < {E^*}_\gamma < 2.75\,\mathrm{GeV}$
- $-0.77 < \cos\theta_\gamma < 0.96$
- Cluster does not contain a noisy or dead crystal (no bad channels)
- $N_{crystals} > 4$

- Second moment$< 0.002\,\mathrm{GeV}/c$
- Distance to nearest shower > 25 cm

Figure 4 5 6 7 show the related distributions of the above variables from the signal MC.

3.2.2 π^0 and η Veto

We apply vetoes to remove some high energy photons from π^0 and η decays by combining the high energy photon with each of the other neutral bumps candidates in the event with energy greater than 50 MeV (250 MeV in the η veto case). We veto invariant masses in the range:
$115 < M_{\gamma\gamma} < 155\,\mathrm{MeV}/c^2$ for the π^0 case and
$508 < M_{\gamma\gamma} < 588\,\mathrm{MeV}/c^2$ for the η case.

Figures 8 and 9 describe the π^0 and η mass window and the cuts.

The detailed efficiencies according to the above cuts are listed in Table 9. There is an adjustment on the efficiency because of the difference between data and MC samples [31].

3.3 $K_2^*(1430)$ Daughter Candidates Selection

A track is identified as a kaon if its trajectory traverses the DIRC radiators, and the detected Cherenkov photons are consistent in time and angle with a kaon of the measured track momentum. Particle identification (PID) is provided by the energy loss (dE/dx) in the tracking devices and by the DIRC to help the pickup of kaon candidates. A charged pion is selected from

Table 9: Photon selection efficiencies

Cut	$B^0 \to K_2^{*0}\gamma$ $(K_2^{*0} \to K^+\pi^-)$	$B^+ \to K_2^{*+}\gamma$ $(K_2^{*+} \to K_S\pi^+)$	$B^+ \to K_2^{*+}\gamma$ $(K_2^{*+} \to K^+\pi^0)$
Geometric Acceptance $(-0.77 < \cos\theta_\gamma < 0.96)$	94.3	96.6	93.5
No problematic channels	97.3	97.2	97.5
$1.8 < E_\gamma^* < 2.75$	98.2	98.5	97.5
$nCrystal > 4$	100.0	100.0	100.0
$P_{second} < 0.002\,\mathrm{GeV}/c$	99.2	98.8	98.6
25 cm Isolation	90.6	90.0	91.1
π^0 veto:($E_{\gamma 2} > 50\,\mathrm{MeV}$, $115 < m_{\gamma\gamma} < 155\,\mathrm{MeV}/c^2$)	96.0	95.4	95.3
η veto:($E_{\gamma 2} > 250\,\mathrm{MeV}$, $508 < m_{\gamma\gamma} < 588\,\mathrm{MeV}/c^2$)	95.9	95.5	95.9
Data/MC correction	97.5	97.5	97.5
Cumulative Efficiency	72.6	73.0	71.2

the *GoodTracksLoose* list and defined as a track that is not identified as a kaon or an electron. The kaon and pion lab momenta and angle distributions are shown in Fig. 10. The transverse momenta are shown in Fig. 11, the two bumps in the distributions originate from the spin $J = 2$ of the $K_2^*(1430)$.

There is also a requirement on the vertex probability in the reconstruction of the neutral $K_2^*(1430)$ candidate from the $K\pi$ pair, which is shown in Fig. 12.

We formed a K_S list for the reconstruction of the $K_S \to \pi^+\pi^-$ candidates. The list is formed from all pairs of oppositely charged tracks, assigned pion masses, which fail the kaon and electron PID criteria. We apply the following cuts on the K_S given by the list to suppress non-K_S backgrounds:

- a mass cut $489 < M_{\pi\pi} < 507\,\mathrm{MeV}/c^2$,
- a decay length cut, $L_{\mathrm{flight}} > 2\mathrm{mm}$,
- Vertex position to momentum direction angle cut, $\Delta\theta < 0.05$

The distributions and cuts for the above 3 variables are shown in Fig. 13, please note that the Y-axis of the latter two plots are in log scale.

We form a neutral pion list using $\pi^0 \to \gamma\gamma$ decays. The π^0's are made by pairs of photons from the *GoodPhotonLoose* list and a mass constraint fit is applied. The following criteria are satisfied in the reconstruction:

- $E_\gamma > 50\,\mathrm{MeV}$
- $\gamma\gamma$ opening angle $\theta < 36^\circ$
- $115 < M_{\gamma\gamma} < 150\,\mathrm{MeV}/c^2$

The open angle comparison between truth-matched and fake π^0s is shown in Fig. 14.

The detailed efficiencies according to the above cuts are listed in Table 10, in which "GTL" represents "GoodTrackLoose" and "GPL" represents "GoodPhotonLoose".

3.4 Efficiency Correction

The tracking group has made extensive studies of the efficiency for finding these tracks in data, and have come up with a prescription for correcting for the difference between the efficiency in MC and data by comparing SVT and DCH track efficiencies. The Tracking Efficiency Task Force [34] and [32] have determined the relative efficiencies between MC and data for the GoodTrackLoose selection as a function of the momentum of the track (magnitude and direction) and the overall track multiplicity in the event. These corrections have been applied on a track-by-track basis to obtain a correction of $-2.3 \pm 2.4\%$ (97.7% efficiency in data relative to the MC) for the tracking efficiency in the $K_2^{*0}(1430) \to K^+\pi^-$mode for the two tracks and $-1.1 \pm 1.2\%$ (98.9% efficiency) for the $K^\pm, \pi^\pm$ in the charged modes. The correction for the K_S efficiency is a flat value of 98%; and correction for the π^0 is found to be $-5.0 \pm 2.5\%$. The uncertainty on these corrections are considered systematic uncertainties on the overall signal reconstruction efficiency (see Section 8.3).

3.5 K^{**} Invariant Mass

Figure 15 shows the invariant mass plot from the signal Monte Carlo samples.

Table 10: K^{**} reconstruction efficiencies

Cut	$B^0 \to K_2^{*0}\gamma$ $(K_2^{*0} \to K^+\pi^-)$	$B^+ \to K_2^{*+}\gamma$ $(K_2^{*+} \to K_S\pi^+)$	$B^+ \to K_2^{*+}\gamma$ $(K_2^{*+} \to K^+\pi^0)$
Kaon GTL^* reconstructed	85.5	-	84.6
Kaon PID selection	80.3	-	82.2
π GTL^* reconstructed	91.2	87.8	-
π kaon-PID veto	95.8	98.5	-
π electron-PID veto	97.4	99.0	-
$K\pi$ vertex prob. > 0.001	95.6	-	-
Track efficiency correction	97.7	98.9	98.9
K_S tracks reconstructed	-	89.0	-
K_S tracks passing vetos	-	95.4	-
$489 < M_{\pi^+\pi^-} < 507\,\mathrm{MeV}/c^2$	-	76.8	-
K_S decay length$> 0.2\,\mathrm{cm}$	-	95.1	-
K_S vertex angle< 0.05	-	84.1	-
π^0 daughters in GPL^*	-	-	81.5
π^0 daughters $E_\gamma > 50\,\mathrm{MeV}$	-	-	89.5
$\gamma\gamma$ Open Angle$< 36^\circ$	-	-	85.2
$115 < M_{\gamma\gamma} < 150\,\mathrm{MeV}/c^2$	-	-	88.6
K_S Data/MC correction	-	98.0	-
π^0 Data/MC correction	-	-	95.0
Cumulative Efficiency	54.6	43.5	36.0

The full width from the PDG [28] and the fitted values (with relativistic Breit-Weigner function) are listed in Table 11 .

Mode	$B^0 \to K_2^*(1430)^0\gamma$	$B^+ \to K_2^*(1430)^+\gamma$
PDG [28] mass	$1432.4 \pm 1.3\,\mathrm{MeV}/c^2$	$1425.6 \pm 1.5\,\mathrm{MeV}/c^2$
Fitted mass	$1430.2 \pm 1.2\,\mathrm{MeV}/c^2$	$1422.5 \pm 1.3\,\mathrm{MeV}/c^2$
PDG [28] width	$109 \pm 5\,\mathrm{MeV}/c^2$	$98.5 \pm 2.7\,\mathrm{MeV}/c^2$
Fitted width	$108.2 \pm 2.6\,\mathrm{MeV}/c^2$	$102.5 \pm 2.8\,\mathrm{MeV}/c^2$

Table 11: $K_2{}^*(1430)$ invariant mass

We are going to apply roughly a 1.1σ cut, $\pm 120\,\mathrm{MeV}/c^2$, for the neutral mode and $\pm 110\,\mathrm{MeV}/c^2$ for the charged modes, from the PDG value on the invariant mass.

3.6 $K_2^*(1430)$ Helicity Angle

The $K_2^*(1430)$ helicity angle is the angle of the $K^\pm/K_s^0$ computed in the rest frame of the $K_2^*(1430)$ with respect to the flight direction of the $K_2^*(1430)$. Fig. 16 shows a comparison of the helicity angle distribution between signal, continuum background Monte Carlo , and the off-resonance data.

Since $K_2{}^*(1430)$ is a tensor hadron, the kaon helicity angle in $B^0 \to K_2^*(1430)^0\gamma$ decay has a distribution following a $\sin^2\theta_H^*\cos^2\theta_H^*$ function.

The peak in the background distribution at $|\cos\theta_H| = 1$ results from combinations of the kaon candidate with slow tracks in the event.

We are going to use the $|\cos\theta_H|$ distribution because of the statistics concern. The $|\cos\theta_H|$ from the signal MC is show in Fig. 17, which is fitted

with a function mentioned later in Section 6.1.

3.7 B Reconstruction: ΔE and $m_{\rm ES}$

Since the B mesons are produced via $e^+e^- \to \Upsilon(4S) \to B\overline{B}$, the energy of the B meson in the $\Upsilon(4S)$ rest frame is given by the beam energy in the center-of-mass frame, $\sqrt{s}/2$, which is known much more precisely than the energy of the B candidate. Therefore, to isolate the B meson signal, we use two kinematic variables: the difference between the reconstructed energy of the B candidate and the beam energy in the center-of-mass frame (ΔE), and the beam energy substituted mass ($m_{\rm ES}$).

The energy of the B meson is equal to the CMS energy of the beam E_{beam} which is precisely known. We define:

$$\Delta E = E_{\rm B} - E_{\rm beam} \tag{10}$$

where

$$E_{\rm B} = E_{\rm K} + E_{\pi} + E_{\gamma} \tag{11}$$

ΔE should have a distribution centered at zero with a width dominated by the experimental resolution (in this case, the photon energy resolution). We keep the reconstructed B candidates with $-0.5\,{\rm GeV} < \Delta E < 0.5\,{\rm GeV}$, and select $-0.3\,{\rm GeV} < \Delta E < 0.3\,{\rm GeV}$ as the range to be fitted on ΔE.

The second is the beam energy substituted mass ($m_{\rm ES}$), which is defined as $m_{\rm ES}^{\rm raw} = \sqrt{E_{\rm beam}^2 - p_B^2}$, where $E_{\rm beam} = \sqrt{s}/2$, $\vec{p}_B = \vec{p}_{K^*} + \vec{p}_{\gamma}$ with $\vec{p}_{K^*}$ and $\vec{p}_{\gamma}$ representing the momentum of the K_2^* and photon. For signal events, ΔE and $m_{\rm ES}$ peak at zero and the B meson mass, m_B, respectively. For the modes containing a single photon candidate, namely $K^+\pi^-$ and $K_S^0\pi^+$, we

adopt a technique from the CLEO analysis [7], which rescales the measured photon energy E^*_γ with a factor κ, determined for each event, such that $E_{K^*} + \kappa E_\gamma - E_{\rm beam} = 0$; this improves the original $m_{\rm ES}$ ($m^{\rm raw}_{\rm ES}$) resolution from 3.0 to 2.7 MeV/c^2. The effect on the $m_{\rm ES}$ signal shape is to remove a non-Gaussian tail. Fig. 18 shows the change before and after rescaling the gamma energy. A "Crystal-Ball" function, which is described in section 6.1, is used for the fitting.

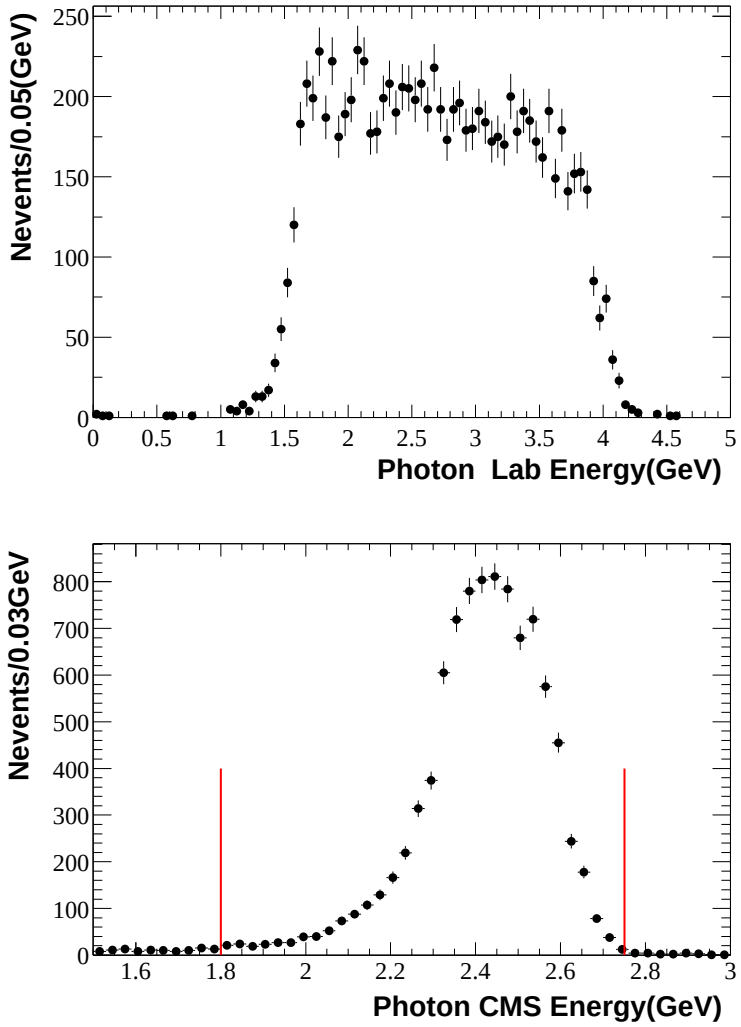

Figure 4: The energy distributions for reconstructed (truth-matched) photon candidates from $B^0 \to K_2^*(1430)^0\gamma$ ($K_2^{*0}(1430) \to K^+\pi^-$) in the lab and center-of-mass frame.

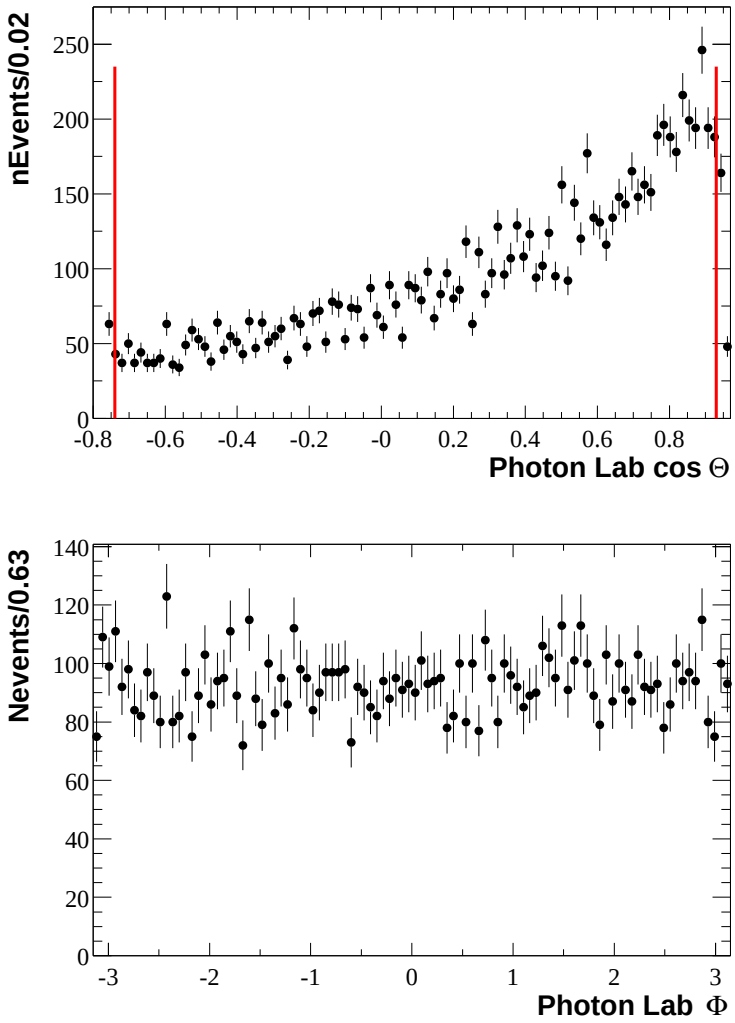

Figure 5: $\cos\theta$ and ϕ distributions for truth-matched reconstructed photon candidates from $B^0 \to K_2^*(1430)^0\gamma$ ($K_2^{*0}(1430) \to K^+\pi^-$) in the lab frame.

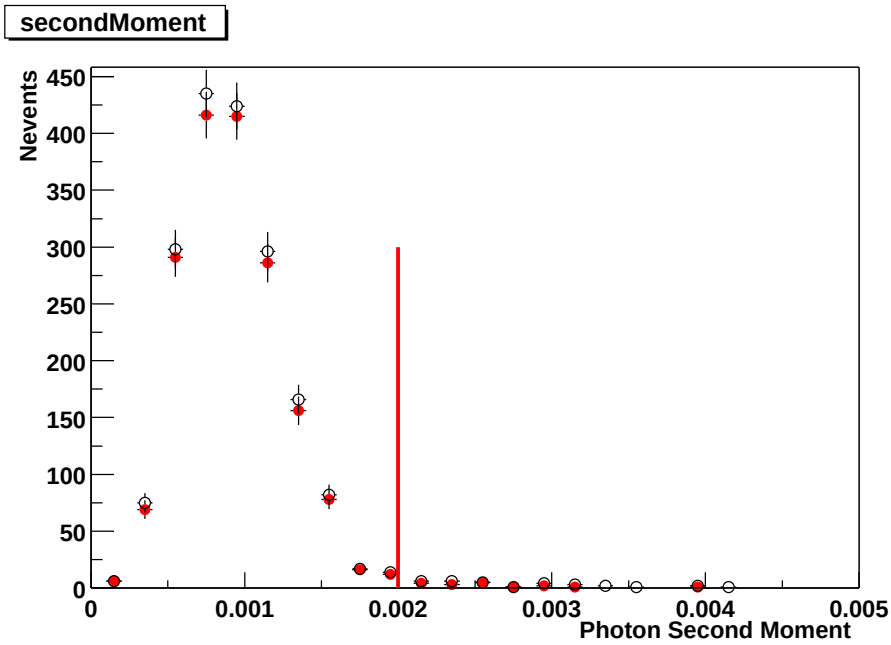

Figure 6: The second moment for photon clusters from the $B^0 \to K_2^*(1430)^0\gamma$ ($K_2^{*0}(1430) \to K^+\pi^-$) Monte Carlo (Open circles for the reconstructed, filled circles for the truth-matched).

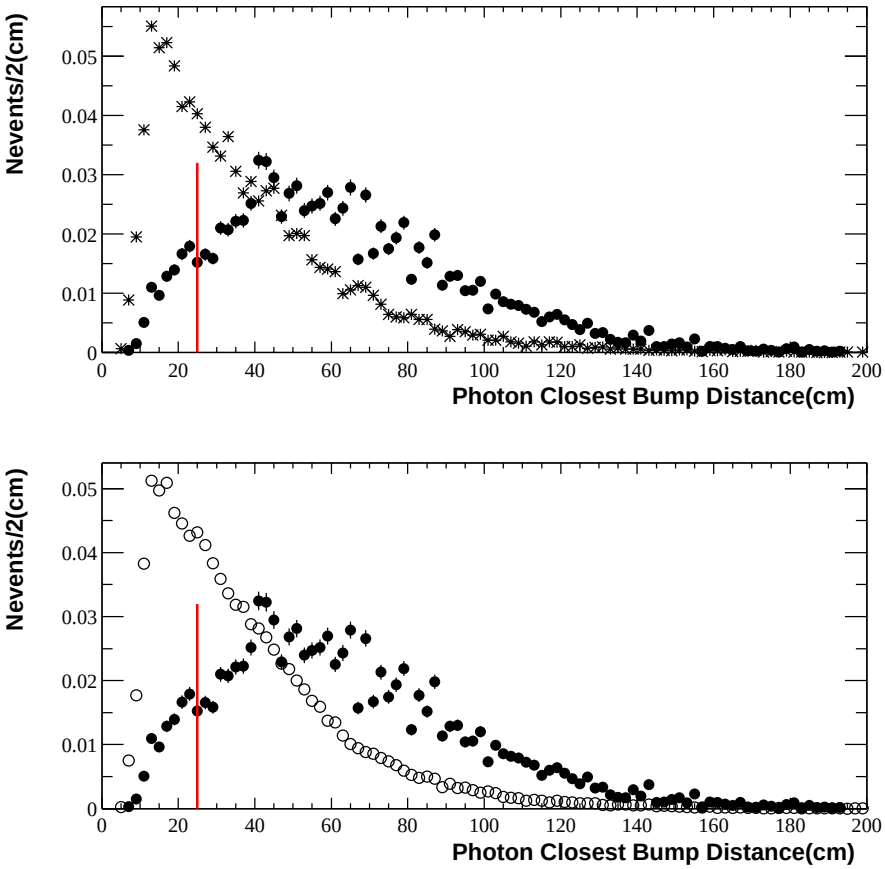

Figure 7: The separation from the closest cluster bump distribution:

●—- $B^0 \to K_2^*(1430)^0\gamma$ ($K_2^{*0}(1430) \to K^+\pi^-$) signal Monte Carlo

∗—- $uds{+}c\overline{c}$ background Monte Carlo

○—- Off-resonance data

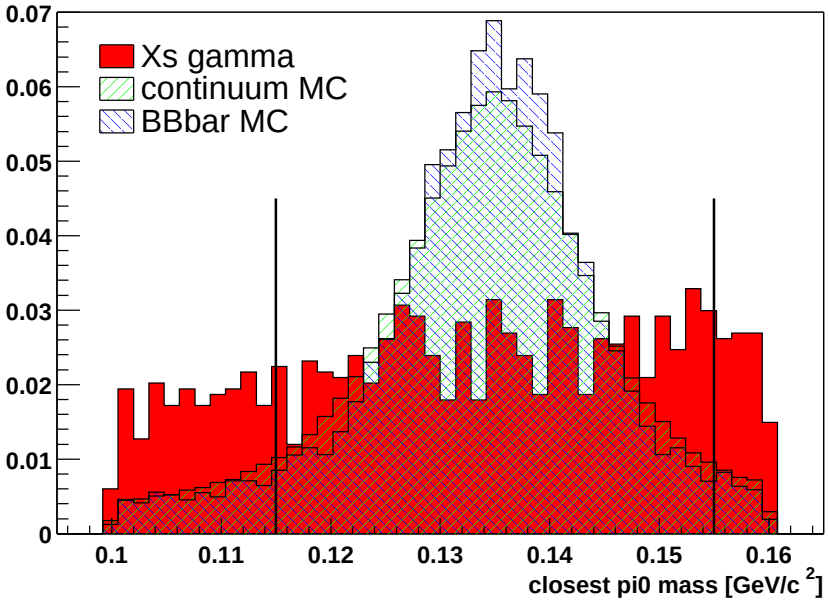

Figure 8: Closest π^0 mass formed by the high-energy γ candidate with another γ with $E^*_\gamma > 50\,\mathrm{MeV}$ (The red line is from the signal MC, the blue is from the $B\overline{B}$ background MC and the green is from the continuum background MC).

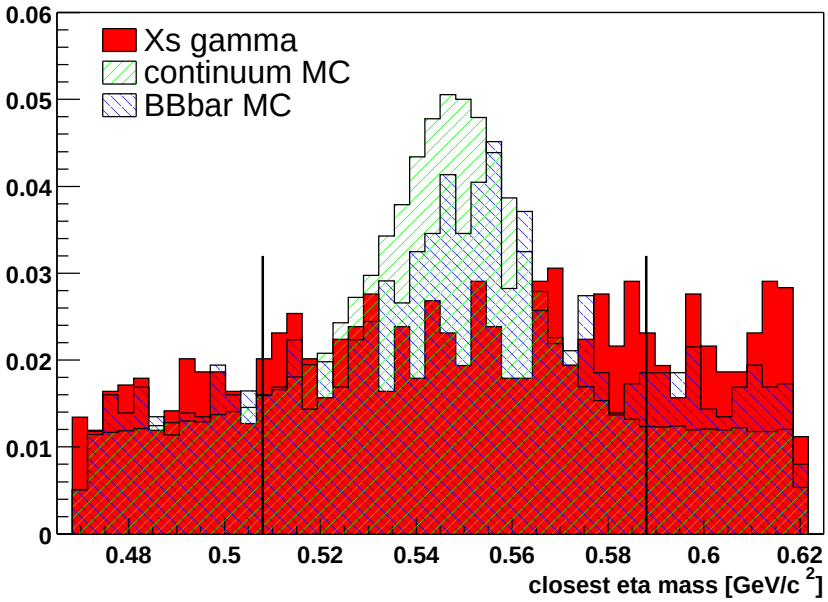

Figure 9: η mass window.

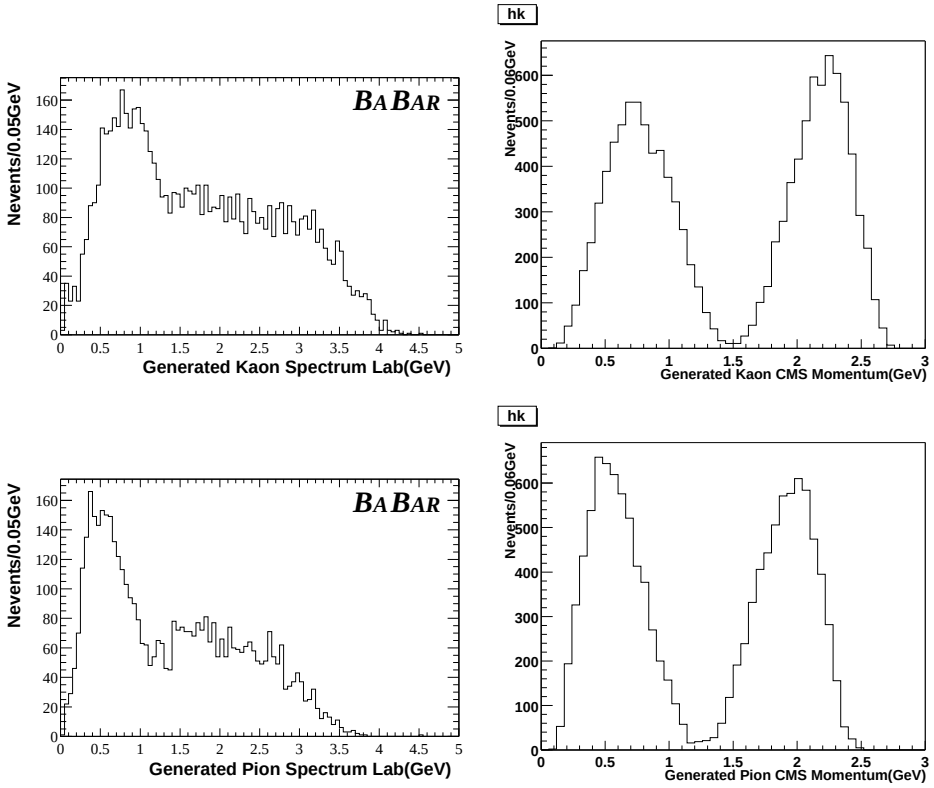

Figure 10: Generated momentum distribution of K^+ and π^- in lab frame and center-of-mass frame from $B^0 \to K_2^*(1430)^0\gamma$ ($K_2^{*0}(1430) \to K^+\pi^-$) Monte Carlo .

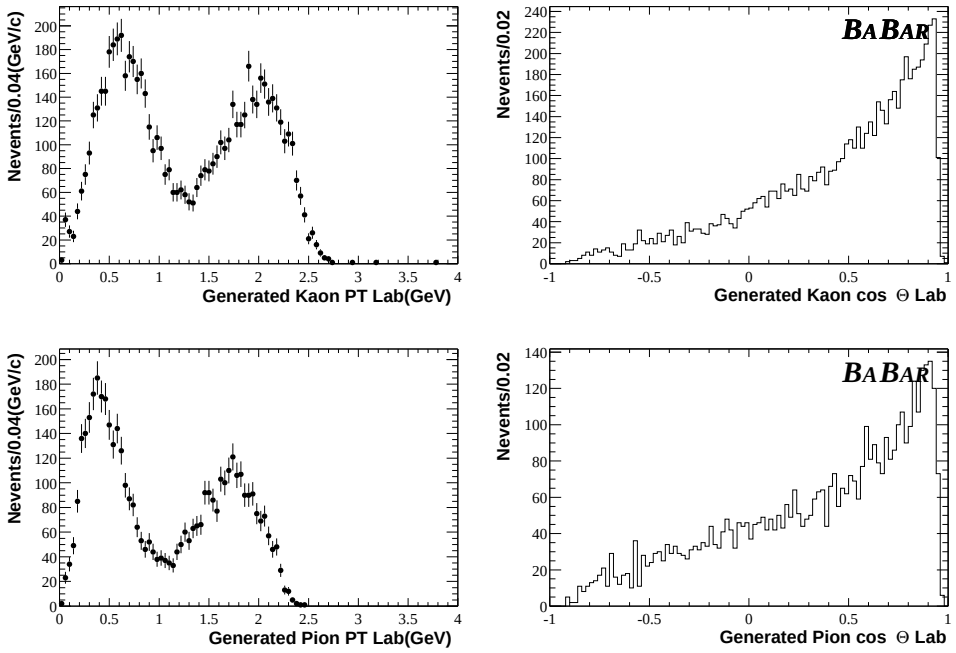

Figure 11: Transverse momentum and $\cos\theta$ distribution of truth-matched reconstructed K^+ and π^- from $B^0 \to K_2^*(1430)^0\gamma$ ($K_2^{*0}(1430) \to K^+\pi^-$) Monte Carlo .

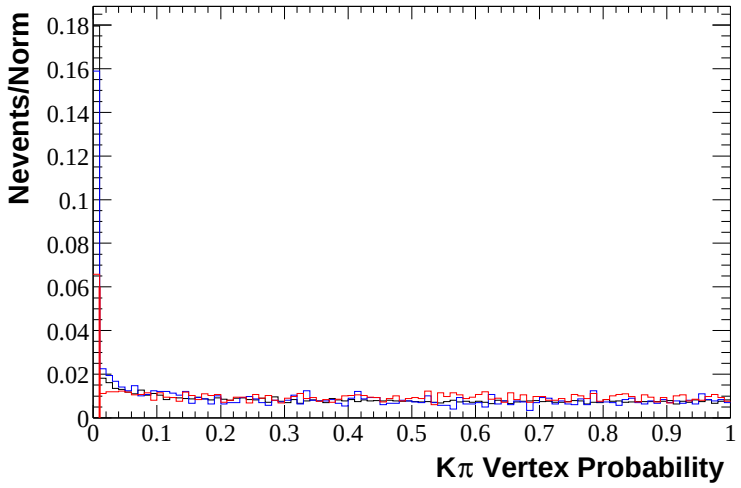

Figure 12: $K^+\pi^-\chi^2$ distribution from $B^0 \rightarrow K_2^*(1430)^0\gamma(K_2^{*0}(1430) \rightarrow K^+\pi^-)$ Monte Carlo (red) , continuum background Monte Carlo (black) and $B\overline{B}$ background (blue).

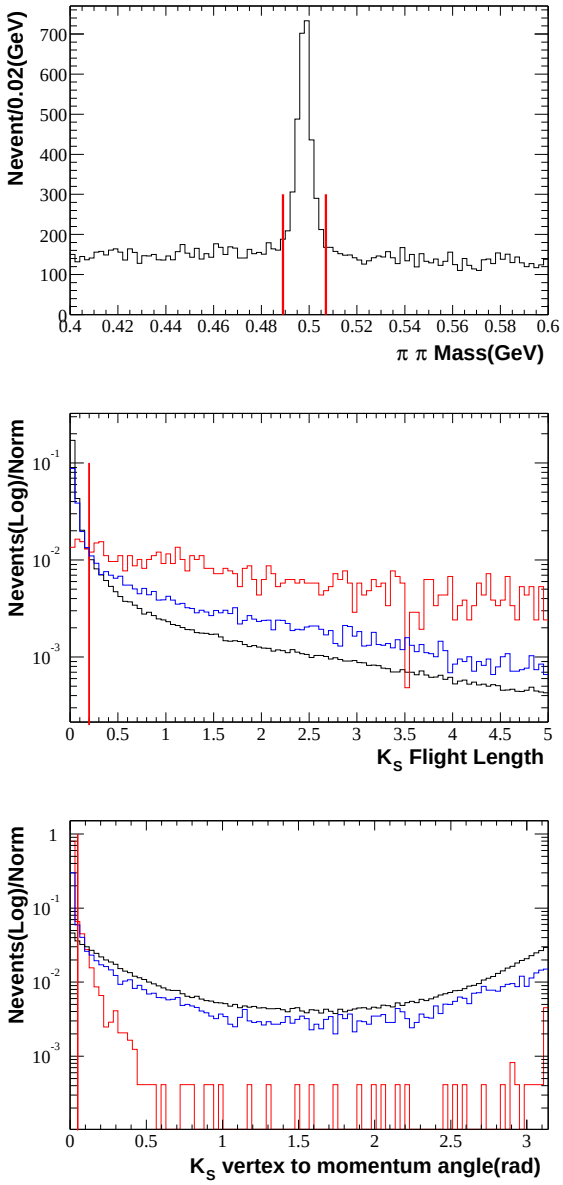

Figure 13: K_S mass, flight length and vertex position to momentum direction angle distribution (red for signal MC, black for continuum background and blue for $B\overline{B}$ background in the lower 2 plots).

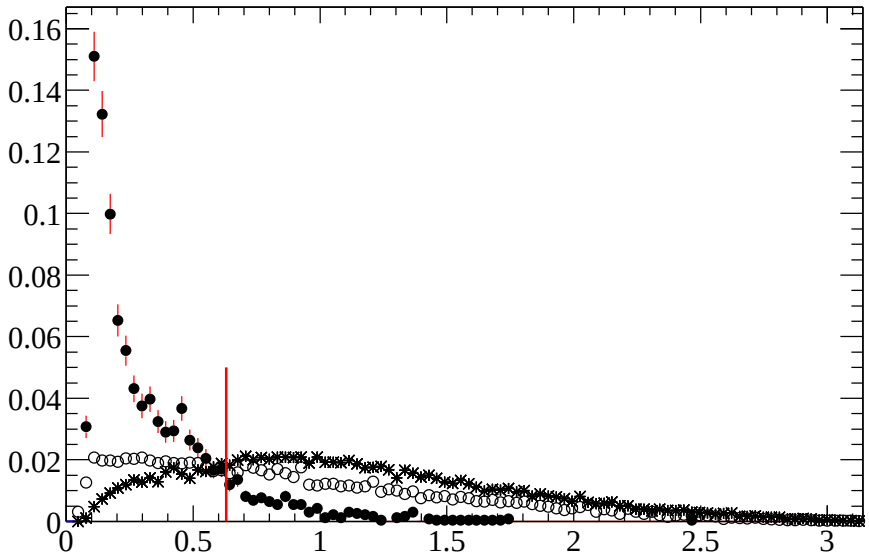

Figure 14: $\gamma\gamma$ open angle distribution comparison between truth-matched π^0s (black dot with red line) and fake π^0s (open-circled) in $B^+ \rightarrow K_2^*(1430)^+\gamma(K_2^{*+}(1430) \rightarrow K^+\pi^0$) MC sample and in continuum MC (close-circled).

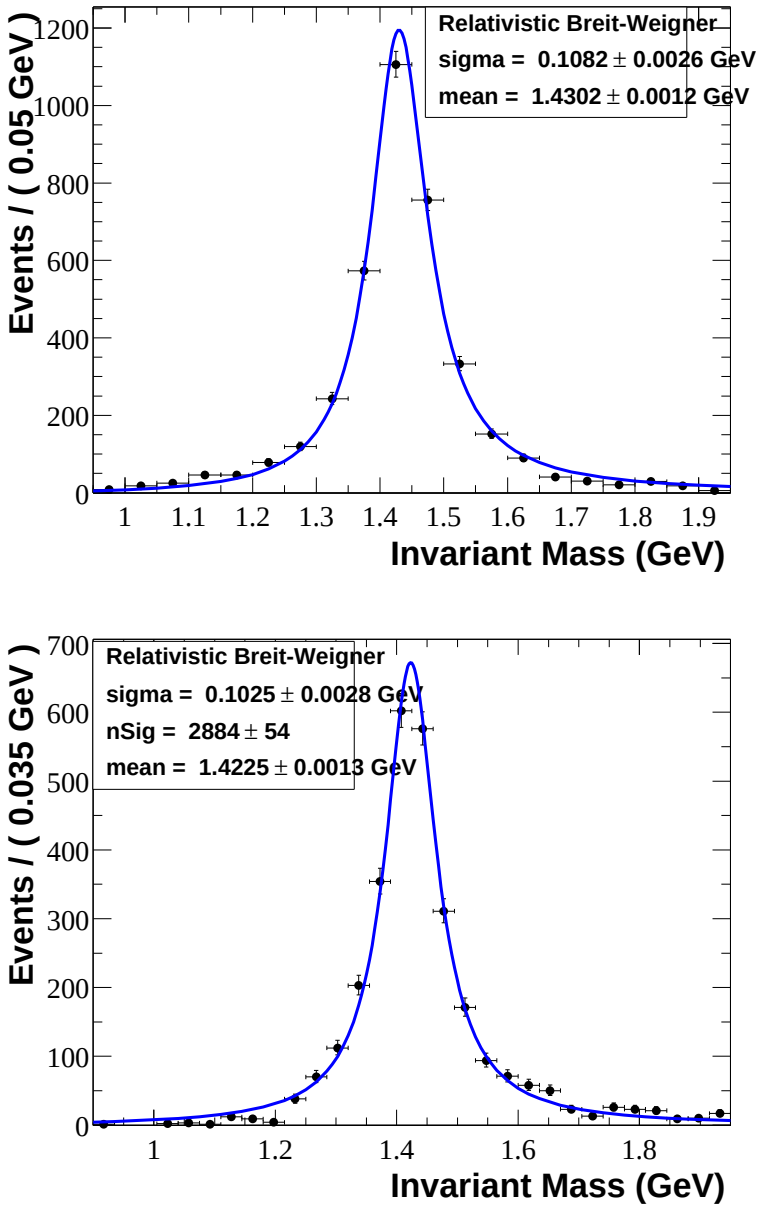

Figure 15: Invariant mass distributions from $B^0 \to K_2^*(1430)^0\gamma$ (top plot) and $B^+ \to K_2^*(1430)^+\gamma$ (bottom plot) Monte Carlo samples.

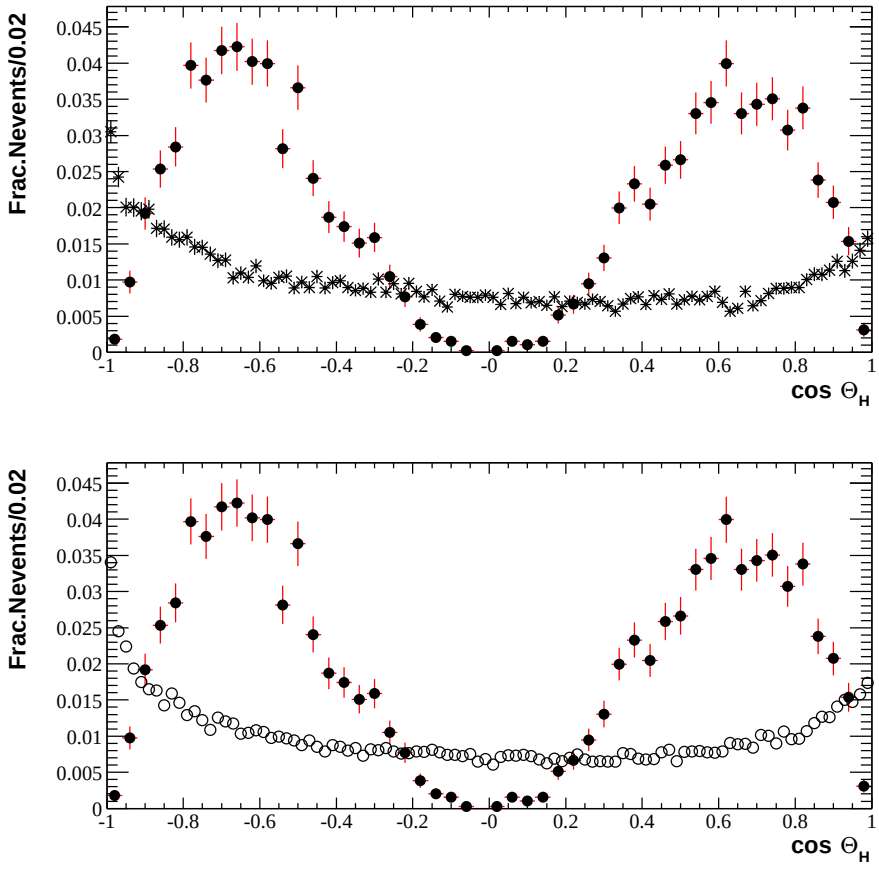

Figure 16: Helicity angle distribution :

• —- $B \to K_2^*(1430)\gamma$ signal Monte Carlo

$*$ —- off-resonance data (upper plot)

$\circ$ —- $uds{+}c\bar{c}$ background Monte Carlo (lower plot)

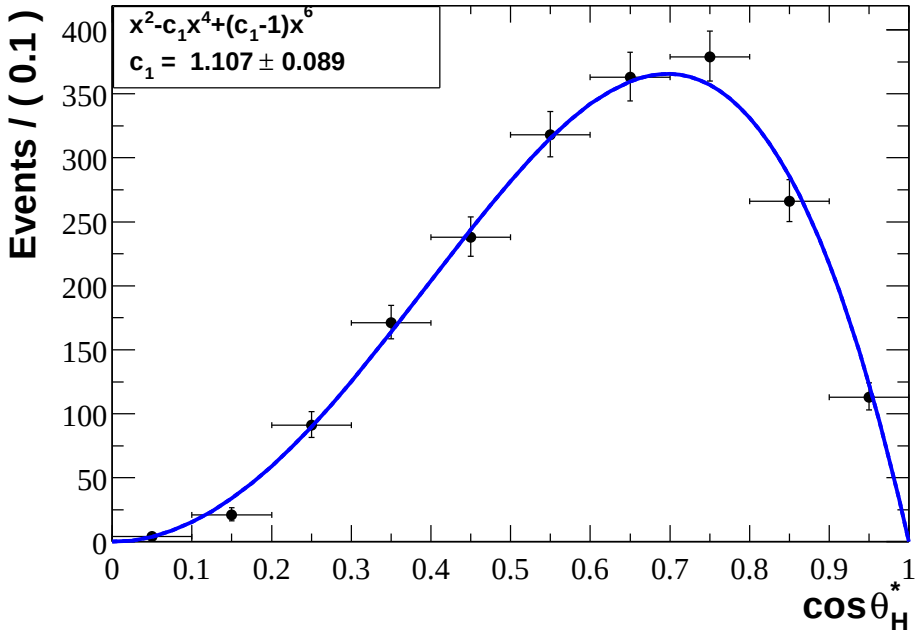

Figure 17: $|\cos\theta_H|$ distribution from the truth-matched signal $B^0 \to K_2^*(1430)^0\gamma$ ($K_2^{*0}(1430) \to K^+\pi^-$) Monte Carlo sample.

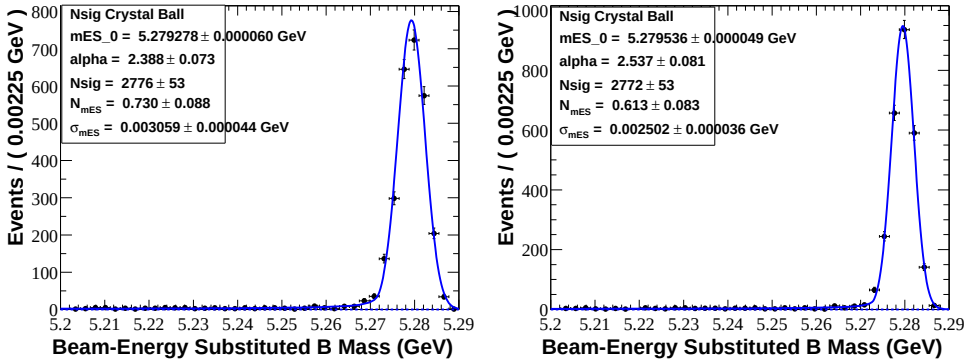

Figure 18: $m_{\rm ES}$ for reconstructed $B^0 \to K_2^*(1430)^0\gamma$ MC before and after rescaling the gamma energy.

4 Continuum Background Suppression

We exploit the difference in the event topology between signal and continuum background to reduce the continuum contribution.

4.1 Thrust Angle

For each B candidate we calculate the thrust angle $|\cos\theta_{\rm T}|$, defined as the angle between the direction of the photon candidate and the thrust axis of the rest of the event in the center-of-mass frame. The rest of the event includes all the particles not used in the reconstruction of the B candidate. The signal distribution is flat in $\cos\theta_{\rm T}$ since the thrust axes of the two B decays are uncorrelated. For the continuum background, the distribution peaks toward $|\cos\theta_{\rm T}|= 1$ due to its jet like structure. Fig. 19 shows the $|\cos\theta_{\rm T}|$ distribution from signal and continuum background MC, the distribution from off-resonance data is also included for reference purposes.

4.2 Neural Network

A neural network is a software (or hardware) simulation of a biological brain. The purpose of a neural network is to learn to recognize patterns (in our cases, signal and background) in the data. The neural network is able to detect similarities in inputs, even though a particular input may never have been seen previously. This property allows for excellent interpolation capabilities, especially when the input data is noisy (not exact). Once the neural network has been trained on samples, it can make predictions by detecting similar patterns in data. The neural network may be used as a direct substitute

for autocorrelation, multi-variable regression, linear regression, trigonometric and other regression techniques.

We train a neural network [29] with a combination of the thrust angle, the angle of the B-meson candidate's direction with respect to the beam axis, the scalar sum of the center-of-mass momentum of the rest of the event (binned with 10° intervals ranging from parallel to anti parallel relative to the photon momentum), sphericity, and the ratio of second-to-zeroth order Fox-Wolfram moments in the photon recoil system, which suppresses initial state radiation (ISR) background.

The basic structure of a neural network is described in Fig. 20, which is an example of 4 input variables, 1 hidden layer with 3 nodes and one output node. At the bottom of the figure, each circle represents an input variable, which is combined with a few other variables to form the hidden nodes (the blue circles): the hidden node j will be formed by the following combination:

$$Y_j = \sum a_{ij} x_j \tag{12}$$

Each hidden node receives a different linear combination of the input variables and then is transformed by an "activation" function (in this case the tanh function) into the final output. The activation function determines how fast the output of the hidden layer varies as a function of the input, if the input range is small, a linear response is recovered; if it's large, a step response will be used. At each stage, there is a "bias" node (purple) which provides a constant output. The linear combination of the output from the hidden nodes $g(Y_i)$ is

$$Z = \sum b_j g(Y_j) \tag{13}$$

The input variables used to train our neural network and then to produce the output are described in Fig. 21, 22 and 23. The details about those variables are explained below:

Thrust angle The angle between the photon candidate and the thrust of the event calculated excluding the B daughters in the CMS frame.

B **angle** The angle of the reconstructed B candidate with respect to the beam direction computed in the CMS frame.

coneN, N=1,2,...18 The momentum vectors in the center-of-mass system for tracks and photons not associated with the B candidate (binned in 10° intervals ranging from parallel to anti-parallel relative to the photon momentum).

Sphericity The angle of the B candidate sphericity axis with respect to the beam axis in the CMS frame.

R_2' The ratio of second-to-zeroth order Fox-Wolfram moment in the photon recoil system.

4.3 Neural Network Training

The parameters a_{ij} and b_j are optimized by a process known as "back-propagation". The performance of the neural network for any given set of coefficients is summarized by the sum-squared error (SSE):

$$\mathrm{SSE}(a_{ij}, b_j) = \sum_{a=1}^{N} [\mathrm{NN}(\vec{x_a}; a_{ij}, b_j) - F(\vec{x_a})]^2 \qquad (14)$$

and the network performance is qualified by the Mean Squared Error (MSE) defined as :

$$MSE = \frac{SSE}{Numberof Events} \tag{15}$$

We divide the MC samples into two equal parts, one as training sample and another as test sample. The MSE is evaluated and compared between these two samples to make sure there is no over-training (the neural network can optimize itself based on some features from statistical fluctuation). The MSE from training and test samples are shown in Fig. 24, from which we choose the training cycle as 300. In our case we use 24 hidden nodes for the 22 input variables.

4.4 Thrust Angle and Neural Network Optimization

Because the thrust angle is an important component in the neural network, they are somehow related. We optimize the thrust angle cut by maximizing $S^2/(S+B)$, here S represents the truth-matched signal Monte Carlo events and B represents continuum background events, and then apply the optimized value as a precut to train the neural network, which proves to help the trained neural network to have better performance. Then we train the neural network again and optimize the cut, and re-optimize the thrust angle with the neural network cut applied, then repeat the neural network training and optimizing..., the iteration will go on until there is no improvement to achieve on the $S^2/(S+B)$ any more.

The process of iteration is reported in Table 12, in which the second $\cos\theta_{\rm T}$ cut column is the optimized $\cos\theta_{\rm T}$ with neural network cut and will serve as the precut for the next round of neural network training if different

Table 12: Optimization of $\cos\theta_{\rm T}$ and neural network

Round	$\cos\theta_{\rm T}$ precut for NN training	Optimized cut from NN	Optimized $\cos\theta_{\rm T}$ cut	$S^2/(S+B)$
1	-	-	0.75	56.1
2	0.75	0.50	0.80	61.0
3	0.80	0.45	0.85	63.5
4	0.85	0.5	0.90	65.7
5	0.90	0.55	0.95	67.7
6	0.95	0.5	0.95	68.1

from the first value.

The neural network improves background suppression significantly. Fig. 25 shows the neural network output distribution from signal, continuum background MC and off-resonance data.

Because the variables used for the neural network training are mostly calculated from the rest-of-the-event (excluding the B daughters) information, we can use a sample of fully reconstructed $B \to D\pi^-$ as well as a sample of simulated $B \to D\pi^-$ as control samples. The bachelor pion in the $B \to D\pi^-$ decay is treated like the photon in $B \to K_2^*(1430)\gamma$ decay for the calculations of the event variables. Fig. 26 shows the distribution of the neural network output of $B^0 \to K_2^*(1430)^0\gamma$ signal, $B^0 \to D^+\pi^-$ and $B\overline{B}$ background MC samples.

The $B^0 \to K_2^*(1430)^0\gamma$ and $B^0 \to D^+\pi^-$ MC samples agree very well as shown by the optimized cut marked in the figure. The charged channel has very similar distributions.

In addition we compared the neural network output distributions between the $B \to D\pi^-$ MC sample and data control sample. Fig. 27 shows the neutral (left plot) and charged (right plot) modes.

Figure 28 shows the distribution of the neural network output of the backgrounds (continuum background MC, off-resonance data and on-resonance data sideband).

From the plots we see there is very good agreement between data samples, but a slight difference between data sample and MC sample. The difference in the efficiency of the cut on the neural network output between different samples is taken as the systematic uncertainty related to this cut.

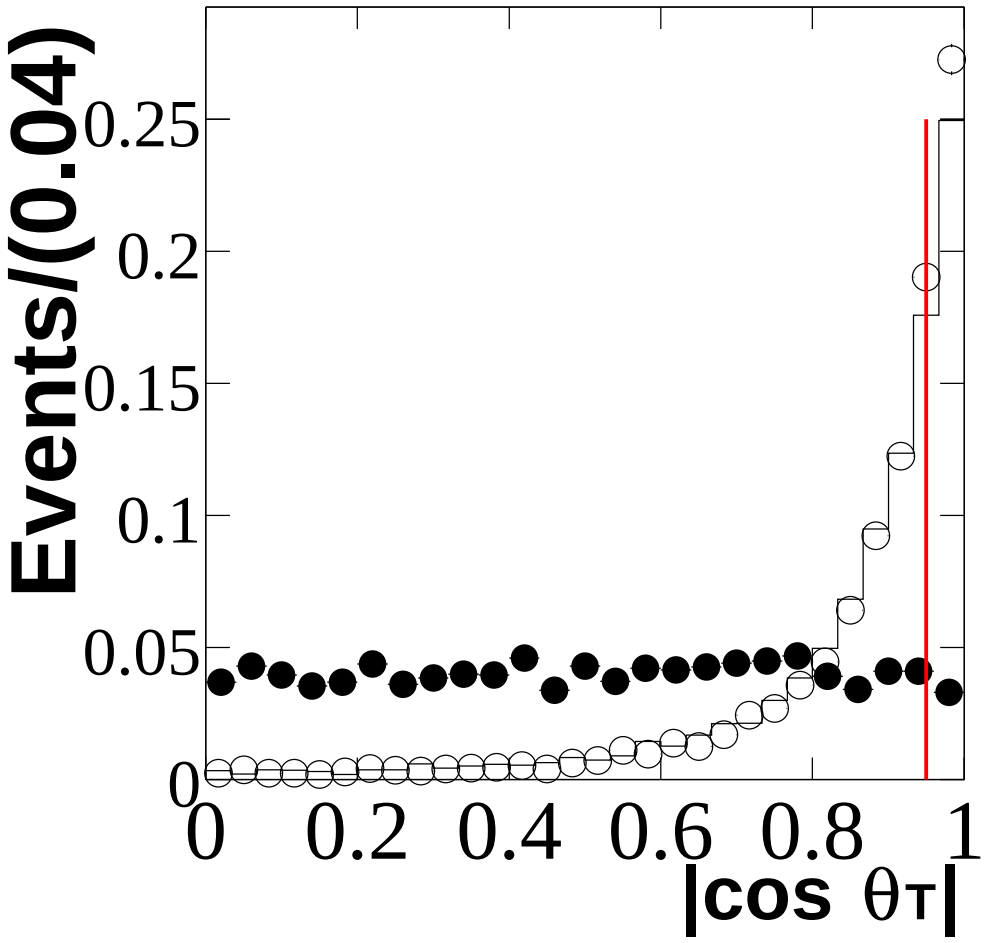

Figure 19: Thrust angle distribution of $B \to K_2^*(1430)\gamma$ MC simulation (filled circles), the off-resonance data (line), and the continuum background MC (open circles). The vertical line indicates the cut value.

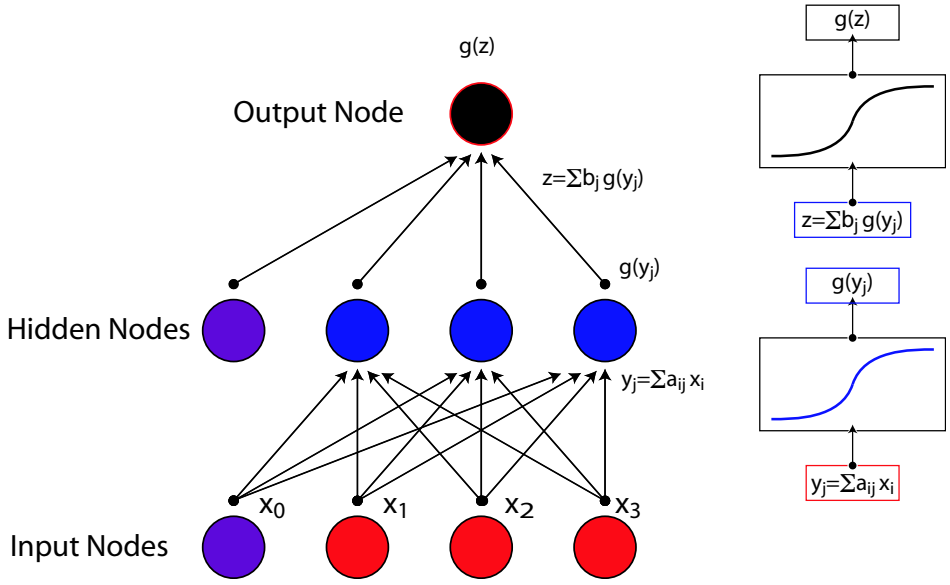

Figure 20: Basic structure of a single hidden layer neural network. Input nodes (red) corresponding to event variables are passed to "hidden" nodes (blue) as linear combinations. The line combination is then transformed by an "activation function," in this case the $\tanh(x)$. Linear combinations of the hidden node outputs are then passed to the output node (black), where it is transformed once again by the activation function to give the final neural network output.

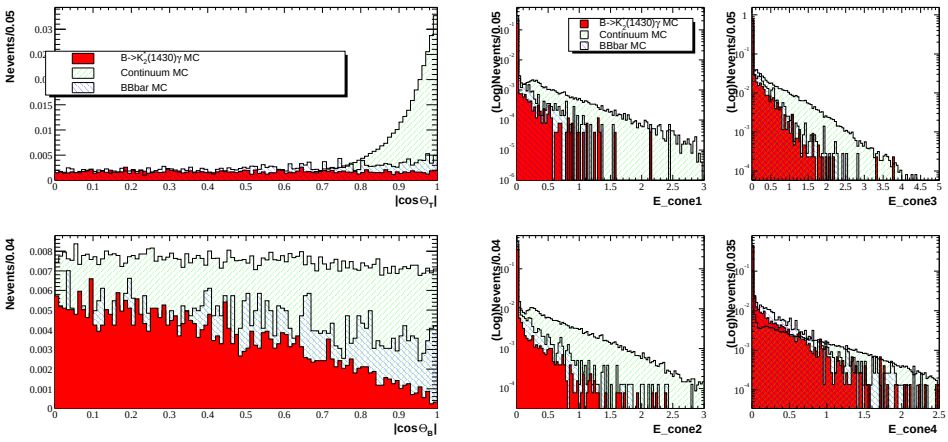

Figure 21: Variables used for neural network training: Thrust angle, B angle, Energy flows in cone 1-4.

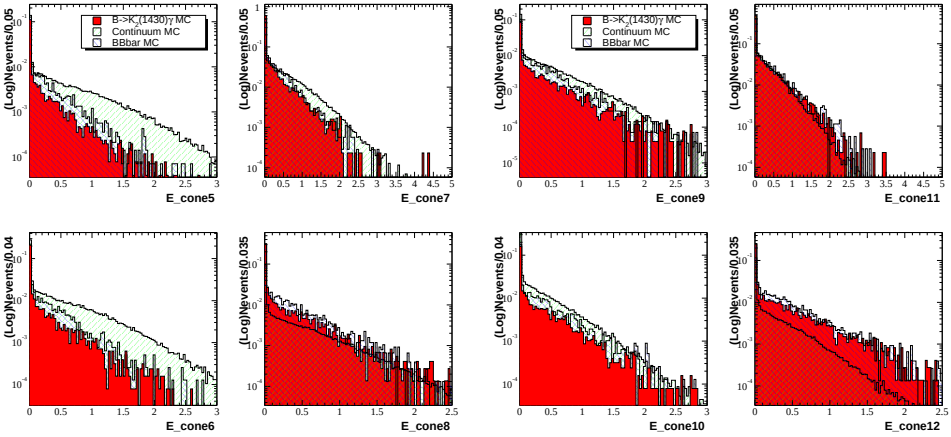

Figure 22: Variables used for neural network training: Energy flows in cone 5-12.

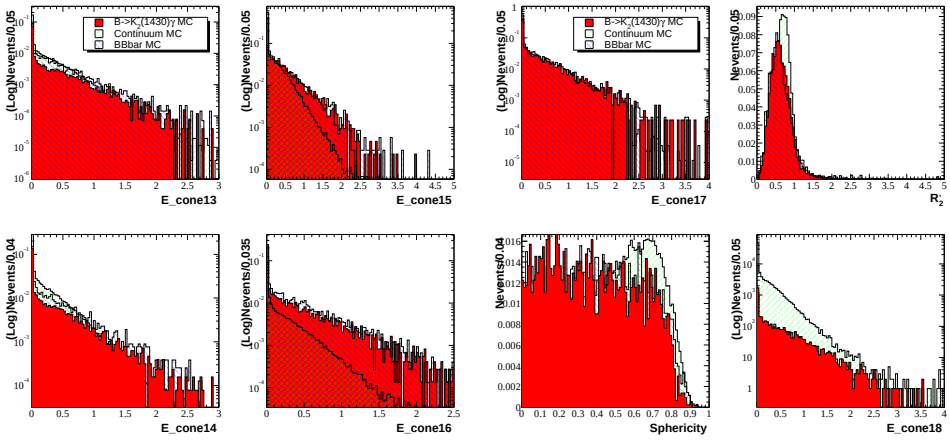

Figure 23: Variables used for neural network training: Energy flows in cone 13-18, Sphericity and R_2'.

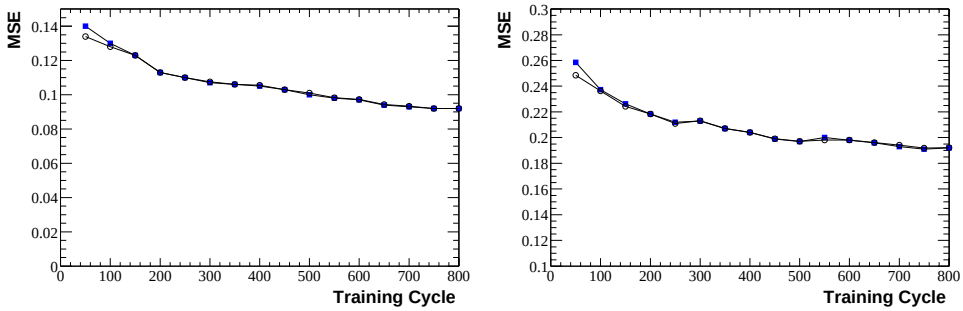

Figure 24: MSE according to different training cycles (squares for training sample, and circles for test sample). Left: Training for $B^0 \to K_2^*(1430)^0\gamma$ neural network. Right: Training for $B^+ \to K_2^*(1430)^+\gamma$ neural network.

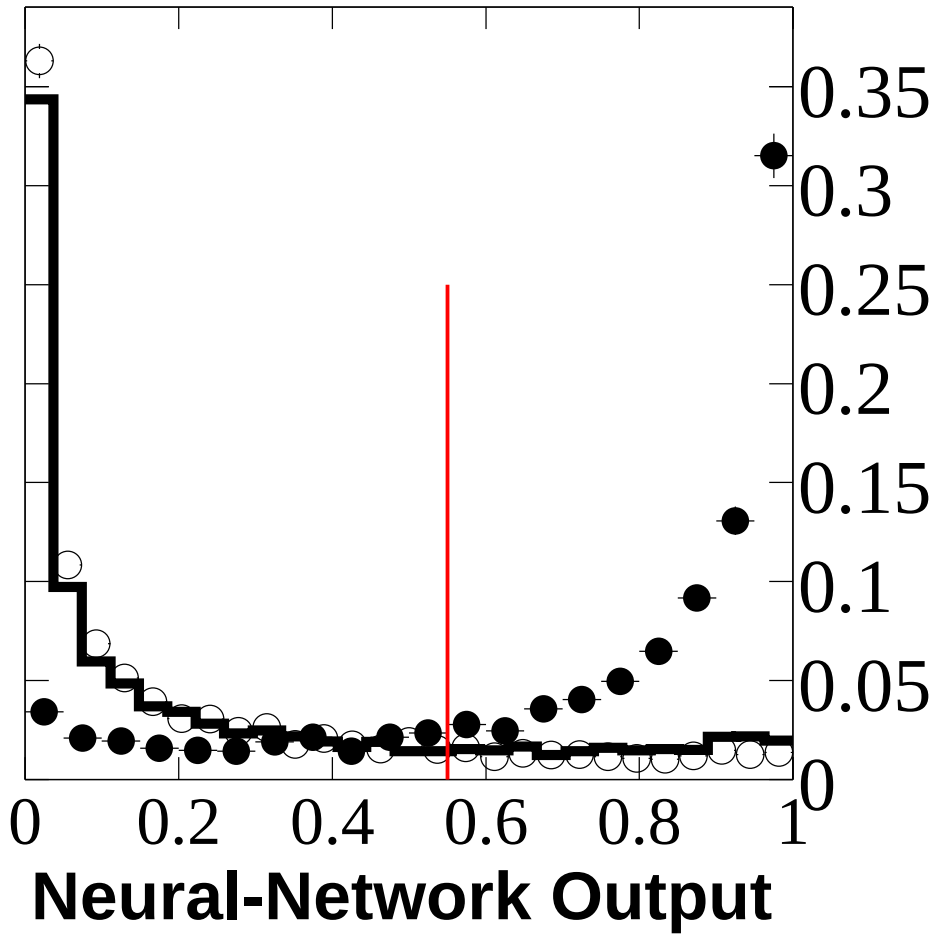

Figure 25: Neural network output distribution of $B \to K_2^*(1430)\gamma$ MC simulation (filled circles), the off-resonance data (line), and the continuum background MC (open circles). The vertical line indicates the cut value.

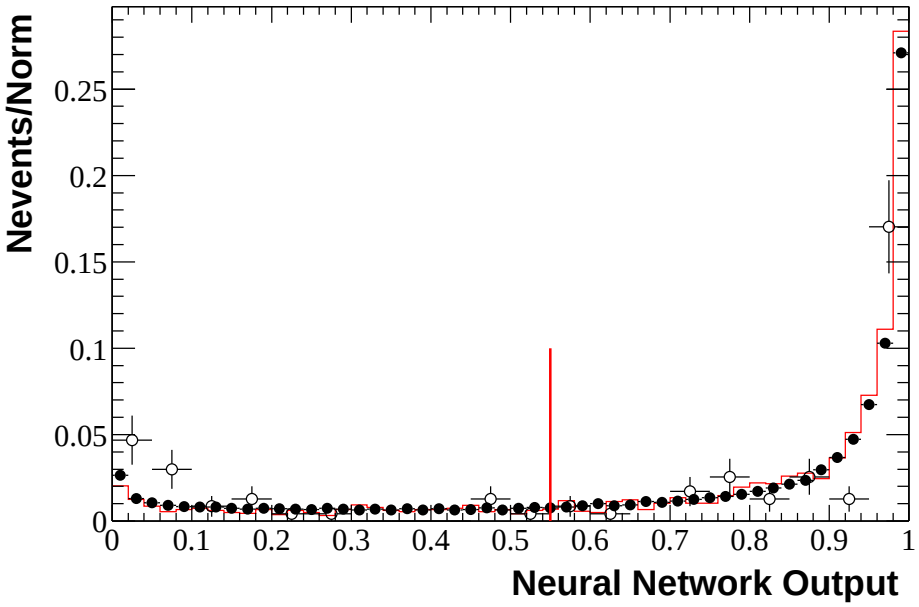

Figure 26: Neural network output distribution of signal $B^0 \to K_2^*(1430)^0\gamma$ (black line), $B^0 \to D^+\pi^-$ MC (close-circled dots) and $B\overline{B}$ background MC (open-circled dots). The vertical line indicates the cut position.

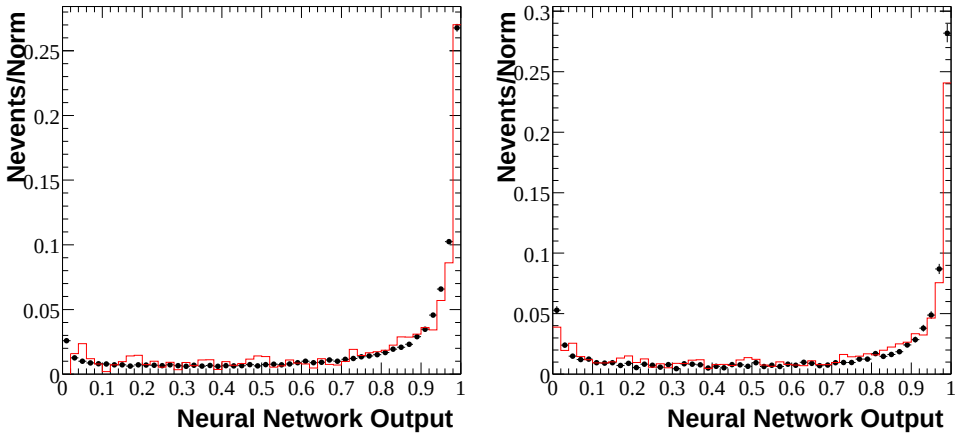

Figure 27: Neural network output distribution of $B^0 \to D^+\pi^-$ (left plot) and $B^+ \to D^0\pi^-$ (right plot) MC sample (dots) and data control sample (red line).

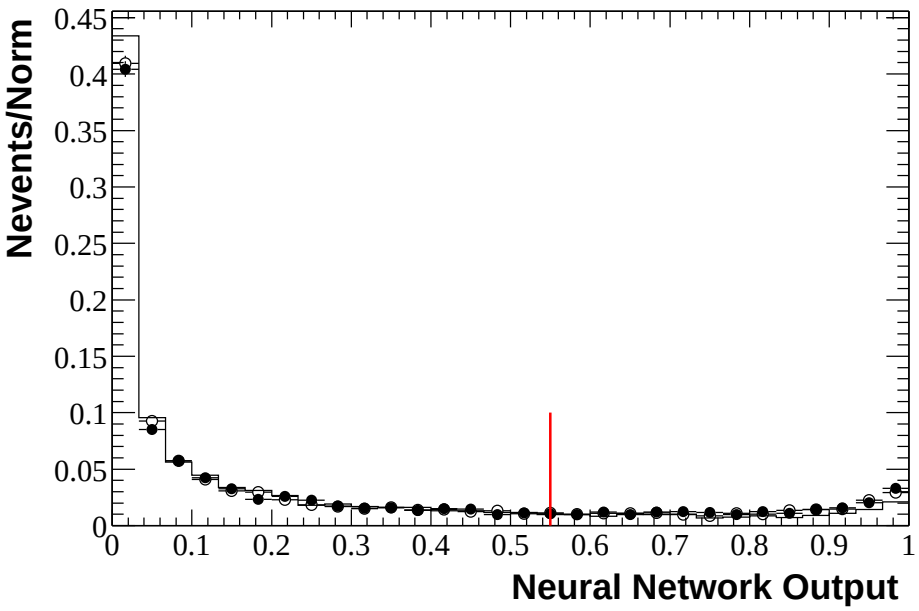

Figure 28: Neural network output distribution of continuum background MC, off-resonance data (filled circle) and on-resonance data sideband (open circle). The vertical line indicates the cut position.

5 Efficiency Study

5.1 Multiple Candidates

In some events there are more than one B candidates reconstructed. From the signal MC, we studied the percentage of events with multiple B candidates in the fit region ($5.2\,\mathrm{GeV} < m_{\mathrm{ES}} < 5.3\,\mathrm{GeV}, -0.3\,\mathrm{GeV} < \Delta E < 0.3\,\mathrm{GeV}$), which is 3.1% for the $K^+\pi^-$ decay channel, 6.3% for the $K_S\pi^+$ decay channel and 4.9% for the $K^+\pi^0$ decay channel, after applying all the cuts. We have to get rid of the excess B candidates to guarantee there is only one B candidate, thus simplifying the statistics. The strategy we use here is to look at each event, and if there are multiple B candidates, we will select the candidate whose $K\pi$ hadronic mass is the closest to the $K_2^*(1430)$ PDG value, which picks up 70.4%, 66.7% and 70.5% of the correct B candidates for the 3 different channels in the multi-B events. This procedure introduces a correction on the efficiency, which is shown in Table 13. A complete list of the efficiencies according to the cuts is shown in Table 13, in which the "un-truth-matched" efficiency is after the multi-B selection process and will be used for branching fraction calculation.

Table 13: Efficiencies listing

Cut	$B^0 \to K_2^{*0}\gamma$ $(K_2^{*0} \to K^+\pi^-)$	$B^+ \to K_2^{*+}\gamma$ $(K_2^{*+} \to K_S\pi^+)$	$B^+ \to K_2^{*+}\gamma$ $(K_2^{*+} \to K^+\pi^0)$
Global Variables	78.1	76.4	74.6
Photon Selections	72.3	73.0	71.2
(K, π, K_S, π^0) selection	54.6	43.5	36.0
$\lvert m_{Had} - m_0 \rvert < 1.1\sigma$	82.9	81.3	80.3
$\lvert cos\theta_T \rvert < 0.95$	95.5	95.5	95.4
NN > 0.50	76.9	79.8	79.8
$\lvert \Delta E \rvert < 0.3\,\mathrm{GeV}$ $m_{\mathrm{ES}} > 5.2\,\mathrm{GeV}$	98.1	98.8	98.0
Truth-matched efficiency	18.3	16.3	10.3
Un-truth-matched efficiency	19.2	16.9	11.3

6 Maximum Likelihood Analysis

The signal yields are extracted using a simultaneous maximum-likelihood (ML) fit of the $m_{\rm ES}$, ΔE and $\cos\theta_H$ distributions. The fit is performed independently for each of the decay modes considered here. All fitting is performed using the RooFitCore and RooFitModels [30] fit engine. The details about the fit will be introduced section by section.

6.1 Probability Density Function(PDF) Used for the Fit on Signal

We use the "Crystal-Ball" distribution for the signal $m_{\rm ES}$ and ΔE. The "Crystal-Ball" function is described as below:

$$S \propto \begin{cases} \exp(-(m-m_0)^2/(2\sigma^2)) & \text{if } m > m_0 - \alpha\sigma \\ \frac{(n/\alpha)^n exp(-\alpha^2/2)}{((m_0-m)/\sigma+n/\alpha-\alpha)^n} & \text{if } m \leqslant m_0 - \alpha\sigma \end{cases} \tag{16}$$

The signal $\cos\theta_H$ distribution is described by a customized function, in which the parameter ccc1 describes the possible shift from the theoretical tensor $\cos\theta_H$ distribution function $\sin^2\theta_H\cos^2\theta_H$.

$$S \propto \sin\theta_H{}^2\cos\theta_H{}^2 - (ccc1 - 1.0) \times (\cos\theta_H{}^4 - \cos\theta_H{}^6) \tag{17}$$

The total PDF is a product of the individual PDFs. The signal reference distributions for $B \to K_2^*(1430)\gamma$ are obtained from Monte Carlo sample after applying all selection cuts. Fig. 29, 30 and 31 shows the ML fit on signal MC samples.

The fitted parameters are listed in Table 14:

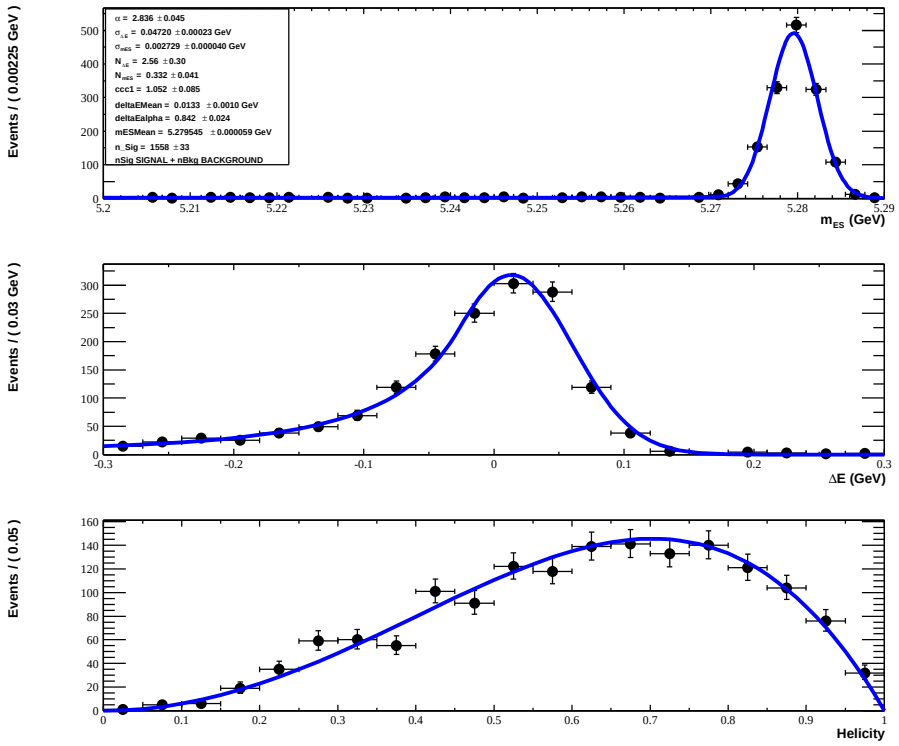

Figure 29: Maximum-likelihood fitting of $m_{\rm ES}$, ΔE and $\cos\theta_H$ variables using signal $B^0 \to K_2^*(1430)^0\gamma$ ($K_2^{*0}(1430) \to K^+\pi^-$) MC sample.

6.2 Background PDFs

We classify the background into two categories: the "peaking" and the "non-peaking" background.

6.2.1 "Non-peaking" Background

As for the "non-peaking" background, which comes from the combinatorial background from B decays and continuum $q\overline{q}$ production, where q can be a u,

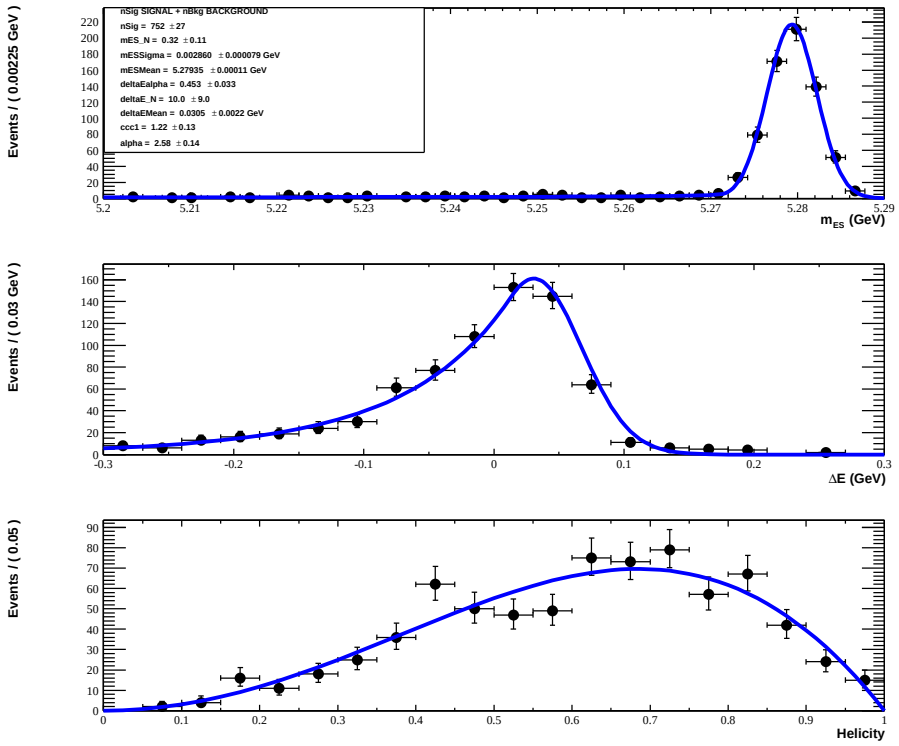

Figure 30: Maximum-likelihood fitting of $m_{\rm ES}$, ΔE and $\cos\theta_H$ variables using signal $B^+ \to K_2^*(1430)^+\gamma$ ($K_2^{*+}(1430) \to K^0\pi^+, K^0 \to K_S^0 \to \pi^+\pi^-$) MC sample.

d, s or c quark, we use the "ARGUS" function for the $m_{\rm ES}$ parameterization,

$$B \propto \frac{M_{ES}}{E_{beam}} \times \sqrt{1 - \frac{M_{ES}^2}{E_{beam}^2}} \times \exp(-\zeta(1 - \frac{{M_{ES}}^2}{E_{beam}^2})) \qquad (18)$$

a 1st-order polynomial shape for ΔE as below:

$$B \propto 1 + L_{\Delta E} \times \Delta E \qquad (19)$$

and an exponential shape for $\cos\theta_H$.

$$B \propto 1 + f \times \exp(\tau|\cos\theta_H\ |) \qquad (20)$$

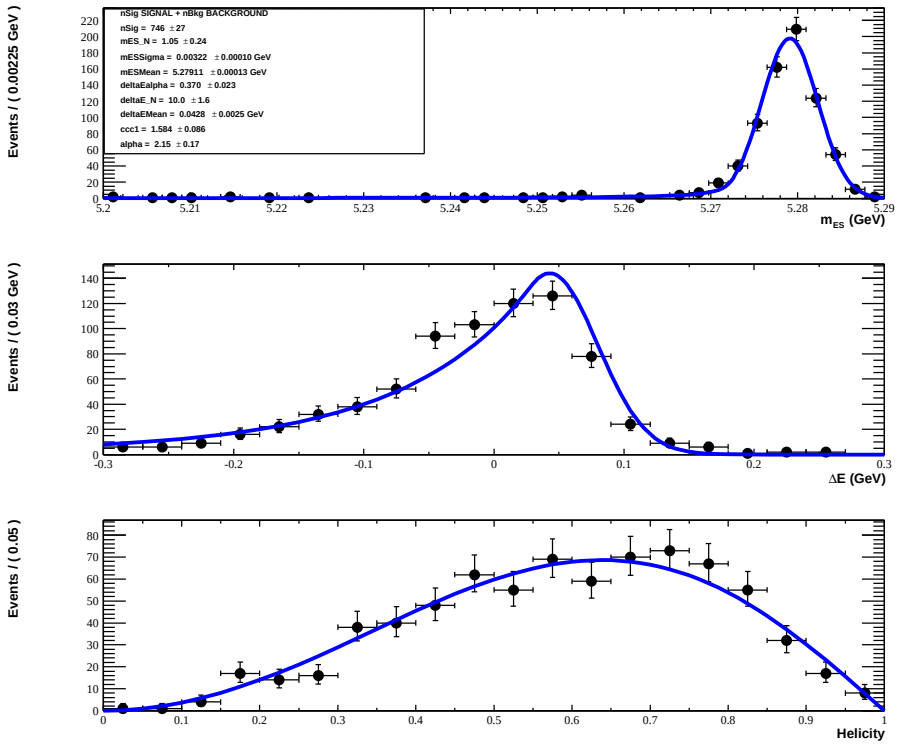

Figure 31: Maximum-likelihood fitting of $m_{\rm ES}$, ΔE and $\cos\theta_H$ variables using signal $B^+ \to K_2^*(1430)^+\gamma$ ($K_2^{*+}(1430) \to K^+\pi^0$) MC sample.

We first check whether or not the probability distribution factorizes. The results are shown in Fig. 32, 33 and 34. We used a slightly bigger fit range on ΔE ($\pm 0.4\,\mathrm{GeV}$ instead of $\pm 0.3\,\mathrm{GeV}$ to gain more statistics for the study).

From Figure 32 we find that both $m_{\rm ES}$ and $\cos\theta_H$ parameters agree within the errors in different regions. From Figure 33 we get a similar conclusion about the ΔE and $\cos\theta_H$ distributions in different $m_{\rm ES}$ sideband regions. We also checked $m_{\rm ES}$ and ΔE distributions in sidebands in a differ-

Table 14: The fitted parameters listing

Parameter	Mode $B \to K_2^*(1430)\gamma$		
	$K^{\pm}\pi^{\mp}$	$K_S^0\pi^{\pm}$	$K^{\pm}\pi^0$
Signal yield	1558.0 ± 39.5	869.0 ± 29.5	894.2 ± 30.6
$m_{\rm ES}$ σ (MeV)	2.73 ± 0.05	2.61 ± 0.07	3.01 ± 0.09
$m_{\rm ES}$ mean (MeV)	5279.55 ± 0.07	5279.36 ± 0.09	5279.10 ± 0.11
$m_{\rm ES}$ α	2.84 ± 0.10	1.84 ± 0.08	1.60 ± 0.07
$m_{\rm ES}$ N	0.33 ± 0.09	0.98 ± 0.10	1.40 ± 0.14
ΔE σ (MeV)	47.2 ± 0.32	47.6 ± 0.23	55.8 ± 0.27
ΔE mean (MeV)	13.3 ± 1.6	-5.0 ± 2.5	-20.5 ± 2.9
ΔE α	0.84 ± 0.08	0.60 ± 0.04	0.69 ± 0.05
ΔE N	2.55 ± 0.64	9.05 ± 1.40	3.6 ± 1.8
Helicity parameter	1.05 ± 0.10	1.30 ± 0.11	1.68 ± 0.07

ent $|\cos\theta_H|$ range, which is shown in Figure 34. From Figure 34 we can see that both ΔE and $m_{\rm ES}$ parameters agree within error in different regions.

In conclusion, the background distribution probability factorizes well using the PDFs we chose.

As for the $K^+\pi^0$ mode it has a different helicity distribution from the continuum background, which is described by a function.

$$B \propto [1 - (\frac{\cos\theta_H}{\cos\Theta_0})^2]^{\alpha} \times \exp(-\zeta[1 - (\frac{\cos\theta_H}{\cos\Theta_0})^2]) \qquad (21)$$

Figure 35 shows the helicity fit on on-resonance data $m_{\rm ES}$ sideband, and it shows that the function describes the helicity very well.

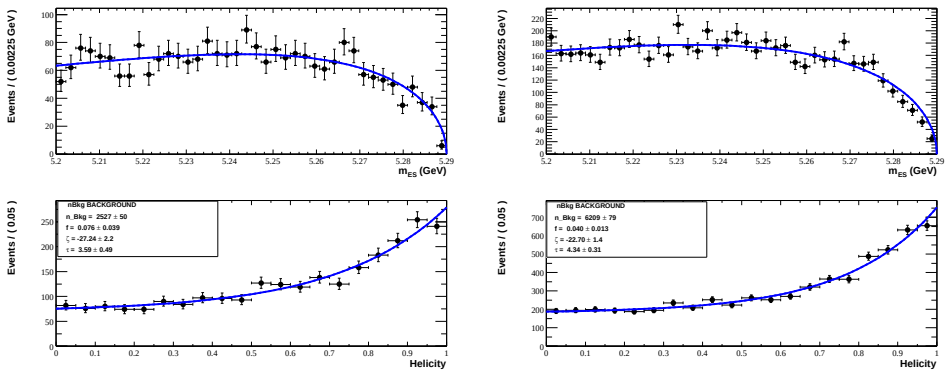

Figure 32: $m_{\rm ES}$ and $\mid \cos\theta_H \mid$ distributions in the high ($0.0 < \Delta E < 0.4$, left plot) and low ($-0.4 < \Delta E < 0.0$, right plot) ΔE sidebands.

Figure 36 shows the ML fit with the $59.6\,\mathrm{fb}^{-1}$ continuum MC sample and $81.4\,\mathrm{fb}^{-1}$ on-resonance data $m_{\rm ES}$ sideband, which serves a good sample for the continuum background and it shows these PDFs describe the background pretty well.

Figure 37 shows the ML fit with the $59.9\,\mathrm{fb}^{-1}$ $B\overline{B}$ MC sample, in which the $B \to X_s\gamma$ modes have been excluded due to the fact that we can not separate our signal from the other $B \to X_s\gamma$ components effectively.

6.2.2 "Peaking" Background

The second background contribution is from other resonant $B \to X_s\gamma$ modes, predominantly $B \to K^*(1410)\gamma$, and non-resonant $B \to K\pi\gamma$ decays. We label these the "peaking" background, since these decays have $m_{\rm ES}$ and ΔE distributions similar to the signal. In order to distinguish the $B \to K_2^*(1430)\gamma$ signal from the background decays, we examine the helicity angle distributions. In the $B \to K^*(1410)\gamma$ decay the $K\pi$ system

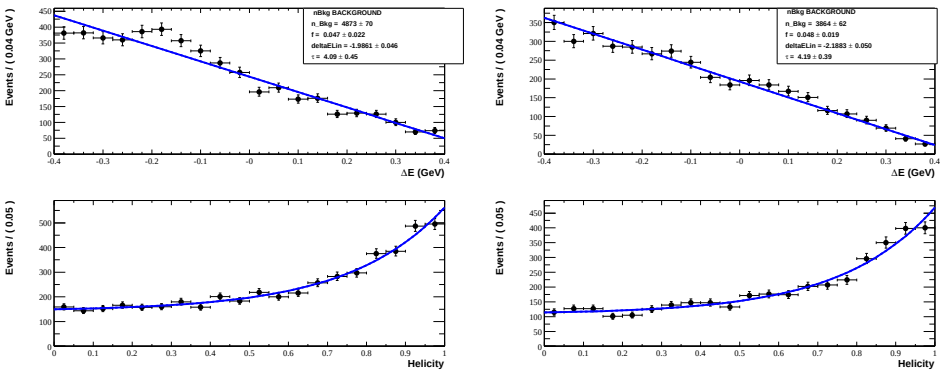

Figure 33: ΔE and $|\cos\theta_H|$ distributions in the low ($5.2 < m_{\rm ES} < 5.235$, left plots) and high ($5.235 < m_{\rm ES} < 5.27$, right plots) $m_{\rm ES}$ sidebands.

has a $\sin\theta_H{}^2$ helicity distribution and in the non-resonant decays the $K\pi$ system was dominated by the $J = 1$ state (the $J = 0$ state is forbidden due to helicity conservation), which has the same helicity distribution as the $B \to K^*(1410)\gamma$ decay.

The ML fits of $m_{\rm ES}$, ΔE and $\cos\theta_H$ from the $B \to K^*(1410)\gamma$ MC sample are shown in Fig. 38.

The parameters in Fig. 38 are listed in Table 15.

6.3 3-body Sub-decay Contributions

There are different fractions of "3-body" ($K^{**} \to K\pi\pi$, $K\rho(\rho \to \pi\pi)$, $K^*(892)\pi$ ($K^*(892) \to K\pi$) ...) decays from the high-kaon resonant modes, as mentioned in section 1. If, in the reconstruction process there is a slow pion missing, such 3-body decays will "fool" around as 2-body decays in the reconstruction process. To deal with such cases, studies have been carried

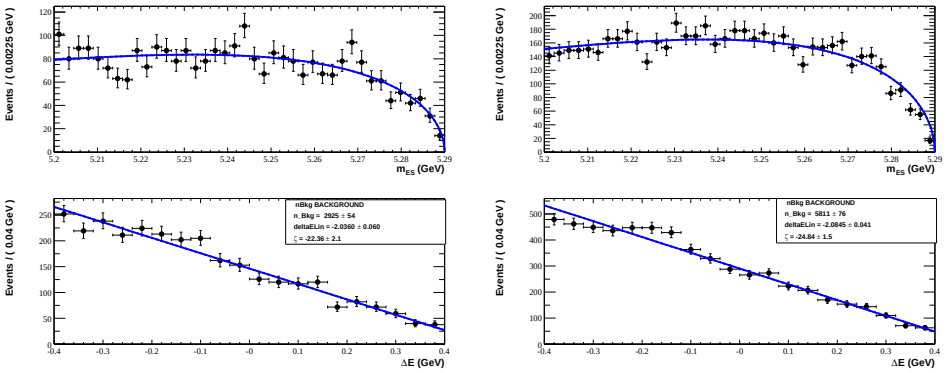

Figure 34: $m_{\rm ES}$ ΔE distributions in $|\cos\theta_H| > 0.5$ (left plots) and $|\cos\theta_H| < 0.5$ (right plots) ranges.

Table 15: The fit parameters from $B \to K^*(1410)\gamma$ MC sample

Parameter	Cross-feed MC	
	neutral sample	charged sample
$m_{\rm ES}$ σ (MeV)	2.61 ± 0.09	2.87 ± 0.16
$m_{\rm ES}$ mean (MeV)	5279.53 ± 0.12	5279.29 ± 0.20
$m_{\rm ES}$ α	1.72 ± 0.17	1.47 ± 0.23
$m_{\rm ES}$ N	8.2 ± 3.4	3.0 ± 1.1
ΔE σ (MeV)	38.2 ± 2.2	45.8 ± 5.2
ΔE mean (MeV)	-9.4 ± 3.1	-14.3 ± 4.5
ΔE α	0.78 ± 0.12	0.57 ± 0.07
ΔE N	4.5 ± 1.9	6.8 ± 2.5

out to check how these contributions affect the signal yield.

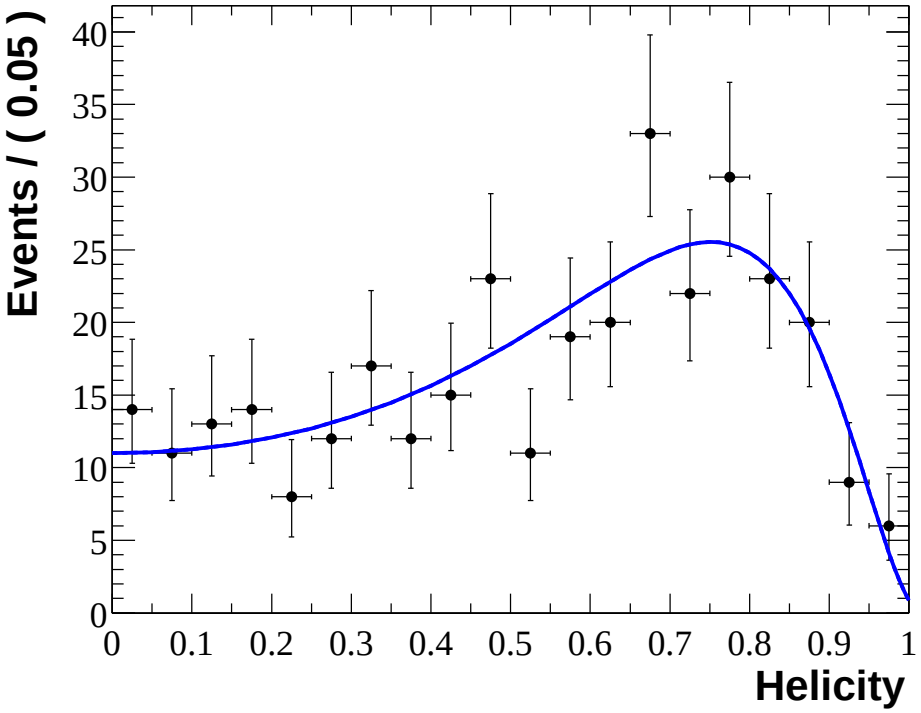

Figure 35: Maximum-likelihood fitting of $\cos\theta_H$ distribution with on-resonance data $m_{\rm ES}$ sideband for $K^+\pi^0$ mode.

6.3.1 3-body Sub-decays Crossing into $K^+\pi^-$ Mode

Figure 39 shows the $m_{\rm ES}$, ΔE and $\cos\theta_H$ distributions from the $B^+ \to K_2^*(1430)^+\gamma$ MC sample done with the $K^+\pi^-$ reconstruction and cuts.

From Fig. 39 we can see the yield is 5.4 ± 3.2 from 44000 MC events, which equals an adjustment of $+0.04 \pm 0.02\%$ on efficiency, based on the assumption that neutral and charged modes have the same branching fraction. This correction is small in comparison to the efficiency of 19.2%, therefore it is neglected.

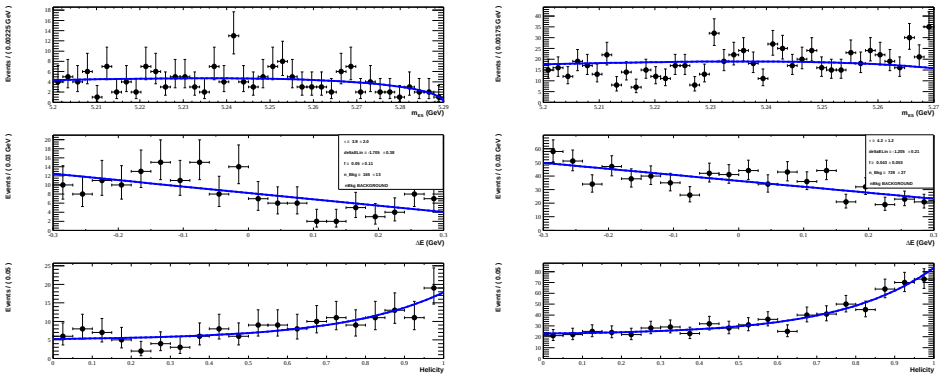

Figure 36: Maximum-likelihood fitting of $m_{\rm ES}$, ΔE and $\cos\theta_H$ variables with $59.6\,\mathrm{fb}^{-1}$ continuum background MC sample and on-resonance data $m_{\rm ES}$ sideband.

Figure 40 shows the $m_{\rm ES}$, ΔE and $\cos\theta_H$ distributions from the other high kaon resonance $B \to K^{**}\gamma$ MC samples done with the $K^+\pi^-$ reconstruction and cuts. Weighting has been used because of the different theoretically predicted branching fractions (theoretical values in [21] are used), and the total yield in an $81.4\,\mathrm{fb}^{-1}$ data sample from high kaon resonance $B \to K^{**}\gamma$ decays is 0.07 ± 0.13, which is too small to be taken into consideration compared to the estimated signal yield of 108.4.

This result agrees well with the study from $m_{\rm ES}$ and ΔE distributions from the $b \to s\gamma$ inclusive MC sample, which gives an estimate of the whole 3-body decay contributions as 0.0 ± 0.6 and is shown in Fig. 41.

6.3.2 3-body Sub-decays Crossing into $K_S\pi^\pm$ Mode

Figure 42 shows the $m_{\rm ES}$, ΔE and $\cos\theta_H$ distributions from the $B^0 \to K_2^*(1430)^0\gamma$ MC sample done with the $K_S\pi^\pm$ reconstruction and cuts. From

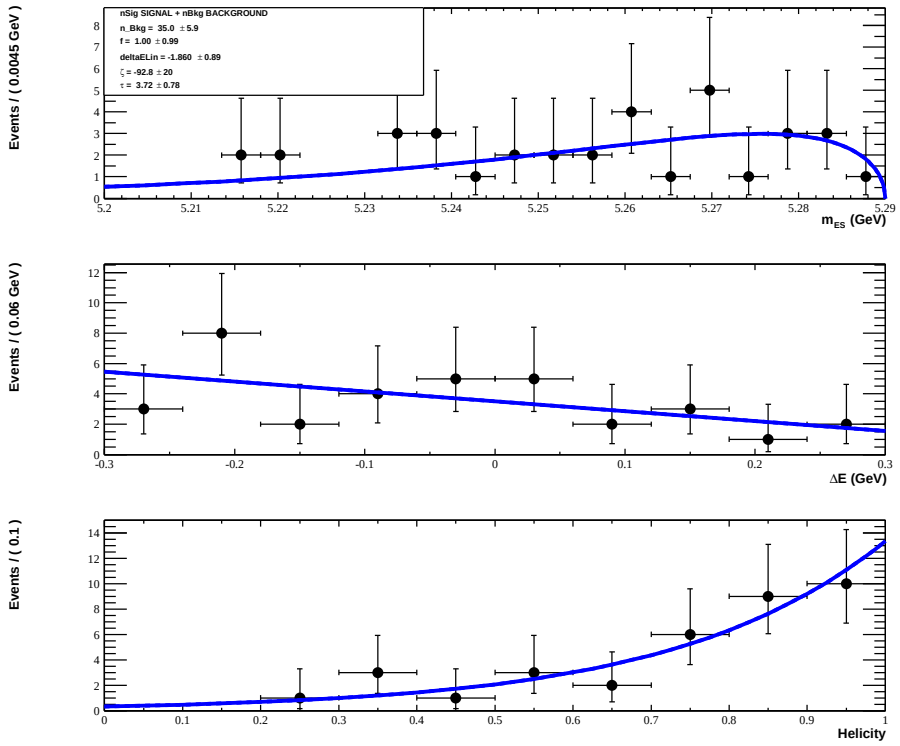

Figure 37: Maximum-likelihood fitting of $m_{\rm ES}$, ΔE and $\cos\theta_H$ variables with a $59.9\,{\rm fb}^{-1}$ $B^0\overline{B}^0$ background MC sample.

Fig. 39 we can see the yield is only 3.6 ± 3.6 from 37000 MC events, whose effect on efficiency is also small enough to be neglected. The expected contribution in $81.4\,{\rm fb}^{-1}$ data sample from the other high Kaon $B \to K^{**}\gamma$ modes is estimated to be 0.00 ± 0.04 using the MC sample, which is shown in Fig. 43. This result also is compatible with the study from $m_{\rm ES}$ and ΔE distributions from the $b \to s\gamma$ inclusive MC sample, which gives an estimate of the whole 3-body decay contributions as 0.4 ± 1.1 and is shown in Fig. 44.

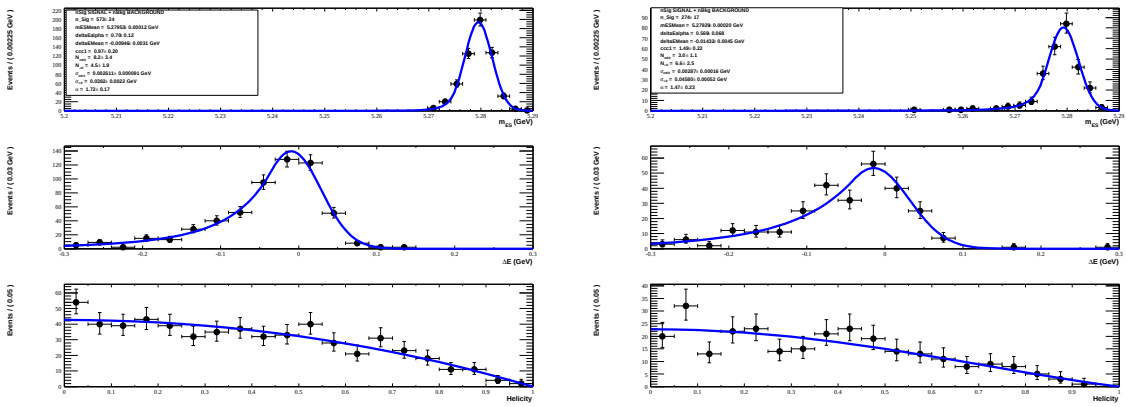

Figure 38: $m_{\rm ES}$, ΔE and $\cos\theta_H$ distributions from $B \to K^*(1410)\gamma$ MC sample (left plot is the neutral mode and right plot is the charged modes).

6.3.3 3-body Sub-decays Crossing into $K^{\pm}\pi^0$ Mode

Fig. 45 shows the $m_{\rm ES}$, ΔE and $|\cos\theta_H|$ distributions from the $B^+ \to K_2^*(1430)^+\gamma$MC sample done with the $K^+\pi^0$ reconstruction and cuts. From Fig. 45 we can see the yield is 7.7±4.1 from 37000 MC events, which means an adjustment of $+0.13 \pm 0.07\%$ on efficiency. The contribution in the $81.4\,\mathrm{fb}^{-1}$ data sample from the other high Kaon $B \to K^{**}\gamma$ modes is estimated to be 0.00 ± 0.04 using the MC information, which is shown in Fig. 46. This result also agrees well with the study from $m_{\rm ES}$ and ΔE distributions from the $b \to s\gamma$ inclusive MC sample, which gives an estimate of the whole 3-body decay contributions as 0.0 ± 0.4 and is shown in Fig. 47.

As a conclusion, only the $K^+\pi^0$ mode needs to apply a small correction on efficiency considering the 3-body decay contributions.

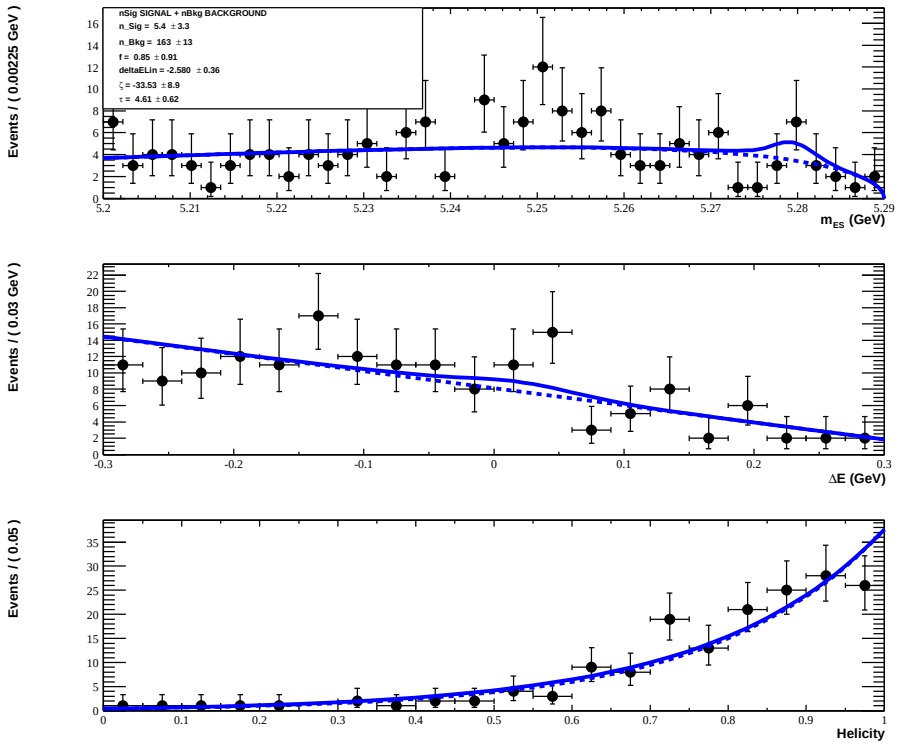

Figure 39: $m_{\rm ES}$, ΔE and $\cos\theta_H$ distributions from $B^+ \to K_2^*(1430)^+\gamma$MC sample with neutral mode reconstruction and cuts.

6.4 ML fit on 81.4 fb^{-1} on-resonance data-set

6.4.1 $m_{\rm ES}$ and ΔE Parameters

Due to the number of parameters in the PDFs, we'd better fix the values of some parameters.

The ML fit on $B \to K^*(892)\gamma$ MC and control samples is shown in Fig. 48 to study the $m_{\rm ES}$ and ΔE parameters. The parameters in Fig. 48 are listed in Table 16.

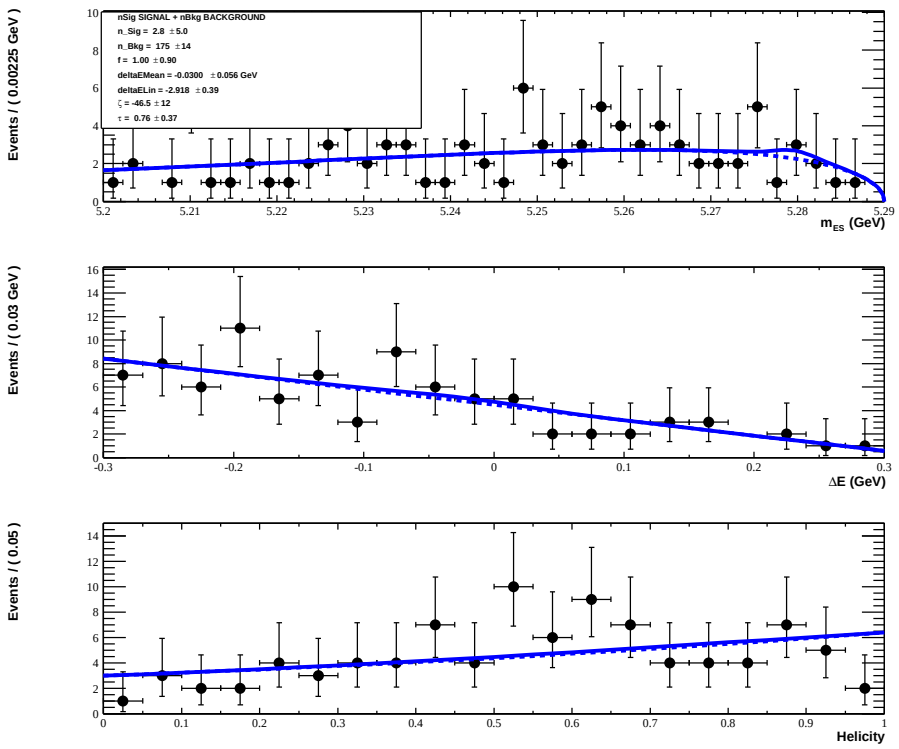

Figure 40: $m_{\rm ES}$, ΔE and $\cos\theta_H$ distributions from $B \to K^{**}\gamma$ MC samples with $K^+\pi^-$ mode reconstruction and cuts.

Based on the test on signal yield changes according to the constraint on different parameter combinations, we have determined the fitting strategy. The signal as well as background yields are allowed to vary in the fit. All the non-peaking background parameters are determined by the fit. The signal and peaking-background helicity angle, Crystal-Ball width and shape parameters are constrained to the MC expectations. The means of the signal $m_{\rm ES}$ and ΔE functions are constrained to the MC expectations, calibrated using $B \to K^*(892)\gamma$ candidates from MC simulation and data, while the

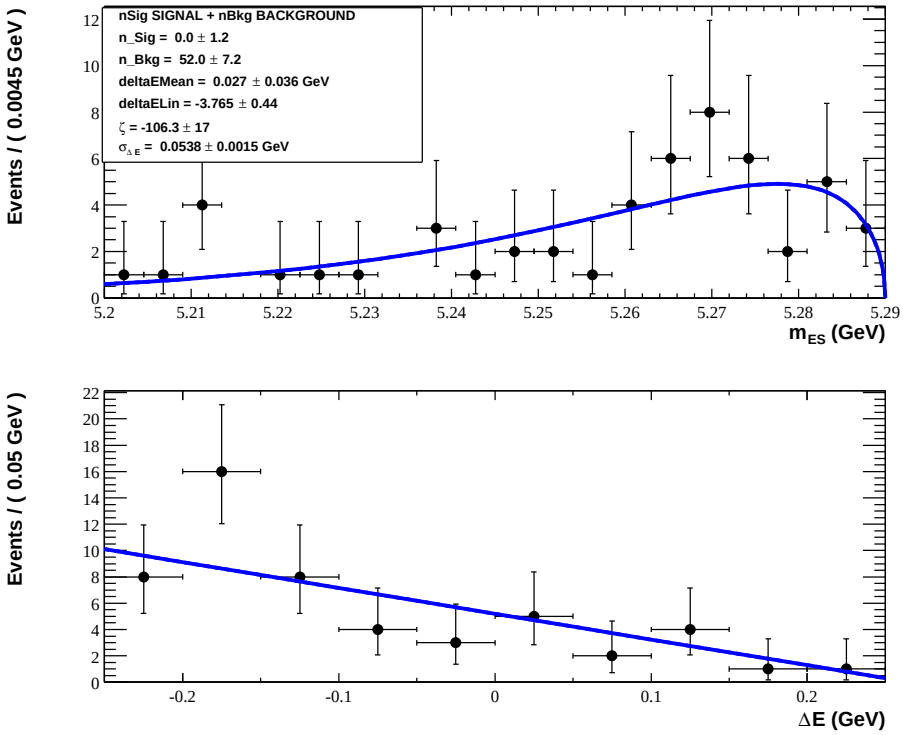

Figure 41: $m_{\rm ES}$ and ΔE distributions in 3-body decays from $b \to s\gamma$ inclusive MC samples with $K^+\pi^-$ mode reconstruction and cuts.

peaking-background means are allowed to float due to their complex composition.

Table 17 gives a summary of the strategy.

6.4.2 Toy MC Simulation

Figure 49, 50 and 51 shows the expected fit results on a 81.4 $\rm fb^{-1}$ on-resonance dataset of the three decay channels, which is simulated from a toy Monte Carlo sample (in the plots the top solid line is the total PDF, the other

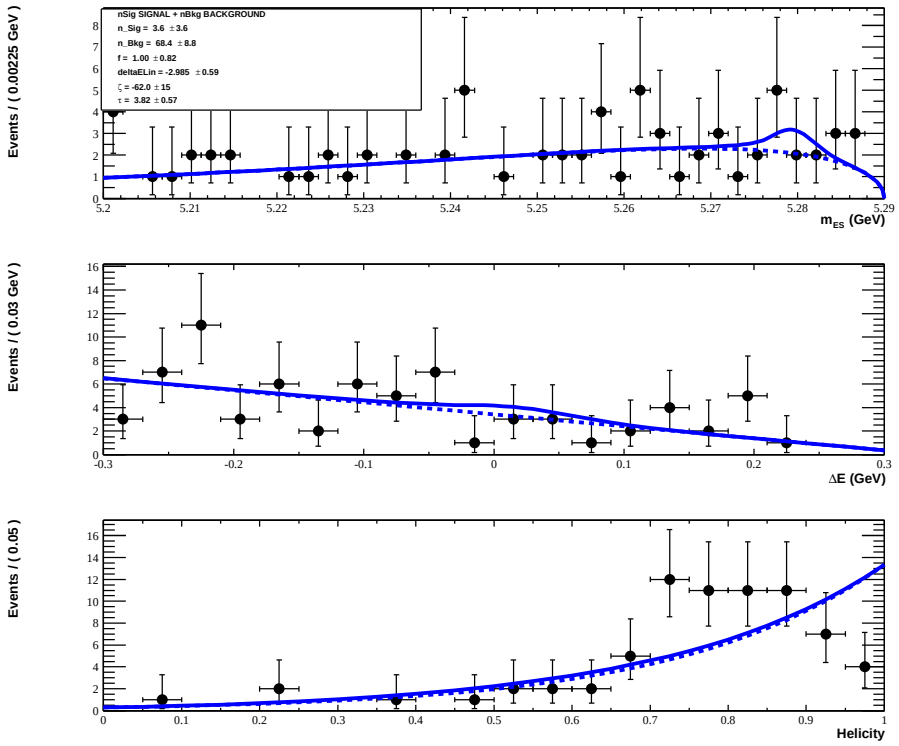

Figure 42: $m_{\rm ES}$, ΔE and $\cos\theta_H$ distributions from $B^0 \to K_2^*(1430)^0\gamma$ MC sample with $K_S\pi^\pm$ mode reconstruction and cuts.

solid line is the continuum background and the dashed line is the peaking background),

More toy MC study has been done for the systematics, which is described in more detail in section 8.4. In addition to the toy MC studies, we also test our fitting procedure with cocktail MC samples (estimated number of $B \to K_2^*(1430)\gamma$ signal MC+ estimated number of continuum background MC + estimated number of non-peaking $B\overline{B}$ background MC + estimated number of $B \to K^*(1410)\gamma$ (or $B \to K^*(1680)\gamma$) MC). The result is very

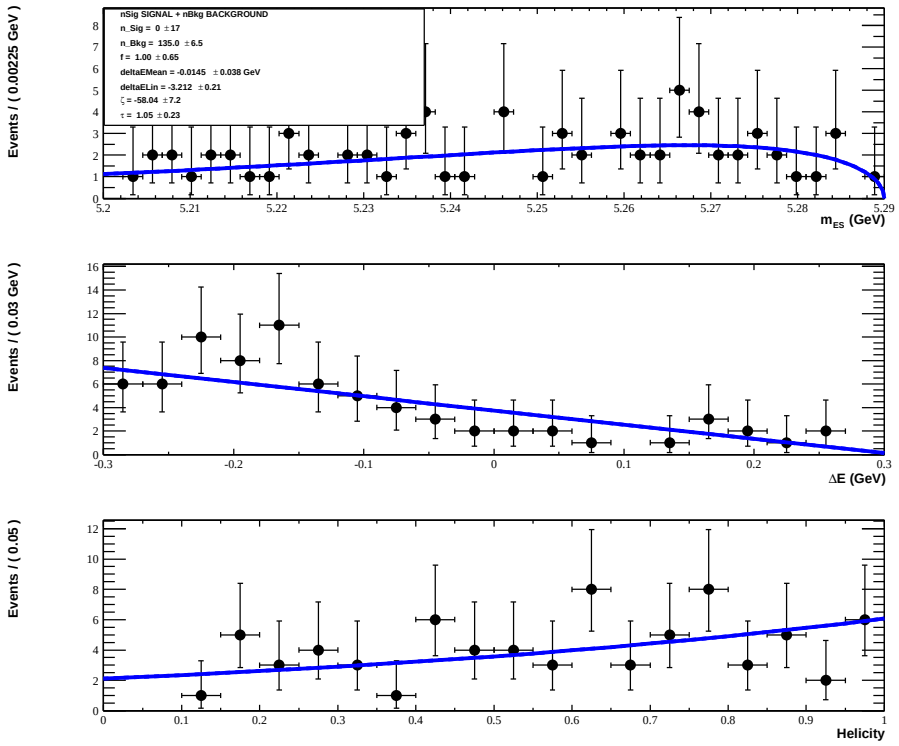

Figure 43: $m_{\rm ES}$, ΔE and $\cos\theta_H$ distributions from $B \to K^{**}\gamma$ MC samples with $K_S\pi^-$ mode reconstruction and cuts.

similar to the toy MC study. As an example, Fig. 52 shows one of the cocktail MC sample fit (94 signal events, 460 continuum background MC, 36 non-peaking $B\overline{B}$ MC sample and 91 $B \to K^*(1410)\gamma$ MC sample).

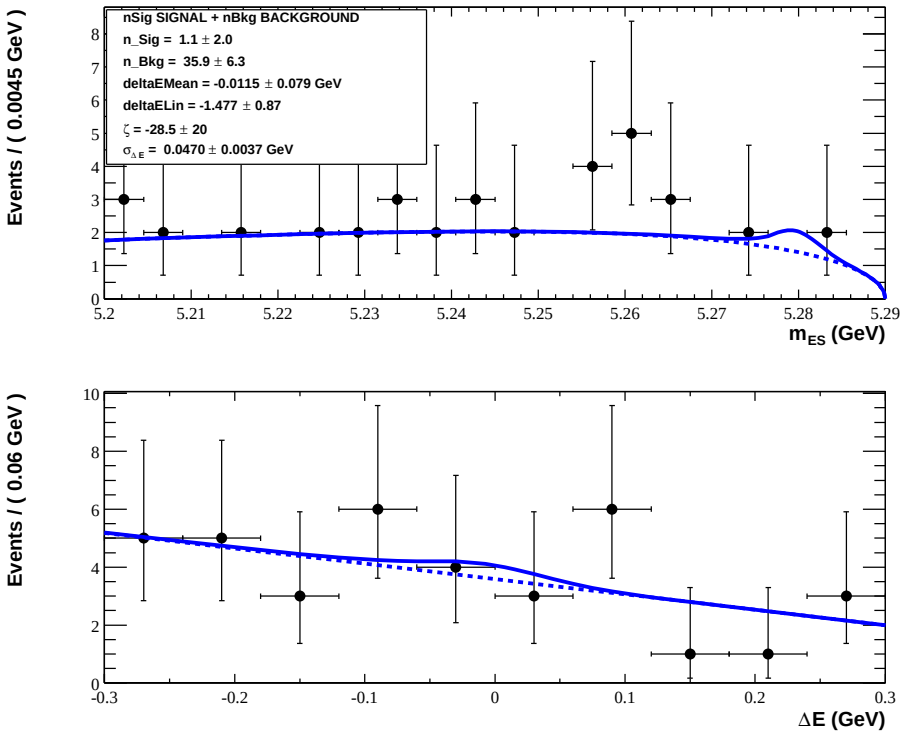

Figure 44: $m_{\rm ES}$ and ΔE distributions in 3-body decays from $b \to s\gamma$ inclusive MC samples with $K_S\pi^-$ mode reconstruction and cuts.

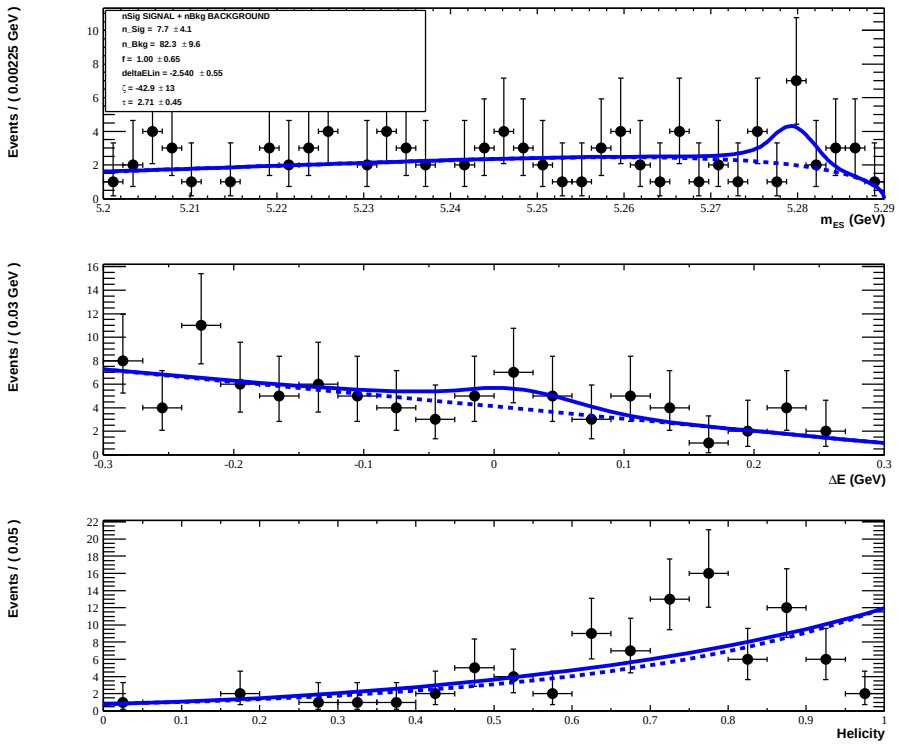

Figure 45: $m_{\rm ES}$, ΔE and $|\cos\theta_H|$ distributions from $B^0 \to K_2^*(1430)^0\gamma$ MC sample with $K^\pm\pi^0$ mode reconstruction and cuts.

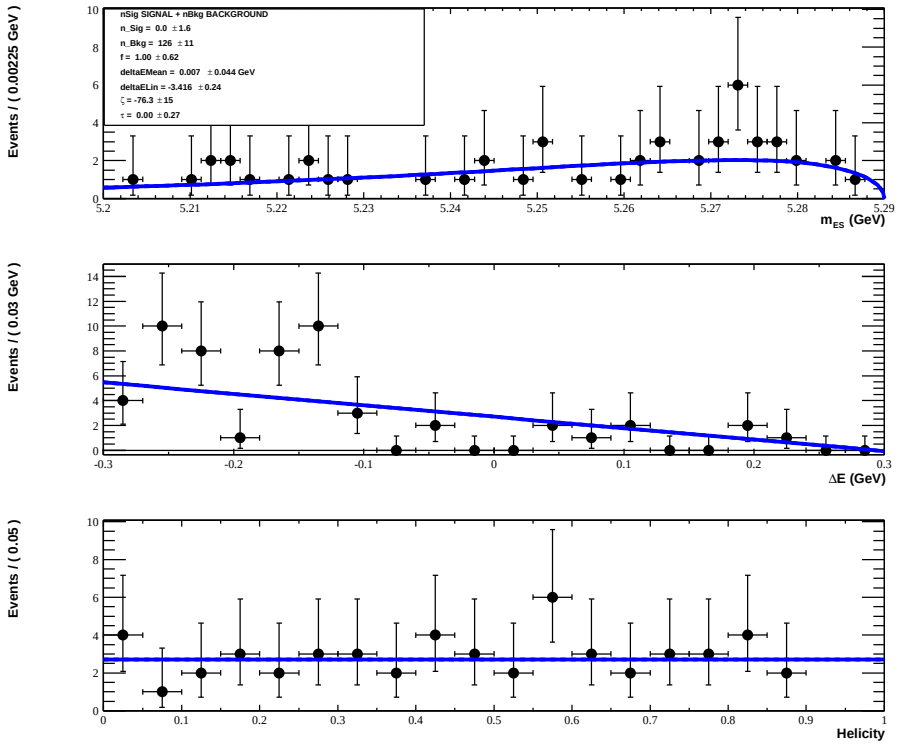

Figure 46: $m_{\rm ES}$, ΔE and $\cos\theta_H$ distributions from $B \to K^{**}\gamma$ MC samples with $K^+\pi^0$ mode reconstruction and cuts.

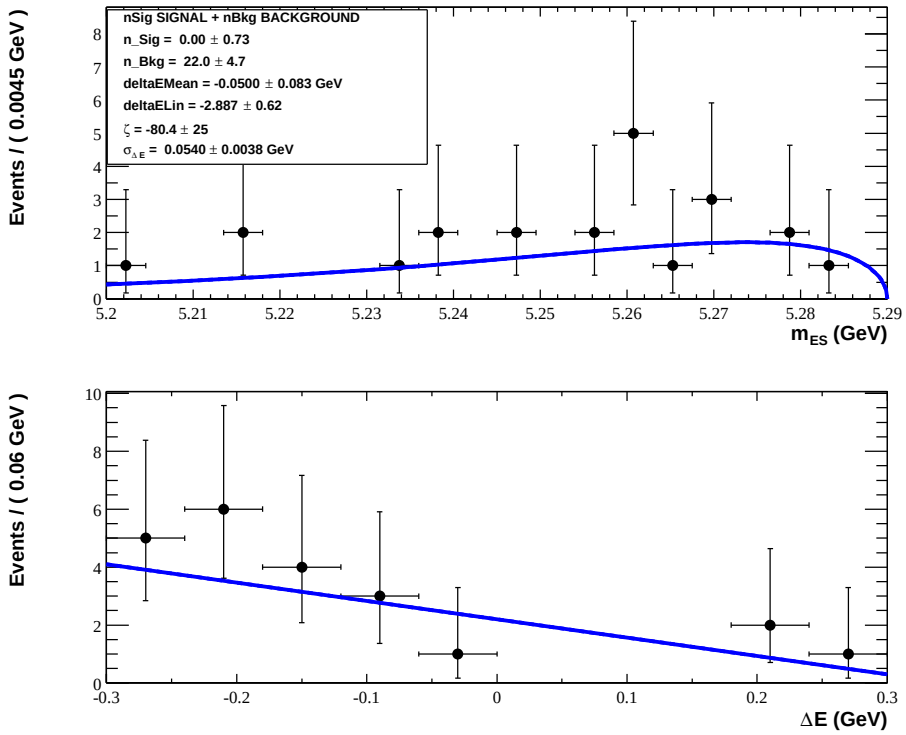

Figure 47: $m_{\rm ES}$ and ΔE distributions in 3-body decays from $b \to s\gamma$ inclusive MC samples with $K^+\pi^0$ mode reconstruction and cuts.

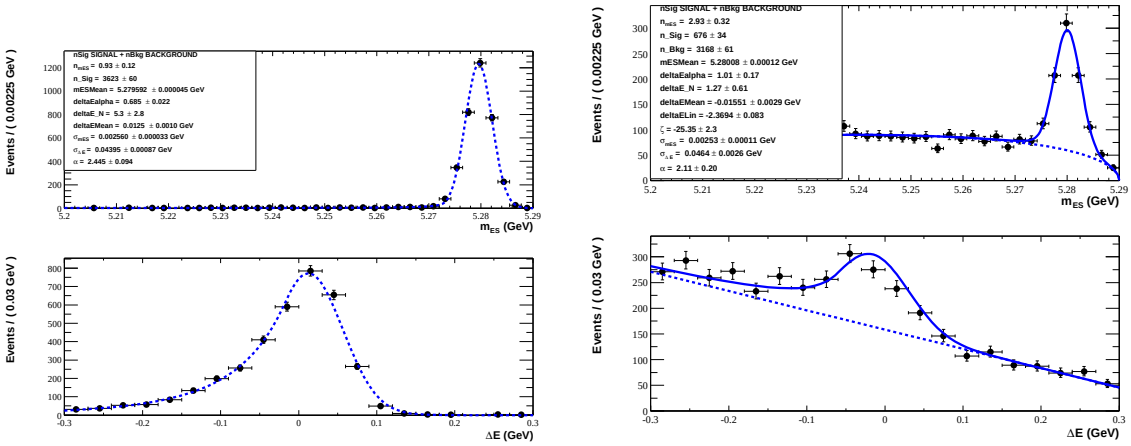

Figure 48: $m_{\rm ES}$, ΔE distributions and ML fit from $B^0 \to K^*(892)\gamma$ MC (left plot) and 81.4 fb^{-1} on-resonance data control sample (right plot) with all parameters floating.

Table 16: The $B \to K^*(892)\gamma$ MC and data control sample parameters

Parameter	Mode $B \to K^*(892)\gamma$	
	MC sample	Data Control sample
$m_{\rm ES}$ σ (MeV)	2.56 ± 0.03	2.53 ± 0.11
$m_{\rm ES}$ mean (MeV)	5279.63 ± 0.04	5280.08 ± 0.12
$m_{\rm ES}$ α	2.445 ± 0.09	2.11 ± 0.20
$m_{\rm ES}$ N	0.93 ± 0.12	2.93 ± 0.32
ΔE σ (MeV)	44.0 ± 0.9	46.4 ± 2.6
ΔE mean (MeV)	12.5 ± 2.0	-15.6 ± 2.9
ΔE α	0.68 ± 0.02	1.01 ± 0.17
ΔE N	5.3 ± 2.8	1.27 ± 0.61

	Parameter	Signal PDF	Continuum BG	Peaking BG
$m_{\rm ES}$	Mean	fixed	-	floating
	Width	fixed	-	fixed
	α, N	fixed	-	fixed
	Argus ζ	-	floating	-
ΔE	Mean	fixed	-	floating
	Width	fixed	-	fixed
	α, N	fixed	-	fixed
	Slope	-	floating	-
$\cos\theta_H$		fixed	floating	theoretical
Yield		floating	floating	floating

Table 17: Maximum likelihood fitting parameters

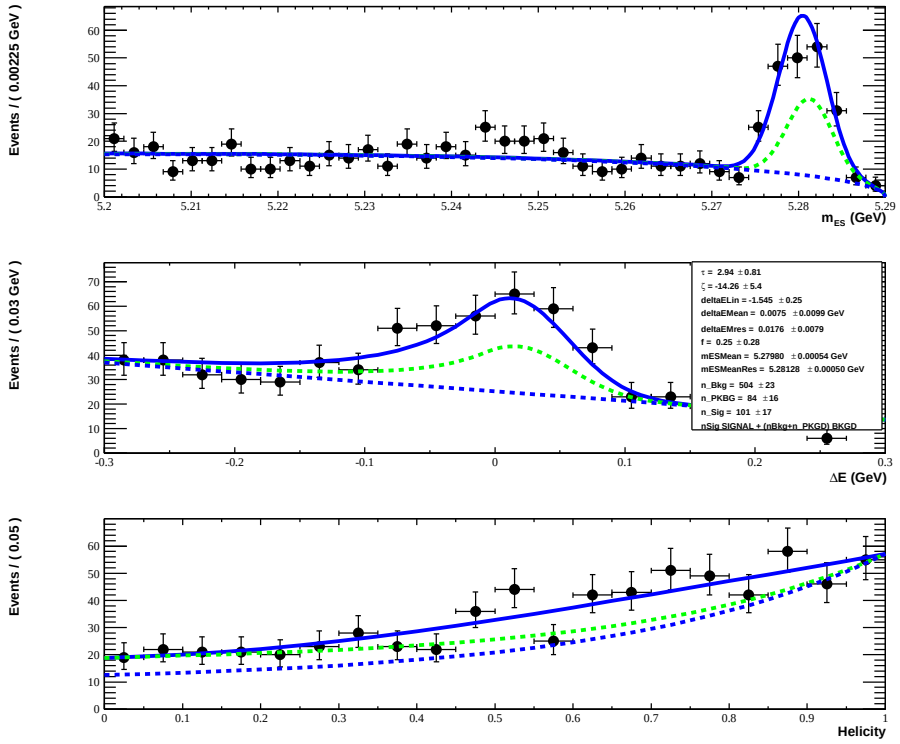

Figure 49: $m_{\rm ES}$, ΔE and $\cos\theta_H$ distribution and ML fit from 81.4 fb^{-1} on-resonance data (toy MC simulation for $K^+\pi^-$ channel with 94.0 signal yields expected).

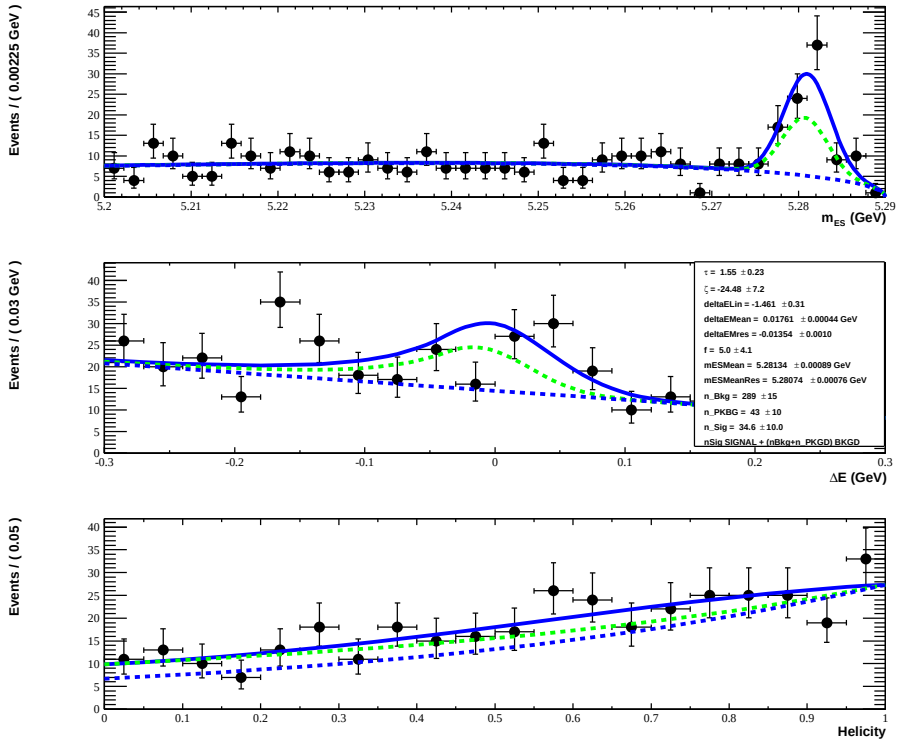

Figure 50: $m_{\rm ES}$, ΔE and $\cos\theta_H$ distribution and ML fit from 81.4 fb^{-1} on-resonance data (toy MC simulation for $K_S\pi^-$ channel with 28.9 signal yields expected).

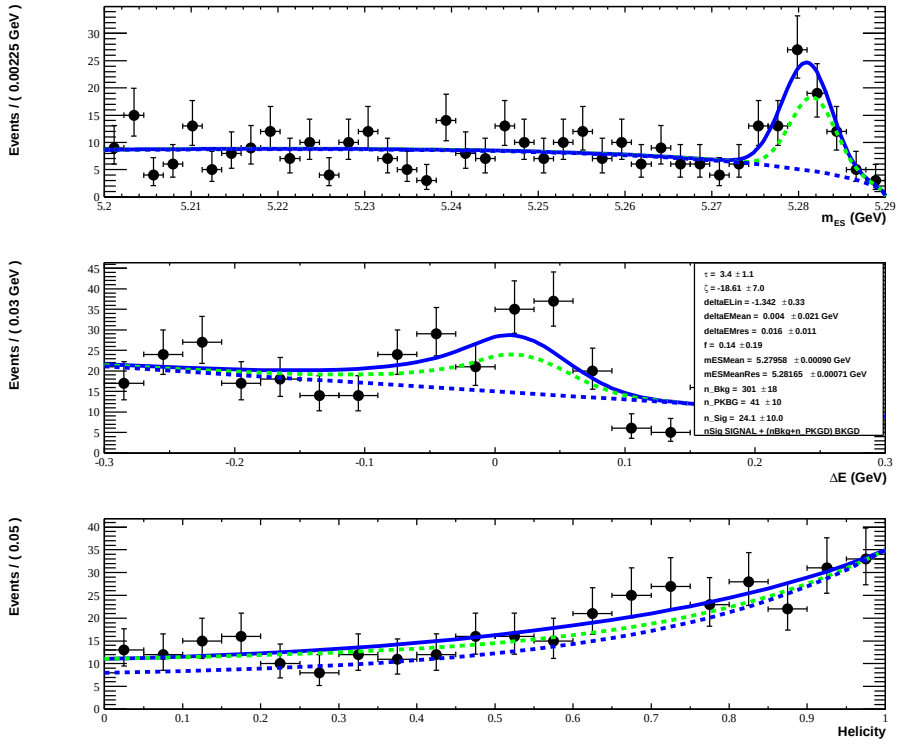

Figure 51: $m_{\rm ES}$, ΔE and $\cos\theta_H$ distribution and ML fit from 81.4 fb^{-1} on-resonance data (toy MC simulation for $K^+\pi^0$ channel with 27.7 signal yields expected).

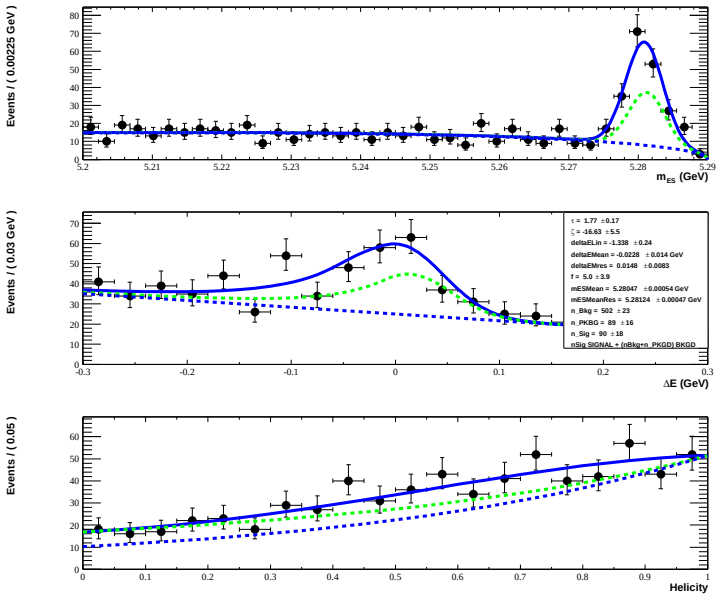

Figure 52: $m_{\rm ES}$, ΔE and $\cos\theta_H$ distribution and ML fit from 81.4 fb^{-1} on-resonance data (cocktail MC mixing for $K^+\pi^-$ channel with 94.0 signal yields expected).

7 CP Asymmetry

We also search for direct CP-violation in $B^0 \to K_2^*(1430)^0\gamma$ decays. This is defined as :

$$\mathcal{A}_{CP} = \frac{1}{1-2\eta} \cdot \frac{\mathrm{N}(\overline{B} \to \overline{K_2^*(1430)}\gamma) - \mathrm{N}(B \to K_2^*(1430)\gamma)}{\mathrm{N}(\overline{B} \to \overline{K_2^*(1430)}\gamma) + \mathrm{N}(B \to K_2^*(1430)\gamma)} \tag{22}$$

where η, is the mistag rate(the fraction of $B \to K_2^*(1430)\gamma$ reconstructed as charge conjugate reaction $\overline{B} \to \overline{K_2^*(1430)}\gamma$). We search for CP-violation using the neutral decay mode only. We determine the "measured a_{CP}"

$$a_{CP} = \frac{\Gamma\left(\overline{B} \to \bar{f}\right) - \Gamma\left(B \to f\right)}{\Gamma\left(\overline{B} \to \bar{f}\right) + \Gamma\left(B \to f\right)}\,. \tag{23}$$

directly from fitting. This measured a_{CP} is related the final $\mathcal{A}_{CP}$ by $a_{CP} = (1-2\eta)\mathcal{A}_{CP}$.

7.1 Tagging

Because the mode on which we study CP asymmetry is the neutral state $K_2^{*0}(1430) \to K^+\pi^-$, the charge of the final state charged particle identified as a kaon is used to tag the reconstructed events as either $B^0 \to K_2^*(1430)^0\gamma$, $K_2^{*0}(1430) \to K^+\pi^-$or its CP conjugate state. The mistag fraction in $K_2^{*0}(1430) \to K^+\pi^-$is estimated from the fully simulated Monte Carlo events. Table 18 shows the number of mistagged events from the signal region for the fully truth-matched Monte Carlo events, and for all Monte Carlo events regardless of truthmatching respectively. There are 14 of 8651 truthmatched events mistagged. The mistag rate is small, thus the estimated η on the total Monte Carlo in the signal box gives : $\eta_{K^+\pi^-} = 0.00163 \pm 0.00071$

Generated Events	Reconstructed Events $K^+\pi^-/K^-\pi^+$	Total
$K^+\pi^-$	1535 / 3	1538
$K^-\pi^+$	2 / 1511	1513
Total	1537 / 1514	3051

Table 18: $K_2^{*0}(1430) \to K^+\pi^-$truth-matched signal Monte Carlo. Number of truth-matched events in the signal box surviving all cuts generated and reconstructed in the CP modes.

7.2 CP Asymmetry Extraction

We extract the CP asymmetry using a simultaneous fit on the $B^0 \to K_2^*(1430)^0\gamma$ components and its CP conjugated component. The fitting PDFs are exactly the same as in the branching fraction study. As stated in Section 6, the parameters of the continuum background are floating, while in the CP asymmetry extraction fittings, we fix the continuum background parameters according to the values in the branching fraction fitting. There are no changes on the parameters of the signal and peaking background.

7.2.1 Yields from the Monte Carlo Components

Table 19 lists the yields of the various background Monte Carlo components in the opposite CP modes. The A_{CP} for each component is consistent with 0, as expected.

	Lumi.	Raw Yields		Total	
	(fb^{-1})	$K^+\pi^-$	$K^-\pi^+$	in $81.4\,\mathrm{fb}^{-1}$	A_{CP}
uds continuum	59.6	165 ± 30	169 ± 31	455.7 ± 59.5	-0.012 ± 0.13
$c\bar{c}$ continuum	64.3	241 ± 15	245 ± 15	615.3 ± 26.9	-0.0083 ± 0.044
$\tau^+\tau^-$	45.70	1	1	3.6	0.0
$uds + c\bar{c} + \tau^+\tau^-$				1074.6 ± 65.0	-0.0095 ± 0.060
Off-Res Data	9.49	63 ± 8	65 ± 10	1097.9 ± 109.8	-0.016 ± 0.099

Table 19: $K_2^{*0}(1430) \to K^+\pi^-$Monte Carlo and off-resonance data yields by CP mode

7.2.2 Toy Monte Carlo Study

We carry out some "embedded" Toy Monte Carlo studies to examine the effects of the correlations in the signal data on the fit parameters. The "embedded" Toy Monte Carlo means that in creating the Monte Carlo Toys, instead of using a PDF to generate events, we select events directly from the Monte Carlo data. We vary the number of generated signal events according to a Poisson distribution about the Monte Carlo expectation in 81.4 fb^{-1} and the samples were randomly selected from the fully simulated Monte Carlo set. The study includes 800 embedded toy experiments. The limited size of the fully simulated data set will lead to slight correlations among the experiments. Figures 53 and 54 show the distribution of N_{sig} and $a_{CP,sig}$, which are summarized in Table 20.

The pulls of the fits are shown in Figure 55.

In summary, these sets of toy studies show there is no bias on the $A_{CP,sig}$

	Pure Toy Monte Carlo ($A_{CP,Sig} = 0.1$)		Embedded Toy ($A_{CP,Sig} = 0.0$)	
Variable	Mean	RMS	Mean	RMS
$nBBkg$	95.6	36.3	100.8	36.6
$nContBkg$	497.2	29.9	495.9	30.11
$nSig$	106.8	18.6	105.7	18.5
$a_{CP,Sig}$	0.103	0.041	0.00	0.047
$P0_{\Delta E}$	-0.21	0.11	-0.30	0.18
ξ	-21.6	5.3	-21.5	5.3
$< \Delta E >$	0.0196	0.0026	0.0208	0.0029
$\sigma_{\Delta E}$	0.0457	0.0028	0.0389	0.0025
$< m_{ES} >$	5.27968	0.00013	5.27954	0.00013
$\sigma_{m_{ES}}$	0.00264	0.00011	0.00266	0.00011

Table 20: Values of fit parameters for CP asymmetry fit from pure toy Monte Carlo study ($A_{CP,Sig} = 0.1$) and embedded toy study in $K_2^{*0}(1430) \rightarrow K^+\pi^-$mode.

from the fitting procedure we are using.

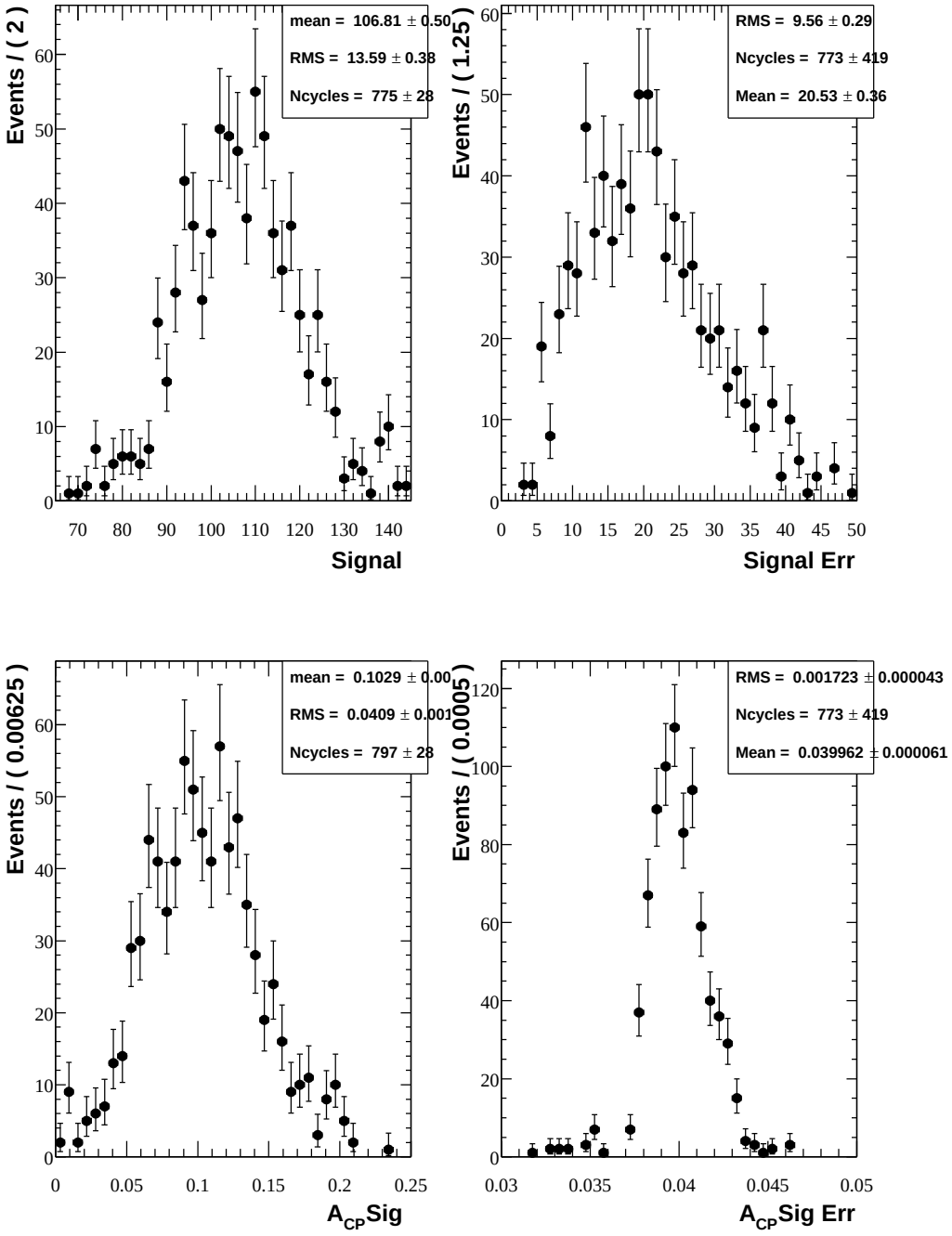

Figure 53: Distribution of N_{sig}, $a_{CP,sig}$ for $K_2^{*0}(1430) \to K^+\pi^-$decay mode with $A_{CP,sig} = 0.1$ pure Toy Monte Carlo.

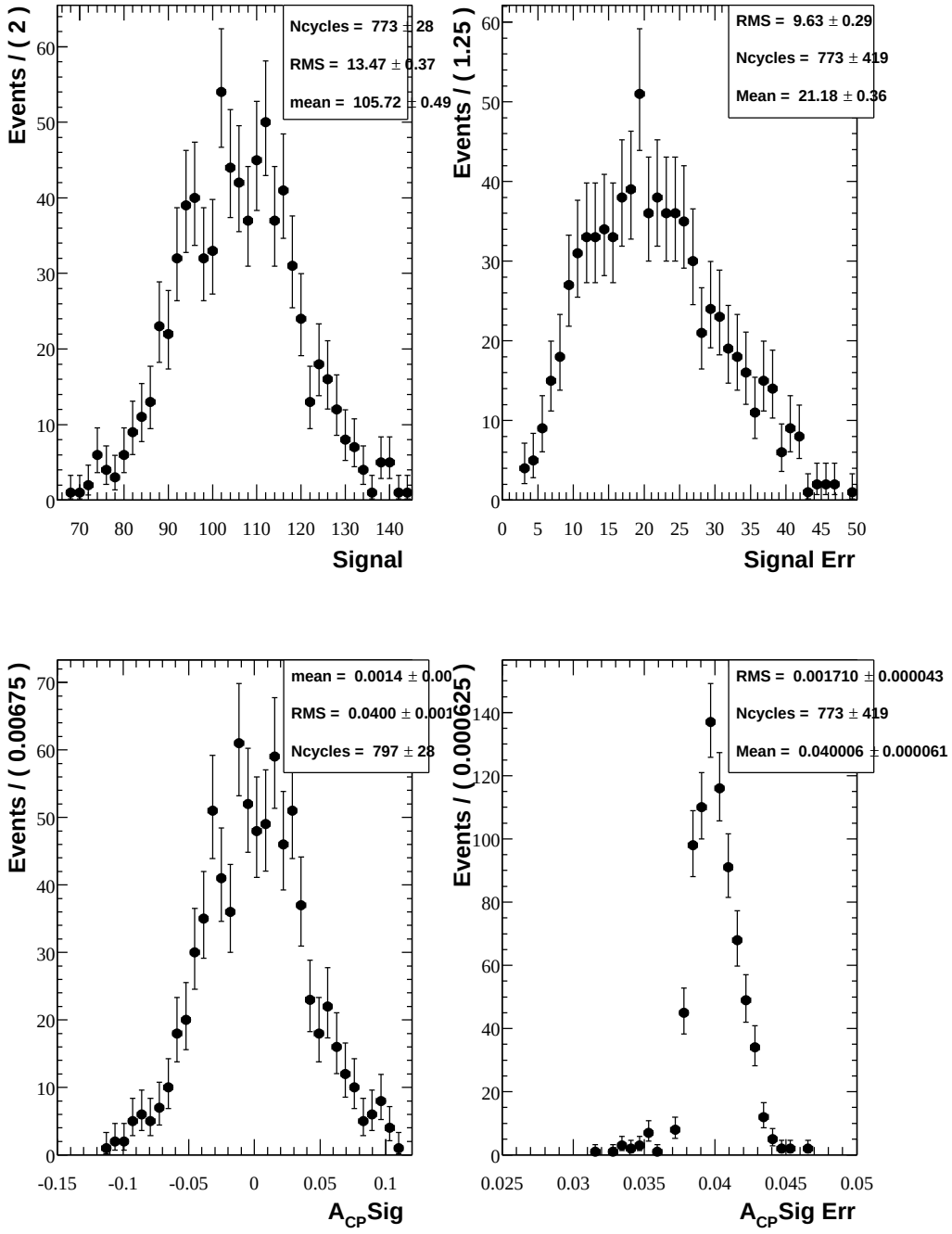

Figure 54: Distributions of N_{sig}, $a_{CP,sig}$ for $K_2^{*0}(1430) \to K^+\pi^-$decay mode with $A_{CP,sig} = 0.0$ embedded Toy Monte Carlo.

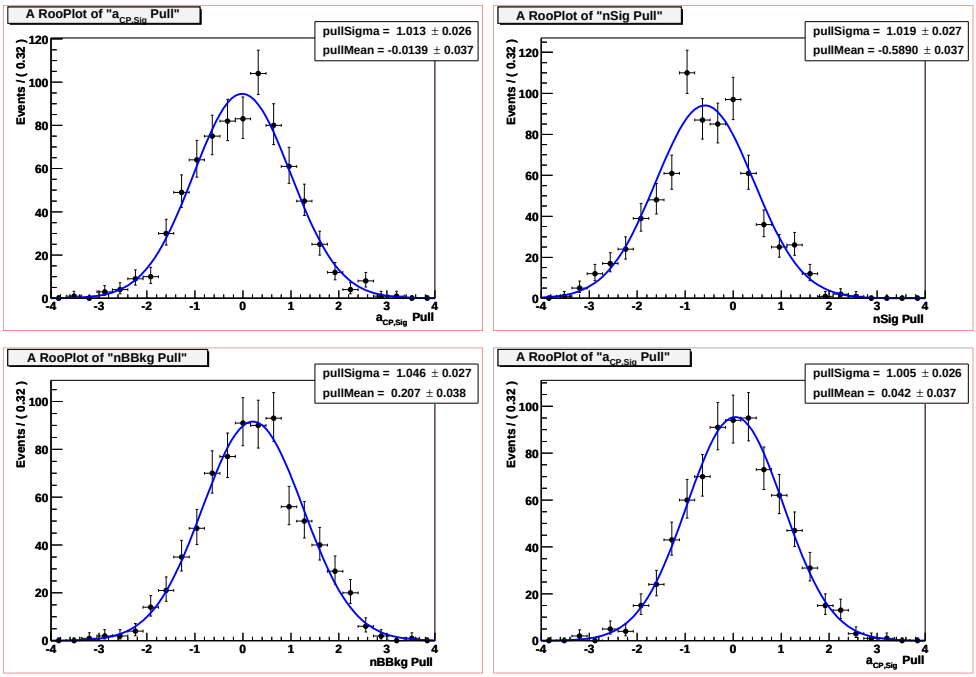

Figure 55: Distributions of N_{sig}, $a_{CP,sig}$ for $K_2^{*0}(1430) \rightarrow K^+\pi^-$decay mode with $A_{CP,sig} = 0.0$ embedded Toy Monte Carlo.

8 Systematic Errors

8.1 Photon Systematics

The difference in the photon detection efficiency is studied using data control samples and the signal MC, and measured as -2.5% [31]. This is used as a systematic bias that must be applied to the signal Monte Carlo efficiency. There is an associated uncertainty on this bias which is listed in Table 21, $\pm 2.5\%$. Please be advised that in the $K\pi^0$ mode, this uncertainty will be combined with the π^0 detection efficiency (5.0%) to be 7.5% in total.

The uncertainties related with the high energy photon reconstruction has been studied in the exclusive $B \to K^*(892)\gamma$ analysis. The systematic errors are the same as those discussed in [33]. They are summarized in Table 21.

Table 21: High Energy Photon Systematics

Photon detection efficiency	$\pm 2.5\%$
Photon energy scale	$\pm 1.0\%$
Photon energy resolution	$\pm 2.5\%$
$\pi^0(\eta)$ vetoes	$\pm 1.0\%$
Bump distance cut	$\pm 2.0\%$
Total	$\pm 4.3\%$

8.2 B-counting systematics

The total number of B mesons in our data sample is needed to normalize the branching fractions. The B-counting is discussed in BAD 30 [35]. The

corresponding systematic error is 1.1%.

8.3 Systematic Errors on Difference between Data and MC Efficiencies

Table 22 shows the systematic errors on the difference between data and MC detection efficiencies obtained from studies of data control samples, as reported in various references. The details are described in the following subsections.

Table 22: Systematic errors on difference between data and MC efficiencies

Systematic From	$\delta\epsilon/\epsilon$		
	$K\pi$	$K_S\pi$	$K\pi^0$
Tracking efficiency	$\pm$1.6%	$\pm$0.8%	$\pm$0.8%
$K^\pm$ identification	$\pm$1.0%	-	$\pm$1.0%
$\pi^\pm$ identification	$\pm$0.6%	$\pm$0.6%	-
π^0 efficiency	-	-	$\pm$2.5%
K_S efficiency	-	$\pm$3.0%	-
Total	$\pm$2.0%	$\pm$3.2%	$\pm$2.8%

8.3.1 Tracking Efficiency

We used the standard procedure adopted by the tracking group [32], which gives a 0.8% systematic uncertainty per track from the GoodTracksLoose list.

8.3.2 Particle Identification

Uncertainty in the efficiency of the Tight kaon selector and the Tight kaon veto for pions is obtained from measuring the efficiency of this selector in charmonium control samples and comparing the result with the same measurement performed for exclusive charmonium samples in Monte Carlo. This method yields a systematic uncertainty of 1.0% for Kaon ID and 0.6% for Pion ID, based on the statistical precision of these control samples.

8.3.3 π^0 Efficiency

The fourth line is about the simulation of the EMC hardware, reconstruction software and calibration in terms of π^0 efficiency, mass scale and resolution. It is studied by a data-MC comparison in the run-I data, based on exploiting τ "1-on-1 decays" $e^+e^- \to \tau^+\tau^-$. The uncertainty is determined to be 5.0%, and this is going to be added linearly with the photon detection efficiency and then quardratically combined with the other uncertainties in the $K^+\pi^0$ mode.

8.3.4 K_S Efficiency

Uncertainty in the efficiency of reconstructing K^0_S is a function of flight distance, after applying the efficiency correction [34]. This is obtained from the maximum variation of mean efficiency upon applying the alternative parameterization/cut values for K^0_S computation. The uncertainty is determined as 3% in Run $1 + 2$.

8.4 Error Related with the Fitting

Maximum likelihood fits can, in general, be biased to some extent because of the wrong pick-up of the PDF used in the fit. We tried some toy Monte Carlo studies to make sure we understood both signal and background distributions correctly and are fitting the parameters correctly. To do this we look at the behavior of the signal yield distributions.

The types of toy Monte Carlo that have been run include:

- PDF generated data sets - fitting back with the same model as used for generations (toy Monte Carlo).
- PDF generated data sets - fitting back using different models from that used for generation (incorrect PDF toy Monte Carlo).

8.4.1 Peaking Background Modeling

If you recall, in section 6.2.2 we stated that the $K\pi$ system was dominated by the $J = 1$ state (the $J = 0$ state is forbidden due to helicity conservation), thus having the helicity distribution as $\mid \sin^2\theta^*_H \mid$. The systematic uncertainty on peaking background modeling comes from the contributions from higher order J contributions.

If we expand the spacial wave-function $\chi = f_1 * e^{(-i\phi_1)} * \chi(J = 1) + f_2 * e^{(-i\phi_2)} * \chi(J = 2) + ...$, in which $|f_i|^2$ is the magnitude of the $J = i$ contribution and the ϕ_i is the phase angle of $J = i$ component. We assume $\frac{|f_2|^2}{|f_1|^2} < 20\%$ and study the strongly aligned/anti-aligned cases, $\phi_1 - \phi_2 = 0, \pi$.

The test is carried out on toy MC samples combining the estimated signal (94.0) and non-peaking background (497.0) events in $81.4\,\mathrm{fb}^{-1}$ and

$B^0 \to K_2^*(1430)^0\gamma(K_2^{*0}(1430) \to K^+\pi^-)$	$\frac{\lvert f_2\rvert^2}{\lvert f_1\rvert^2}$	$\phi_1 - \phi_2$	Signal yield variation (%)
	0	$0/\pi$	0.0/0.0
	0.20	$0/\pi$	$+3.5/-3.3$
$B^+ \to K_2^*(1430)^+\gamma(K_2^{*+}(1430) \to K_S\pi^+)$			
	0	$0/\pi$	$+0.1/0.0$
	0.20	$0/\pi$	$+4.4/-4.9$
$B^+ \to K_2^*(1430)^+\gamma(K_2^{*+}(1430) \to K^+\pi^0)$			
	0	$0/\pi$	$+0.2/-0.1$
	0.20	$0/\pi$	$+4.6/-4.8$

Table 23: Toy Monte Carlo study on fitting uncertainty.

different sets of peaking background toy MC events separately between the upper-lower limits (38.6-162.6) estimated from MC, in which the peaking background helicity is a mixture of $J = 1$ and 20% $J = 2$ components with phase angle 0 and π. We fit the toy Monte Carlo sample with the same procedure as will be done in data fitting.

The same procedures are repeated with the $K_S\pi^+$ and $K^+\pi^0$ decay channels. We summarize the study made above in Table 23. We choose the values of the biggest relative variation as the systematic errors on efficiency, which are 3.5%, 4.9% and 4.8%.

8.4.2 Crystal Ball Width

The width of the Crystal Ball (in signal $m_{\rm ES}$ PDF, signal ΔE PDF) function is fixed in the fits to the data. The values which are used are obtained

from the fits to the $B \to K_2^*(1430)\gamma$ MC sample. To obtain a systematic uncertainty related with this procedure, we vary the width by the 1σ error of the widths and check the changes in the signal yields.

8.4.3 Crystal Ball Shape Parameters

The uncertainty related with the Crystal Ball shape parameters are obtained in the same method as the width.

8.4.4 Significance of Signal

We have estimated the statistical significance of the signal in Table 29, we will include systematic uncertainties in this calculation through the following procedure. First, we increase the mean peaking backgrounds by one standard deviation in their uncertainty. Secondly, among the various choices of signal fitting described in the above paragraphs which are used to bound our systematic uncertainty on the signal yield, we choose the combination which gives the minimum yield. The change in lnL between the fits is calculated and used to accept or reject the null hypothesis. The results for all modes are listed in Table 24.

8.5 Sub Branching Fraction Systematic Error

We used the $K\pi$ two-body decays of $K_2^*(1430)$ to reconstruct the hadron. The two-body decay branching fraction we use is $(49.9 \pm 1.2)\%$, from [28]. So the corresponding uncertainty is 2.4%.

Table 24: Significance of $B \to K_2^*(1430)\gamma$signals

Mode	Signal yield	Stat. Significance	Stat.+Syst. Significance
$B^0 \to K_2^*(1430)^0\gamma$ $(K_2^{*0}(1430) \to K^+\pi^-)$	69.2 ± 14.1	5.8	5.7
$B^+ \to K_2^*(1430)^+\gamma$ $(K_2^{*+}(1430) \to K_S\pi^+)$	29.3 ± 10.3	3.3	3.1
$B^+ \to K_2^*(1430)^+\gamma$ $(K_2^{*+}(1430) \to K^+\pi^0)$	20.5 ± 9.2	2.6	2.2

8.6 Systematic Error on $K_2^*(1430)$ Mass

The peak value and width of the $K_2^*(1430)$ mass is not clearly understood, thus we have to introduce a systematic error for both neutral and charged modes. Since both the uncertainty on peak value and the width will affect the efficiency, we vary the invariant mass cut by $\sqrt{(1.1\sigma_{K\pi})^2 + \sigma_{m0}^2}$, and then check the corresponding changes on the efficiency. The uncertainties are listed in Table 25. We pick the most efficiency change as the systematic error.

8.7 Systematic Error on Background Suppression Cuts

The major continuum background suppression cuts lie on the thrust angle and neural-network cuts. The efficiency of the two cuts for both neutral and charged modes is cross-checked in data using the appropriate $B \to D\pi$

Table 25: $K_2^*(1430)$ Mass Cut Systematics

Mode	$\sigma_{K\pi}$	σ_{m0}	Cut Variation	Efficiency Change
$B^0 \to K_2^*(1430)^0\gamma$ $(K_2^{*0}(1430) \to K^+\pi^-)$	1.3 MeV	5.0 MeV	± 5.6 MeV	$+1.6/-1.3\%$
$B^+ \to K_2^*(1430)^+\gamma$ $(K_2^{*+}(1430) \to K_S\pi^+)$	1.5 MeV	2.7 MeV	± 3.3 MeV	$+1.0/-0.9\%$
$B^+ \to K_2^*(1430)^+\gamma$ $(K_2^{*+}(1430) \to K^+\pi^0)$	1.5 MeV	2.7 MeV	± 3.3 MeV	$+1.1/-0.7\%$

channels. We compare the efficiencies of the cuts in the data and MC $B^0 \to D^-\pi^+$ (for the neutral mode) and $B^+ \to D^0\pi^+$ (for the charged mode). The efficiencies are compared between these two samples to determine the systematic uncertainty. Figure 27 offers the $B \to D\pi^+$ MC and data control sample comparison on neural network output. Table 26 shows the efficiency comparison.

Table 26: Continuum Background Suppression Cut Systematics

Mode	$B \to D\pi$ MC	$B \to D\pi$ Data	$R = (Data/MC)$
$B^0 \to K_2^*(1430)^0\gamma$	$73.0 \pm 0.7\%$	$71.5 \pm 1.8\%$	$97.9 \pm 2.6\%$
$B^+ \to K_2^*(1430)^+\gamma$	$74.0 \pm 0.7\%$	$72.9 \pm 2.0\%$	$98.5 \pm 2.9\%$

8.8 MC statistics

There is also a small systematic error associated with the limited statistics of the signal MC sample which is used for all the efficiency numbers.

8.9 Results

The components of the systematic errors are listed in table 27.

8.10 Systematics in CP Asymmetry Measurement

There are two major sources for the systematics in CP asymmetry measurement, as listed below:

- Charge Asymmetry.
- PID Asymmetry.

8.10.1 Charge Asymmetry

The *BABAR* tracking efficiency group studied the systematics of tracking efficiency carefully. The study uses events of type $e^+e^- \to \tau^+\tau^-$, with one tau decaying leptonically and the other to three charged hadrons (plus an arbitrary number of neutrals). These events provide a measurement of the charge asymmetry in track reconstruction, by defining:

$$(\epsilon A)^{\pm} = \frac{N_4^{\pm}}{N_3^{\pm} + N_4^{\pm} + N_5^{\pm}}, \tag{24}$$

where the N_i^+ is the number of events with exactly i tracks, with the three tracks used to select the event having total charge -1 (i.e., the 4th

Table 27: Fractional systematic uncertainties (%) in the measurement of $\mathcal{B}(B \to K_2^*(1430)\gamma)$.

Uncertainty			
	$K^{\pm}\pi^{\mp}$	$K_S^0\pi^{\pm}$	$K^{\pm}\pi^0$
B-counting	1.1	1.1	1.1
Photon detection efficiency	2.5	2.5	7.5
Photon energy scale	1.0	1.0	1.0
Photon energy resolution	2.5	2.5	2.5
Photon isolation	2.0	2.0	2.0
π^0/η veto	1.0	1.0	1.0
K^+/π^+ tracking	1.6	0.8	0.8
Kaon ID	1.0	...	1.0
Pion ID	0.6	0.6	...
K_S^0 efficiency	...	3.0	...
Sub-mode branching fraction	2.4	2.4	2.4
$K_2^*(1430)$ mass/width	1.6	1.0	1.1
Signal PDF parameters	3.9	5.8	6.3
Background suppression	2.6	2.9	2.9
Peaking-background modeling	3.5	4.9	4.8
MC statistics	2.5	3.2	3.2
Total	8.4	10.	13.

track must be positive), the similarly for the N_i^-. With this, the asymmetry is defined as:

$$a_{\pm} = \frac{(\epsilon A)^+ - (\epsilon A)^-}{(\epsilon A)^+ + (\epsilon A)^-}, \tag{25}$$

The charge asymmetry is computed for data and MC separately and compared. In general, the uncertainty of charge asymmetry for the "GoodTrackLoose" candidates is 0.35% per track.

8.10.2 PID Asymmetry

The PID asymmetry comes from the asymmetric *BABAR* detector response to positive and negative tracks. The PID group has studied this asymmetry in the efficiencies of the PID selectors with the idea of "PID killing", which patches the MC to reflect the data efficiency of particle selectors. The efficiency is tabulated in bins of momentum, polar and azimuthal angles. The PID tables store the data efficiency and misidentification of the various particle selectors. The PID killing build the particle selectors using the tables. The PID killing code loops over candidates from the basic list in which the candidates have MC truth-matching information. A random number is created for every candidate in the event. All the PID tables are looped over and for each table the efficiency of the candidate is extracted. If the efficiency is bigger than the random number, the candidate will be appended to the corresponding particle list depending of its truth MC information.

In the absence of a CP asymmetry in the fundamental processes, the differences in PID efficiency for particles of opposite charge will appear as a

'fake' measured a_{CP}^{PID}:

$$a_{CP}^{PID} = \frac{\epsilon_{PID}(\overline{K^*}) - \epsilon_{PID}(K^*)}{\epsilon_{PID}(\overline{K^*}) + \epsilon_{PID}(K^*)}$$

Table 28 shows the a_{CP}^{PID} expected for the $K_2^{*0}(1430) \rightarrow K^+\pi^-$mode calculated from the PID efficiency tables. For a given PID selector, the PID efficiency tables are divided into bins based on RunI/RunII conditions, true particle type, magnitude of measured particle momentum, and direction of particle momentum. For each Run and particle type there are 20 bins of momentum magnitude and 2 bins of momentum polar angle. The efficiencies in Table 28 are calculated basically by convolving the PID tables and the momentum spectrum of the fully truth matched $K_2^{*0}(1430) \rightarrow K^+\pi^-$events surviving the skim and photon selection cuts.

For an efficiency calculation, a weight is assigned to each event. For the efficiencies for a single particle (kaon or pion PID only), the weight is the luminosity weighted sum of the RunI and RunII efficiencies for the particle momentum.

$$w_i(X) = \frac{\mathcal{L}_{RunI}}{\mathcal{L}_{Tot}}\epsilon_{table}(RunI, X, p_X) + \frac{\mathcal{L}_{RunII}}{\mathcal{L}_{Tot}}\epsilon_{table}(RunII, X, p_X)$$

The errors for the efficiencies were computed by varying the efficiencies in the PID tables by $\pm 1\sigma$ and adopting the maximum difference as an error. The efficiencies were varied to maximize the deviation of a_{CP}^{PID} from its central value, i.e. for the calculation of the kaon PID efficiency error, the K^+ efficiencies were all increased (decreased) by 1σ while the K^- efficiencies were simultaneously decreased (increased) by 1σ.

PID Selector	$\epsilon_{PID}(\overline{K_2^*(1430)})$	$\epsilon_{PID}(K_2^*(1430))$	a_{CP}^{PID}
$K^{\pm}$ (SMS K Tight)	0.8962±0.0081	0.9051±0.0079	-0.0049±0.0063
$\pi^{\mp}$ (SMS K Tight veto)	0.9915±0.0074	0.9973±0.0090	-0.0029±0.0058
Both PID cuts	0.8814±0.0110	0.8920±0.0120	-0.0078±0.0086

Table 28: CP Asymmetry PID : Faked a_{CP}^{PID} factors for $K_2^{*0}(1430) \to K^+\pi^-$signal Monte Carlo

8.10.3 Asymmetry Systematics Summary

In conclusion, the particle-antiparticle asymmetry in the detector response, which includes 0.35% uncertainty for the tracking efficiency and 1.5% uncertainty for the charged particle identification, predominantly contributes to the systematic uncertainty of the $\mathcal{A}_{CP}$ measurement. The nuclear interaction asymmetry, which arises from the different interaction probabilities of K^+ and K^- and of π^+ and π^-, is calculated in a similar way as in Ref. [37] and this component is 0.20%. Then the total $\mathcal{A}_{CP}$ measurement uncertainty is 1.6%. Combining this with the systematic on the tracking efficiency, we find the total systematic is 1.6% for $K_2^{*0}(1430) \to K^+\pi^-$.

Figures 56, 57 and 58 show the fitted $m_{\rm ES}$, ΔE and $\cos\theta_H$ distributions for the 3 modes in data, in which the dashed line is the continuum background, the dash-dotted line is the background in total and the solid one has signal included, along with the $\cos\theta_H$ distributions in the signal region (defined as $-0.15 < \Delta E < 0.10\,\text{GeV}$, $5.272 < m_{\rm ES} < 5.288\,\text{GeV}/c^2$). The signal and the calculated branching ratios for all 3 modes are given in Table 29. The signal significance has been evaluated from the change in the likelihood

when the fit is repeated with the signal yield set to zero.

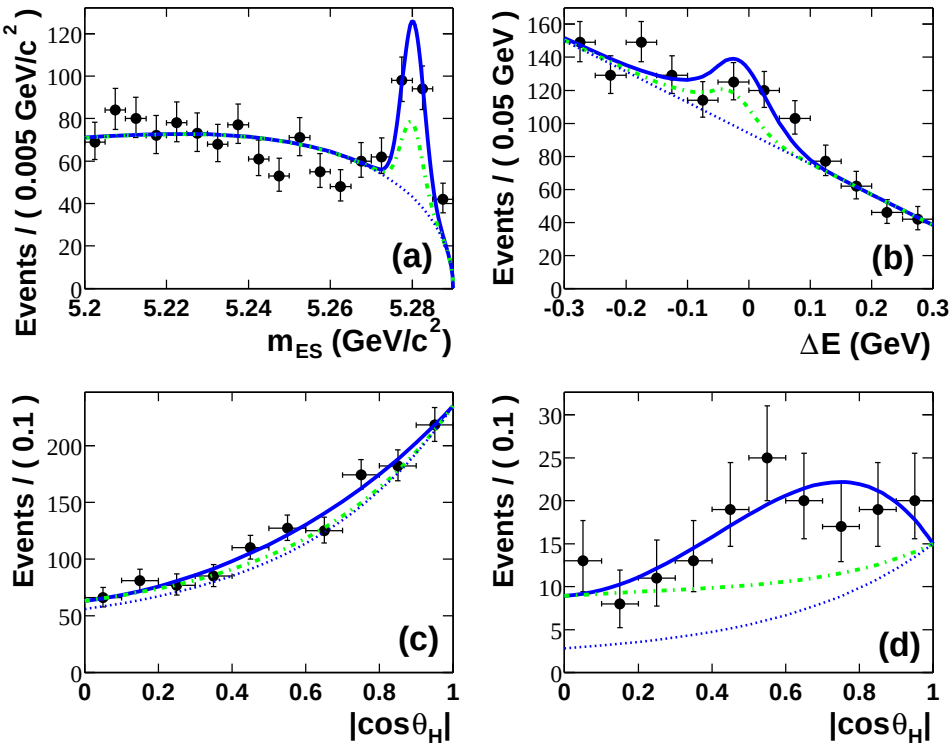

Figure 56: A fit to the $m_{\rm ES}$ (a), ΔE (b) and $\cos\theta_H$ (c) distributions for $B^0 \to K_2^*(1430)^0\gamma$, $K_2^*(1430)^0 \to K^+\pi^-$ candidates in data, and the $\cos\theta_H$ distribution (d) in the signal region. The solid line shows the result of the fit to the data. The peaking (dashed-dotted line) and non-peaking (dotted line) background contributions are also shown.

We also have the $m_{\rm ES}$ distribution (with $-0.15 < \Delta E < 0.1$ GeV cut) and ΔE distribution (with $5.272 < m_{\rm ES} < 5.288\,{\rm GeV}/c^2$ cut) for the 3 modes in Figs. 59, 60 and 61.

Fig. 62 shows the $K\pi$ invariant mass distribution where the cut on this

Mode	Efficiency (%)	Signal	Signal significance	$\mathcal{B}(B \to K_2^*(1430)\gamma)$ $\pm$(stat.)$\pm$(syst.)$\times 10^{-5}$
$K^+\pi^-$	6.4	69.2 ± 14.1	5.8	$1.22 \pm 0.25 \pm 0.10$
$K_S^0\pi^+$	1.9	29.3 ± 10.3	3.3	$1.69 \pm 0.59 \pm 0.16$
$K^+\pi^0$	1.9	20.5 ± 9.2	2.6	$1.23 \pm 0.55 \pm 0.15$

Table 29: The fitted signal yield, efficiency, and measured branching fraction $\mathcal{B}(B \to K_2^*(1430)\gamma)$.

quantity has been relaxed. The continuum background, estimated from the data outside the signal region, has been subtracted. The invariant mass is fit with a relativistic Breit-Wigner function plus a first-order polynomial background. There is a clear enhancement around $1.4\,\mathrm{GeV}/c^2$ both in the neutral and charged modes.

8.11 Goodness of Fit

For reference, we show the distribution of $-logL$ for the toy Monte Carlo experiments (produced with the same signal, peaking and non-peaking background yields as in unblinded data) in Fig. 63 and we check the $-logL$ values obtained from the 3 modes (the line in Fig. 63) compared with these distributions to determine if the quality of the fit is within the expected range. From the plot we can see that the actual $-logL$ in fitting agrees with the expectations.

Mode	Signal yield	A_{cp}
$K^+\pi^-$	31.1 ± 9.1	
$K^-\pi^+$	36.6 ± 9.9	-0.08 ± 0.15

Table 30: The fitted signal yield and measured A_{cp} for $K_2^{*0}(1430) \to K^+\pi^-$.

8.12 CP Asymmetry Result

Fig. 64 and 65 show the fitted $m_{\rm ES}$, ΔE and $\cos\theta_H$ distributions for the $K_2^{*0}(1430) \to K^+\pi^-$ and $\overline{K_2^{*0}(1430)} \to K^-\pi^+$ in data. The yields and corresponding CP asymmetry result are listed in Table 30.

8.13 Summary

A method described in BAD 33 has been used to combine the results from $K_S^0\pi^+$ and $K\pi^0$ modes. By including the systematic error, the measured $B \to K_2^*(1430)\gamma$ branching ratios are listed in Table 31, in which we also listed the existing publication results and the most recent theoretical prediction.

This doctoral research deals with an important physics issue being addressed in three current major experiments and of interest to a large community of scientific people. We have presented a preliminary measurement of the branching fraction of $B^0 \to K_2^*(1430)^0\gamma$ as $(1.22 \pm 0.25 \pm 0.10) \times 10^{-5}$ with a 5.7σ statistical significance, which is an improvement over previous experimental results, while still being in agreement. The first observation of $B^+ \to K_2^*(1430)^+\gamma$ branching fraction is reported with a preliminary measurement of the branching fraction as $(1.45 \pm 0.40 \pm 0.15) \times 10^{-5}$ with a 3.8σ

Table 31: $B \to K_2^*(1430)\gamma$ Branching Ratio

Channel	Branching Fraction
$B^0 \to K_2^*(1430)^0\gamma$	$(1.22 \pm 0.25 \pm 0.10) \times 10^{-5}$
$B^+ \to K_2^*(1430)^+\gamma$	$(1.45 \pm 0.40 \pm 0.15) \times 10^{-5}$
CLEO result	$(1.66 \pm 0.56 \pm 0.13) \times 10^{-5}$
BELLE result	$(1.50 \pm 0.55 \pm 0.10) \times 10^{-5}$
Theory	$(1.78 \pm 0.15) \times 10^{-5}$

statistical significance, made by combining the results from $K_S^0\pi^+$ and $K\pi^0$ modes. Both results agree with the theoretical prediction from the relativistic form-factor model of Veseli and Olsson [21]. The $\mathcal{A}_{CP}$ is measured to be $-0.08 \pm 0.15 \pm 0.01$, thus no evidence of direct *CP* violation is observed. Our improved results on measurements of $B \to K_2^*(1430)\gamma$will help to understand the inclusive $b \to s\gamma$ study, and the techniques used in this analysis can be easily extended into the study on $B \to K_1(1400)\gamma$ for photon polarization measurement, which may serve as an independent test platform to probe physics beyond Standard Model!

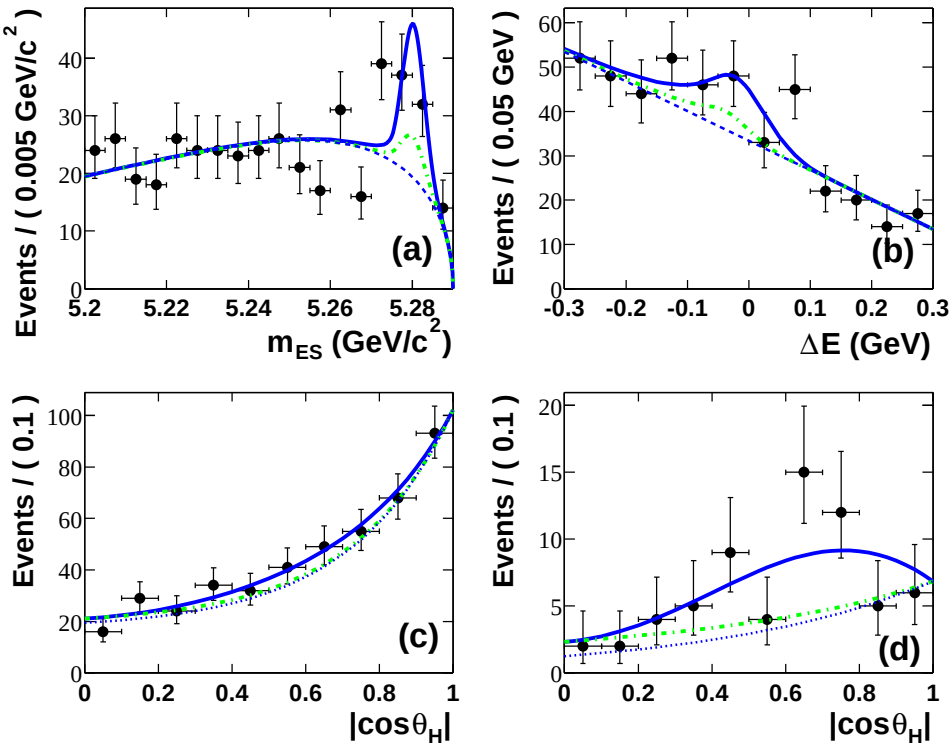

Figure 57: A fit to the $m_{\rm ES}$ (a), ΔE (b) and $\cos\theta_H$ (c) distributions for $B^+ \to K_2^*(1430)^+\gamma$, $K_2^*(1430)^+ \to K_S^0\pi^+$ candidates in data, and the $\cos\theta_H$ (d) distribution in the signal region. The solid line shows the result of the fit to the data. The peaking (dashed-dotted line) and non-peaking (dotted line) background contributions are also shown.

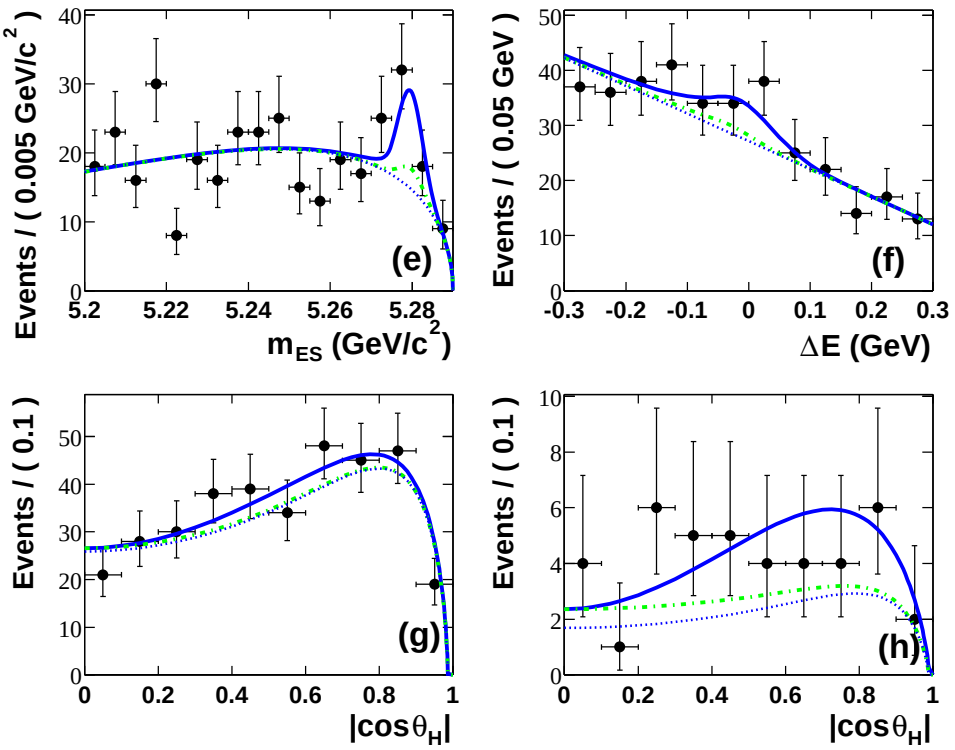

Figure 58: A fit to the $m_{\rm ES}$ (e), ΔE (f) and $\cos\theta_H$ (g) distributions for $B^+ \to K_2^*(1430)^+\gamma$, $K_2^*(1430)^+ \to K^+\pi^0$ candidates in data, and the $\cos\theta_H$ (h) distribution in the signal region. The solid line shows the result of the fit to the data. The peaking (dashed-dotted line) and non-peaking (dotted line) background contributions are also shown.

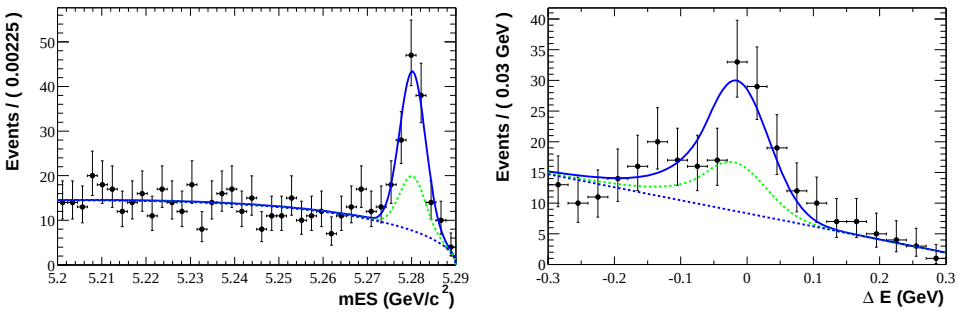

Figure 59: $m_{\rm ES}$ distribution with ΔE cut and ΔE distribution with $m_{\rm ES}$ cut for the $K^+\pi^-$ mode.

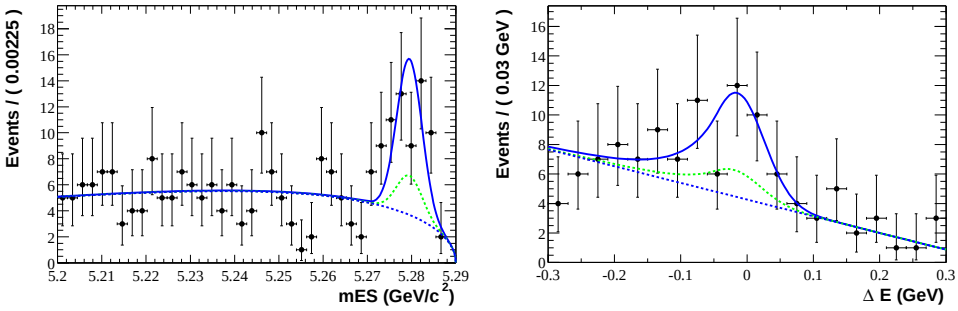

Figure 60: $m_{\rm ES}$ distribution with ΔE cut and ΔE distribution with $m_{\rm ES}$ cut for the $K^0_S\pi^+$ mode.

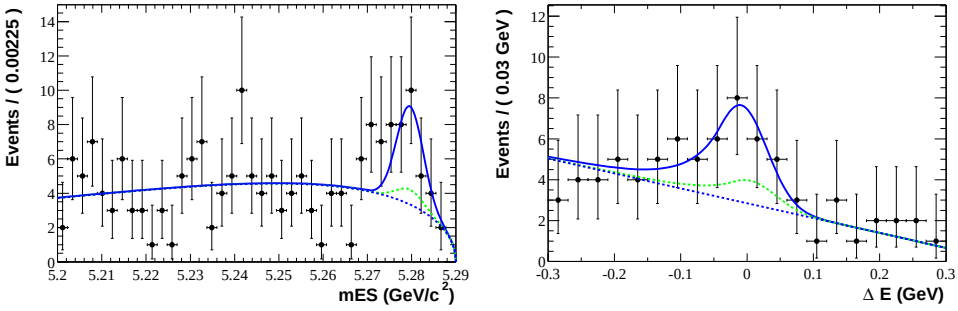

Figure 61: $m_{\rm ES}$ distribution with ΔE cut and ΔE distribution with $m_{\rm ES}$ cut for the $K^+\pi^0$ mode.

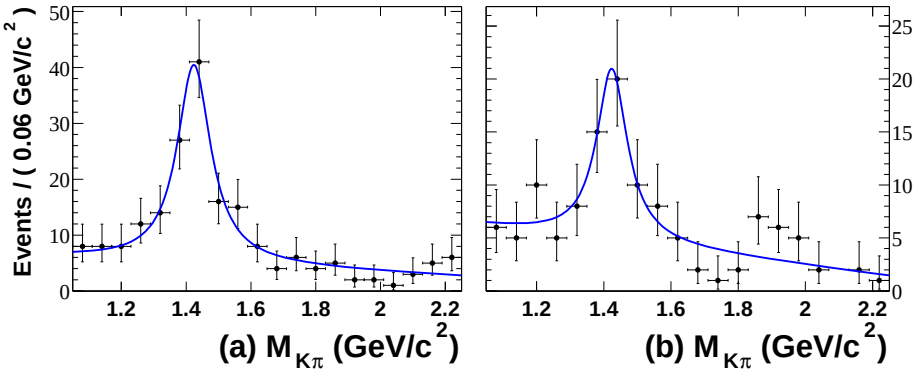

Figure 62: $K^+\pi^-$ (a) and $K^0_S\pi^+$ and $K^+\pi^0$ (b) invariant mass distributions for the signal region after background subtraction

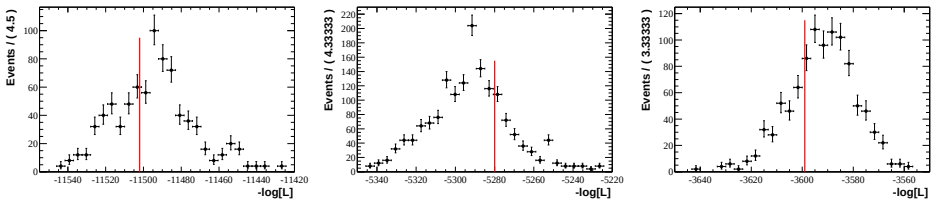

Figure 63: $-logL$ distribution in the toy MC study: $K^+\pi^-$ mode (left); $K^0_S\pi^+$ (middle) and $K^+\pi^0$ (right) modes.

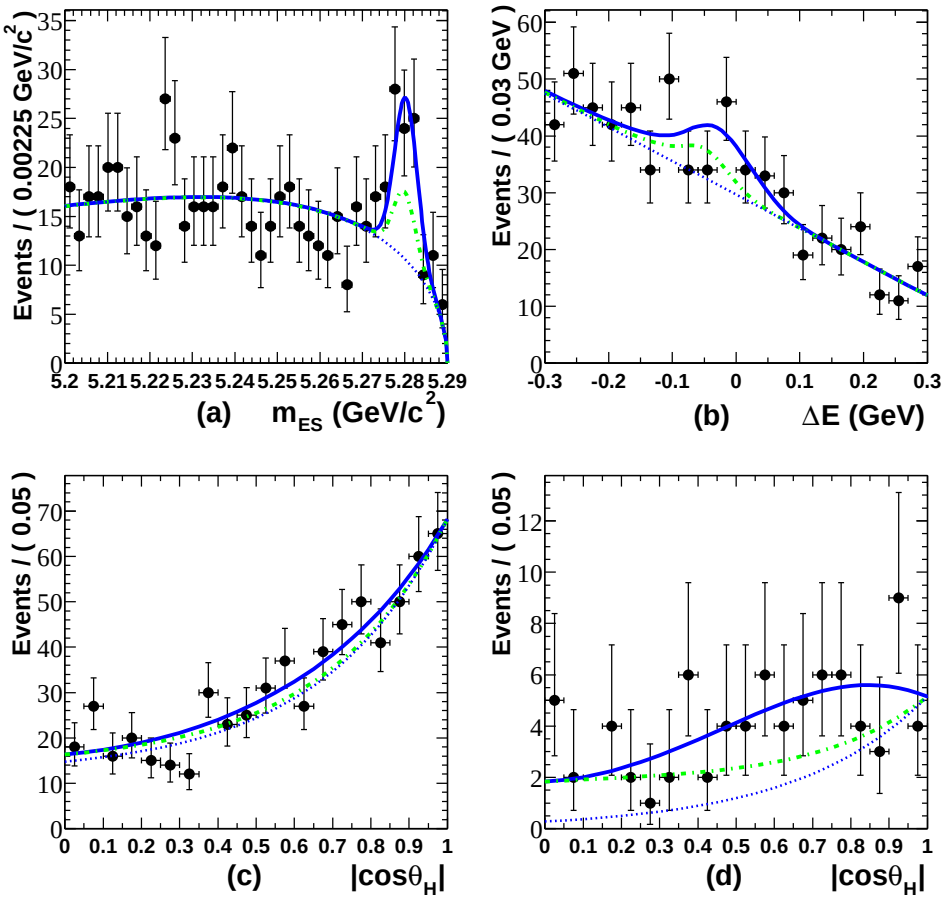

Figure 64: A fit to the $m_{\rm ES}$ (a), ΔE (b) and $\cos\theta_H$ (c) distributions for $B^0 \to K_2^*(1430)^0\gamma$, $K_2^{*0}(1430) \to K^+\pi^-$ in data, and the $\cos\theta_H$ distribution in the signal region (d). (The solid line shows a fit to the data with the peaking (dash-dot) and non-peaking (dash) backgrounds as indicated.)

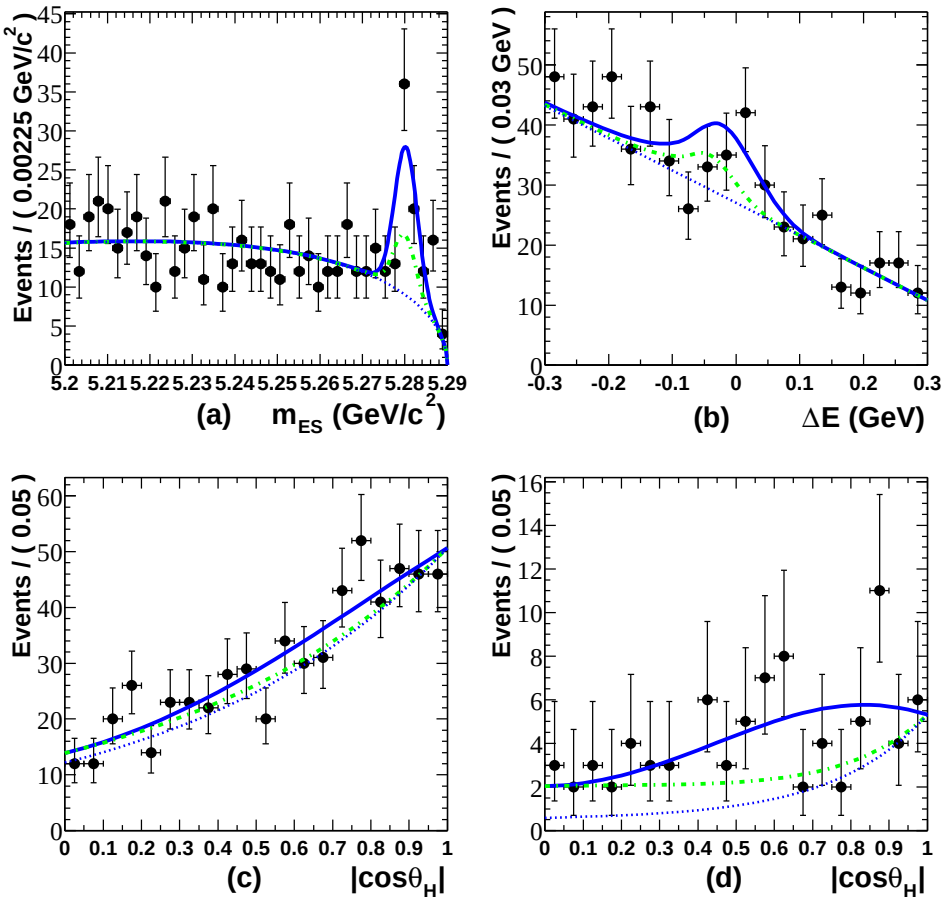

Figure 65: A fit to the $m_{\rm ES}$ (a), ΔE (b) and $\cos\theta_H$ (c) distributions for $\overline{B} \to \overline{K_2^{*0}(1430)}\gamma$, $\overline{K_2^{*0}(1430)} \to K^-\pi^+$ in data, and the $\cos\theta_H$ distribution in the signal region (d). (The solid line shows a fit to the data with the peaking (dash-dot) and non-peaking (dash) backgrounds as indicated.)

A GoodTracksLoose Definition

In the analysis we used the "GoodTracksLoose" criteria for all the charged tracks (like $K^{\pm}$,$\pi^{\pm}$).The requirements are:

- Number of drift chamber hits more than 12
- $|d_0| < 1.5\,\mathrm{cm}$. d_0 is the point of closest approach of the track to the nominal beam spot in the azimuthal plane(x-y). In the Babar coordinate system the nominal beam spot is at(x=0, y=0, z=0.33 cm)
- $|z_0| < 10\,\mathrm{cm}$. z_0 is the point of closest approach of the track to the beam spot in the polar plane(z)
- The transverse momenta of the track is greater than 100 MeV and the momenta is less than 10 GeV

B GoodPhotonLoose Criteria

The "GoodPhotonLoose" list is derived from the "CalorNeutral" list by further requiring:

- $E_\gamma > 30\,\mathrm{MeV}$.
- $LAT < 0.8$, LAT is the lateral profile variable.

C Data Samples

Below is a list of data and MC samples used in this analysis.

sample	events	$\mathcal{L}$ [fb^{-1}]
$B^0\bar{B}^0$	33858408	59.9
B^+B^-	34241092	60.6
$u\bar{u}/d\bar{d}/s\bar{s}$	124576347	59.6
$c\bar{c}$	83662589	64.3
$B^0 \to K^*(892)^0(K^0_S\pi^0)\gamma + CC$	40000	1327.4
$B^0 \to K^*(892)^0(K^\pm\pi^\mp)\gamma + CC$	40000	7964.4
$B^+ \to K^*(892)^+(K^+\pi^0)\gamma + CC$	73000	7267.5
$B^+ \to K^*(892)^+(K^0_S\pi^+)\gamma + CC$	73000	4845.0
$B^0 \to K_1(1273)^0\gamma + CC$	45k	2885.7
$B^0 \to K_1(1400)^0\gamma + CC$	45k	5943.7
$B^0 \to K^*(1410)^0\gamma + CC$	45k	3040.0
$B^0 \to K^*_2(1430)^0\gamma + CC$	22k	1166.2
$B^0 \to K^*(1680)^0\gamma + CC$	44k	24336.3
$B^+ \to K_1(1273)^+\gamma + CC$	45k	2885.7
$B^+ \to K_1(1400)^+\gamma + CC$	43k	5943.7
$B^+ \to K^*(1410)^+\gamma + CC$	45k	3040.0
$B^+ \to K^*_2(1430)^+\gamma + CC$	44k	2345.6
$B^+ \to K^*(1680)^+\gamma + CC$	45k	24889.4
$B^0 \to X_s d\gamma(EXP465)$	53k	148.9
$B^+ \to X_s u\gamma(EXP465)$	51k	143.3
$B^0 \to \eta' K_S(\eta' \to \rho^0\gamma)$	15k	228.9
$B^+ \to \eta' K^+(\eta' \to \rho^0\gamma)$	15k	177.0
off–resonance DATA Run–I		9.56
on–resonance DATA Run–I		81.4

References

[1] G. Feldman *et al.*, Proceedings of the 1988 DPF Summer Study (Snowmass, Colorado) pp.561-565 (1989).

[2] PEP-II An Asymmetric B Factory, SLAC-PUB-5379, June 1993.

[3] KEKB B-Factory Design Report, KEK Report 95-7, August 1995.

[4] D. Rice, Proceedings of 5th european Particle Accelerator Conference (EPAC96), pp.17-21.

[5] T. E. Browder, F. A. Harris, and S. Pakvasa, Proceedings of the 2nd international conference on B physics and CP violation (Honolulu Hawaii) pp.1-13 (1997).

[6] M. Beneke, T. Feldmann, and D. Seidel, hep-ph0106067; S. W. Bosch and G. Buchalla, hep-ph0106081; A. Kagan and M. Neubert, hep-ph0110078; Z. Ligeti and M. B. Wise, Phys. Rev. D **60**, 117506 (1999).

[7] CLEO Collaboration, Phys. Rev. Lett. **84**, 5283 (2000).

[8] BELLE Collaboration, S. Nishida *et al.* , Phys. Rev. Lett. **89**, 231801 (2002).

[9] ALEPH Collaboration, R. Barate *et al.*, Phys. Lett. B **429**, 169 (1998);

CLEO Collaboration, D. Cronin-Hennessy *et al.*, Phys. Rev. Lett. **87**, 251807 (2001);

BELLE Collaboration, K.Abe *et al.*, Phys. Lett. B **511**, 151 (2001);

BABAR Collaboration, B. Aubert *et al.*, hep-ex/0207076 and hep-ex/0207074 (2002).

[10] A. J. Buras, A. Czarnecki, M. Misiak and J. Urban, Nucl. Phys. B631:219, 2002 .

[11] B. Grinstein and D. Pirjol, Phys. Rev. D **62**, 093002 (2002); M. Beneke, T. Feldmann and D. Seidel, Nucl. Phys. B. proc. suppl **612**, 25 (2001); S. W. Bosch and G. Buchalla, Nucl. Phys. B. proc. suppl **621**, 459 (2002); A. Ali and A. Y. Parkhomenko, Euro. Phys. Jour **C23**, 89 (2002).

[12] L. Everett, G.L. Kane, S. Rigolin, L.T. Wang and T.T. Wang, JHEP **0201**, 022 (2002). For a review of B physics in SUSY models, see S. Bertolini, F. Borzumati and A. Masiero, *BDecays*, second edition, ed. S. Stone, World Scientific, 1994, p. 620.

[13] K. Fujikawa and A. Yamada, Phys. Rev. D **62**, 093002 (2000); M. Beneke, T. Feldmann and D. Seidel, Nucl. Phys. B **612**, 25 (2001); S.W. Bosch and G. Buchalla, Nucl. Phys. B **621**, 459 (2002); A. Ali and A.Y. Parkhomenko, Euro. Phys. Jour **23**, 89 (2002).

[14] D. Atwood, M. Gronau and A. Soni, Phys. Rev. Lett. **79**, 185 (1997); D. Melikhov, N. Nikitin and S. Simula, Phys. Lett. B **442**, 381 (1998); F. Kruger, L.M. Sehgal, N. Sinha and R. Sinha, Phys. Rev. D **61**, 114028 (2000); C.S. Kim, Y.G. Kim, C.D. Lu and T. Morozumi, Phys. Rev. D **62**, 034013 (2000); T. Mannel and S. Recksiegel, Acta Phys. Polonica **B28**, 2489 (1997).

[15] S. Veseli and M. G. Olsson, Modeling form factors in HQET, B. Grinstein, R. Springer, and M. B. Wise, Nucl. Phys. B 339, 269 (1990); A. Ali and C. Greub, Z. Phys. C 49, 431 (1991).

[16] A. J. Buras, M. Misiak, M. Munz, and S. Pokorski, Nucl. Phys. B **424**, 374 (1994); N. G. Deshpande, Theory of Penguins in B Decays, World Scientific, 1994.

[17] GEANT4 Collaboration, V.N. Ivanchenko *et al.*, Nucl. Instrum. Methods A.**494**, 514 (2002).

[18] M. Gronau, Y. Grossman, D. Pirjol and A. Ryd, Phys. Rev. Lett. **88**, 051802 (2002); M. Gronau, D. Pirjol, Phys. Rev. D **66**, 054008 (2002).

[19] T. Altomari, Phys. Rev. D **37**, 677 (1988).

[20] A. Ali, T. Ohl and T. Mannel, Phys. Lett. B **298**, 195 (1993).

[21] S. Veseli and M. G. Olsson, Phys. Lett. B **367**, 309 (1996).

[22] D. Ebert, R.N. Faustov, V.O. Galkin, and H. Toki, Phys. Lett. B **495**, 309 (2000).

[23] A.S. Safir, Euro. Phys. Jour **3**, 15 (2001).

[24] *BABAR* Collaboration, B. Aubert *et al.*, Nucl. Instrum. Methods A.**479**, 1 (2002).

[25] S. Veseli and M. G. Olsson, Phys. Lett. B **367**, 302 (1996).

[26] BELLE Collaboration, Phys. Rev. Lett. **89**, 231801 (2002).

[27] G. C. Fox and S. Wolfram, Nucl. Phys. B **149**, 413 (1979).

[28] Particle Data Group, K. Hagiwara *et al.*, Phys. Rev. D **66**, 010001 (2002).

[29] Stuttgart Neural Network Simulator, http://www-ra.informatik.uni-tuebingen.de/SNNS/.

[30] Homepage of the RooFit Toolkit, http://www.slac.stanford.edu/BFROOT/www/Computing/Offline/ROOT/RooFit/index.html .

[31] T. Colberg *et al.* , "Study of pi0 efficiencies in RUN1 data using tau 1-on-1 decays", *BABAR* collaboration internal document BAD196, unpublished.

[32] E. Varnes *et al.* , "Measurement of the GoodTrackLoose efficiency using SVT tracks", *BABAR* collaboration internal document BAD157, unpublished.

[33] *BABAR* Collaboration, B. Aubert *et al.*, "A measurement of the branching fraction of the exclusive decay $B^0 \to K^{*0}\gamma$", hep-ex/0008055.

[34] Homepage of Particle Identification Group, http://www.slac.stanford.edu/BFROOT/www/Physics/TrackEfficTaskForce/Recipe/KsTrack-R10.html

[35] Heart *et al.* , "Hadronic Event Selection and B-Counting for Inclusive Charmonium Measurements", *BABAR* collaboration internal document BAD30, unpublished; "Measurement of the Number of Upsilon(4S)

Mesons Produced in Run 1 (B Counting)", *BABAR* collaboration internal document BAD134, unpublished.

[36] C. Jessop *et al.* , "High Energy Photon Selection for Penguin Analysis", *BABAR* collaboration internal document BAD201, unpublished.

[37] *BABAR* Collaboration, B. Aubert *et al.*, Phys. Rev. Lett. **92**, 241802 (2004).

[38] BELLE Collaboration, published in *Ise-Shima 2001, B physics and CP violation* p71-74, hep-ex/0104045 and hep-ex/0107065.

[39] T. Altomari, Phys. Rev. D **37**, 677 (1988); A. Ali, T. Mannel, and T. Ohl, Phys. Lett. B **298**, 195 (1993); S. Veseli and M.G. Olsson, Phys. Lett. B **367**, 309 (1996); D. Ebert, R.N. Faustov, V.O. Galkin, and H. Toki, Phys. Lett. B **495**, 309 (2000); A.S. Safir, Euro. Phys. Jour **3**, 15 (2001).